

**LASER SINTERING OF NANOCOMPOSITE ON FLEXIBLE
SUBSTRATE: EXPERIMENTAL STUDY AND MOLECULAR DYNAMICS
SIMULATION**

by

Zheng Kang

A Dissertation

Submitted to the Faculty of Purdue University

In Partial Fulfillment of the Requirements for the degree of

Doctor of Philosophy



School of Mechanical Engineering

West Lafayette, Indiana

August 2019

THE PURDUE UNIVERSITY GRADUATE SCHOOL
STATEMENT OF COMMITTEE APPROVAL

Dr. Benxin Wu, Chair

Department of Mechanical Engineering

Dr. Yung C. Shin

Department of Mechanical Engineering

Dr. Liang Pan

Department of Mechanical Engineering

Dr. Gary J. Cheng

Department of Industrial Engineering

Approved by:

Dr. Anil K. Bajaj

Head of the Graduate Program

Dedicated to my beloved family

ACKNOWLEDGMENTS

I would like to extend my deepest appreciation to my advisor Prof. Benxin Wu, who has continually offered thoughtful guidance, inspiring discussions and steady support throughout my research and study. I am also very grateful to Prof. Yung C. Shin, Prof. Liang Pan and Prof. Gary J. Cheng for serving on my advisory committee.

Many thanks to my lab mates, Ze Liu, Navid Dabir-Moghaddam, Zhen Yang, Hanyu Song, Weidong Liu, Ran Le and Muxuan Wang. In research, I have enjoyed their valuable discussions and pleasant cooperation. They have also helped me and brought so much fun in my life. My gratitude also goes to Ruoxing Wang, Yixiu Wang, Shengjie Gao, Rong Xu, Jitendra Kumar Tripathi, Prof. Ahmed Hassanein and many others who have helped me a lot in my research. Dr. Christopher Gilpin, Robert Seiler and Laurie Mueller were really helpful with some related sample preparations and characterizations. The description of the TEM sample preparation process in Chapter 3 is based on the information and writing from Robert Seiler. I would like to thank all my coauthors in my publications for their contribution. I would also like to thank Rich DuVall, Mike Sherwood, and all staffs working in Machine shop and E-shop for helping me with various engineering ideas and lab work. I would like to thank Dmitry Zemlyanov for his related help. I would like to thank Mr. Yifan Zhu for his related early-stage work.

This material is based upon work supported by the National Science Foundation under Grant No. CMMI 1542376. Any opinions, findings, and conclusions or recommendations expressed in this material are those of the author(s) and do not necessarily reflect the views of the National Science Foundation.

Finally, I would express my warmest love to my family. Without their support and encouragement, I cannot imagine I would be where I am now.

TABLE OF CONTENTS

| | |
|---|----|
| LIST OF TABLES | 7 |
| LIST OF FIGURES | 8 |
| ABSTRACT | 12 |
| 1. INTRODUCTION | 14 |
| 1.1 Methods of Fabrication for Flexible Electronics | 14 |
| 1.1.1 Conventional Sintering | 15 |
| 1.1.2 Intense Pulsed Light Sintering | 16 |
| 1.1.3 Selective Laser Sintering | 17 |
| 1.2 Issues with Flexible Electronics During Application | 18 |
| 1.3 Molecular Dynamics Simulation of Atomic Processes | 20 |
| 1.4 Dissertation Outline | 25 |
| 2. LASER-BASED FABRICATION OF CARBON NANOTUBE – SILVER COMPOSITES WITH ENHANCED FATIGUE PERFORMANCE ONTO A FLEXIBLE SUBSTRATE..... | 27 |
| 2.1 Experiments | 28 |
| 2.1.1 Laser-Based Fabrication of CNT-Silver Composite Lines on a Polyimide Substrate | 28 |
| 2.1.2 Characterizations..... | 33 |
| 2.2 Results and Discussions..... | 36 |
| 2.3 Conclusions..... | 46 |
| 3. STRUCTURAL AND INTERFACIAL CHARACTERIZATIONS OF CARBON NANOTUBE –SILVER COMPOSITE ON FLEXIBLE SUBSTRATE | 48 |
| 3.1 Fabrication method and characterization approaches | 49 |
| 3.1.1 Fabrication of CNT-silver composites on polyimide substrates..... | 49 |
| 3.1.2 Sample Characterizations..... | 52 |
| 3.2 Results and Discussions..... | 54 |
| 3.2.1 Introduction to Characterization results..... | 55 |
| 3.2.1.1 SEM and EDS | 55 |
| 3.2.1.2 TEM and EDS in STEM Mode | 57 |
| 3.2.1.3 XPS Analysis..... | 59 |
| 3.2.2 Analysis and Discussions on Characterization Results | 63 |

| | |
|---|-----|
| 3.2.2.1 CNT-Silver Interfaces in the Composite | 63 |
| 3.2.2.2 Interface between the CNT-silver Composite and the Polyimide Substrate | 65 |
| 3.3 Conclusions..... | 69 |
| 4. STATIC TENSILE TESTS AND ADHESION TESTS OF LAESR SINTERED CNT-SILVER COMPOSITE ON FLEXIBEL SUBSTRATE | 71 |
| 4.1 Experiment Setup..... | 71 |
| 4.2 Results and Discussion | 74 |
| 4.2.1 Static Tensile Test..... | 74 |
| 4.2.2 Adhesion Test | 78 |
| 4.3 Conclusions..... | 80 |
| 5. COALESCENCE OF GOLD NANOPARTICLES AROUND THE END OF A CARBON NANOTUBE: A MOLECULAR-DYNAMICS STUDY..... | 81 |
| 5.1 Model Setup..... | 81 |
| 5.2 Results and Discussions..... | 84 |
| 5.2.1 MD Model Comparison with Experiment-Deduced Results | 84 |
| 5.2.2 MD Study of NP Coalescence and NP-CNT Interaction Near the End of the CNT .. | 86 |
| 5.2.2.1 Effect of CNT diameter on coalescence and interactions under the targeted temperature of ~600 K | 87 |
| 5.2.2.2 Effect of Temperature on Coalescence and Interactions..... | 94 |
| 5.3 Conclusions..... | 99 |
| 6. CONCLUSTIONS AND FUTURE WORK..... | 101 |
| 6.1 Research Review and Conclusions | 101 |
| 6.2 Recommendations for Potential Future Research..... | 103 |
| REFERENCES | 105 |
| VITA | 118 |
| PUBLICATIONS..... | 119 |

LIST OF TABLES

| | |
|--|----|
| Table 2.1 Laser power (which is ~0.35 W or ~0.4 W), number of scans and line thickness for the eight groups of lines compared in the fatigue bending tests (the test results are shown in Figure 2.6 and 2.7). | 42 |
| Table 3.1: Summary of the binding energy (BE) and the full-width at half-maximum (FWHM) (in the unit of eV) for each deconvoluted peak in the high-resolution XPS spectra in Figure 3.8 and the corresponding chemical state identified, for Sample (a), (b) and (c), respectively | 61 |
| Table 3.2: Atomic percentage of different chemical states of silver deduced from the XPS results in Figure 3.8(the bottom left group) for Sample (a), (b) and (c) respectively. | 61 |
| Table 5.1 MWCNT parameters used in the MD simulations of this work..... | 85 |

LIST OF FIGURES

| | |
|---|----|
| Figure 1.1 Size effect of melting temperature in gold nanoparticles. Data points in (a) are digitized from (Buffat & Borel, 1976), which gives experiment deduced data. The dashed blue line in (a) is melting point of bulk gold (Goudeli & Pratsinis, 2016). | 15 |
| Figure 1.2 Structural evolution during the sintering process of misoriented metal NPs. Angular separations over time between two [100] crystallographic axes ($\Delta\theta[100]$) are shown at (a) 500K with initial $\Delta\theta = 10^\circ$; (b) 500K comparing initial $\Delta\theta = 10^\circ$ with initial $\Delta\theta = 20^\circ$ and (c) 1100K with initial $\Delta\theta = 10^\circ$. Atomic structures at difference stages of the two particles coalescing in case (a) are shown in (i)-(iii). Angular velocities are not dependent on initial $\Delta\theta$ as shown in (b). Corresponding structures (iv)-(vi) in case (c) show that particle rotation is minimal while slippage on planes parallel to neck groove improves particle co-alignment. Reproduced with permission from (Lange et al., 2016). Copyright © Elsevier, 2016. | 24 |
| Figure 2.1 Schematic diagram of the fabrication process to produce CNT-silver composite lines onto a polyimide film (not drawn to scale, not all components or details given, and the demonstrated details not necessarily exact; there is a plastic layer below the polyimide film for mechanical support). | 30 |
| Figure 2.2 An SEM image of silver nanoparticles purchased for this work (some silver nanoparticles are put into acetone, and a certain amount of the formed suspension is dropped onto a copper tape, and the SEM observation is made after the acetone is evaporated). | 32 |
| Figure 2.3 Schematic diagram of the experimental setup for the fatigue bending tests: (a) isometric view; (b) and (c) side view (not drawn to scale, not all components or details given, and the demonstrated details not necessarily exact). | 36 |
| Figure 2.4 SEM images of the sintered CNT-silver composite: (a) laser power: ~ 0.4 W, single scan; (b) laser power: ~ 0.4 W, double scans. | 39 |
| Figure 2.5 The measured electrical resistivity of laser-sintered silver lines and CNT-silver composite lines produced under different laser powers of ~ 0.29 W to ~ 0.40 W by: (a) single laser scan, and (b) double laser scans. | 39 |
| Figure 2.6 The normalized electrical resistivity versus the number of bending cycles obtained from the fatigue bending tests for laser-sintered silver lines and CNT-silver composite lines in different test groups (the “normalized” electrical resistivity is for the region of $x = -2.5$ to $+2.5$ mm for each line; the laser power, number of scans and line thickness for each group are shown in Table 2.1; data points when the normalized resistivity is above 100 are not shown). | 41 |
| Figure 2.7 The fatigue life (in terms of the number of bending cycles) for each tested group of laser-sintered silver and CNT-silver composite lines based on the failure criterion of the normalized resistivity (as given in Figure 2.6) reaching 10 (the point with an upward-pointing arrow means that the normalized resistivity is still below the failure criterion at the maximum number of bending cycles tested in the experiment, and hence this maximum number is plotted here, but the actual fatigue life should be longer). | 42 |

- Figure 2.8 SEM images of the CNT-silver composite line in the tested Group 7 after the fatigue bending test (i.e., after being bent for ~2800 cycles)..... 44
- Figure 2.9 SEM images of the silver line in the tested Group 7 after the fatigue bending test (i.e., after being bent for ~580 cycles). 45
- Figure 2.10 (a) Cross-section profile for an as-printed silver NP+ CNT line (an averaged profile measured using a white-light interferometer over a 0.5-mm long section of the line); and (b) SEM image of another as-printed silver NP+CNT line (the lines are dispensed onto a polyimide surface, and then dried, but not sintered). 45
- Figure 3.1 Schematic of the major procedure for laser-based fabrication of CNT-silver composite on a polyimide substrate (the chamber has an inlet and outlet for argon gas flow; not all components are shown in the schematic, which is not drawn according to the exact actual details). 49
- Figure 3.2 An SEM image of some silver nanoparticles (NPs) purchased to fabricate CNT-silver composites in this study (silver nanoparticles were stirred in acetone to form a suspension, several drops of which were dispensed onto a copper tape. Then the SEM image was taken after acetone on the copper tape was evaporated). 51
- Figure 3.3 Schematics of: (a) the definition of the top and bottom surface of each CNT-silver composite line in a cross-sectional view; and (b) the setup to expose the bottom surface of a CNT-silver composite line by peeling the line off from the polyimide substrate..... 53
- Figure 3.4 SEM images of: (a) the top surface of a laser-sintered CNT-silver composite line on a polyimide substrate; and (b) the bottom surface of a CNT-silver composite line, after the composite is peeled off from the polyimide substrate (the bottom surface is tilted by 25° in the image). The average electrical resistivity was measure to be ~10.2 $\mu\Omega\cdot\text{cm}$ for the whole group of CNT-silver composite line samples prepared for characterizations, where the average thickness of the group of composite lines was ~1.49 μm . The two images shown above are from two different samples. 55
- Figure 3.5 (left) An SEM image for a region of the bottom surface of a CNT-silve composite line (where the bottom surface is exposed in the way shown in Figure 3.3b); and (right) an image showing the distributions of some elements measured by EDS for the region. 56
- Figure 3.6 TEM image of a region in the cross-section of a laser-sintered CNT-silver composite sample (a), and TEM image of a CNT in the composite at a higher magnification (b). 57
- Figure 3.7 TEM images of the cross-section of a laser-sintered CNT-silver composite line on a polyimide substrate: (a) for a portion near the composite line side boundary; and (b) for a more central region of the line. The insets show silver weight percentage from EDS analysis performed in the STEM mode for multiple points approximately labeled on each TEM image. 58
- Figure 3.8 XPS results: survey spectra (the top left group), high-resolution spectra around C 1s peaks (the top right group), Ag 3d peaks (bottom left group) and O 1s peaks (bottom right group). For each group of spectra, Row (a), (b) and (c) are results for Sample (a) (top surface of a CNT and silver NP mixture before sintering), Sample (b) (top surface of a sintered CNT-silver composite line) and Sample (c) (exposed bottom surface of a sintered CNT-silver composite line), respectively. In spectra plots for C 1s, for simplicity “C=O” is used to roughly represent carbonyl

| | |
|---|----|
| carbon and “C-O” to represent aromatic carbon connected with an ether oxygen, respectively. In plots for O 1s, for simplicity “C-O-C” is used to roughly represent ether oxygen..... | 60 |
| Figure 3.9 TEM image of a cross-section of a laser-sintered CNT-silver composite line on a polyimide substrate | 67 |
| Figure 4.1 Schematic setup of static tensile tests..... | 74 |
| Figure 4.2 Schematic setup of adhesion test..... | 74 |
| Figure 4.3 Normalized resistance change curve during static tensile tests. (a) Ag sintered with ~0.35W laser. (b) Ag sintered with ~0.4W laser. (c) CNT-silver sintered with ~0.35W laser. ... | 75 |
| Figure 4.4 Optical microscope images of sintered lines during static tensile tests at different strains. | 77 |
| Figure 4.5 SEM images of Ag @~0.4W laser(left) and CNT-silver @~0.35W laser(right) samples after static tensile tests. | 78 |
| Figure 4.6 Shear strength of laser sintered materials on PI film under different conditions. | 79 |
| Figure 5.1 Initial configuration and geometrical setup of the MD model: (a) side view, and (b) view from the bottom end of the MWCNT (Yellow atoms represent Au atoms, while black atoms represent carbon atoms. Four Au NPs surround the central Au particle with a center-to-center distance of 3.4 nm; and the center of the latter is 1.9 nm away from the end of the CNT whose diameter in different cases is listed in Table 5.1) | 82 |
| Figure 5.2 (a) Melting points of Au NPs at different sizes predicted by MD simulations in this work, in comparison with experiment-deduced melting points digitized from a figure in Ref. (Buffat & Borel, 1976). (b): MD-predicted PE per atom versus temperature for 3-nm Au NPs during heating and cooling processes. (c) MD-predicted PE per atom versus temperature for Au NPs of different sizes during a heating process. | 87 |
| Figure 5.3 MD-predicted system evolution where the system temperature is 600 K at the end of the 100-ps heating stage. Column 1: system that only consist of Au NPs; Column 2, 3 and 4: system with Au NPs initially near the end of a MWCNT with different diameters (The heating stage starts at $t=0$ ps and ends at $t=100$ ps, after which the system is maintained in the NVE ensemble during the simulation. Images shown are for cross-sections of NPs and/or CNTs. Carbon atoms are plotted in black. Gold atoms are plotted in colors denoting their local atomic structures identified through the adaptive CNA approach (Stukowski, 2012). The green,blue and red colors correspond to fcc (face-centered cubic), bcc (body-centered cubic), and hcp (hexagonal close packed) structures respectively while the white color is used to plot atoms with unidentified structures (such as surface atoms or disordered atoms))...... | 91 |
| Figure 5.4 Mean squared displacement (MSD) of gold (Au) atoms for the different simulated systems shown in Figure 5.3..... | 92 |
| Figure 5.5 Radial distribution function (RDF) evolution of gold atoms for the simulated system in Figure 5.3 with the 2.04-nm inner diameter CNT. | 93 |
| Figure 5.6 MD-predicted system situation at the end of the simulation period ($t=600$ ps) (Column 1: system that only consists of Au NPs; Column 2, 3 and 4: system with Au NPs initially near the | |

end of a MWCNT with different diameters. Different rows correspond to systems with different temperatures at the end of the heating stage. Images shown are for cross-sections of the systems. Carbon atoms are plotted in black, while gold atoms are plotted in colours representing their local atomic structures that are identified with the adaptive CNA approach (Stukowski, 2012). The green, blue and red colours represent fcc, bcc and hcp structures, respectively, while atoms with unidentified structures are plotted in white (such as surface atoms or disordered atoms)) 95

Figure 5.7 The (15,15)-(20,20) CNT and the gold atoms inside the CNT at $t = 600$ ps based on the MD simulation (system temperature at the end of the heating stage: $T = 800\text{K}$). (a) Top view of a cross section of the CNT. (b) Side view of the most external layer of the gold atoms inside the CNT. Carbon and gold atoms are plotted in black and yellow, respectively. In (b), bonds are drawn for the visualization purpose only. 96

Figure 5.8 MD-predicted Mean Squared Displacement (MSD) of gold atoms around a: (a) (10, 10)-(15, 15) MWCNT, and (b) (15, 15)-(20, 20) MWCNT (the system temperature at the end of the 100-ps heating stage is indicated in the plots). 97

Figure 5.9 Radial distribution function (RDF) evolution of gold atoms for (a) a system with Au NPs initially around the end of a (15,15)-(20,20) MWCNT, and (b) a system with Au NPs only (the system temperature at the end of the heating stage is 800 K). 98

ABSTRACT

Author: Kang, Zheng. Ph. D.

Institution: Purdue University

Degree Received: August 2019

Title: Laser Sintering of Nanocomposite on Flexible Substrate: Experimental Study and Molecular Dynamics Simulation.

Committee Chair: Dr. Benxin Wu

Flexible electronics involve electronic circuits fabricated on flexible substrates. They have promising applications in wearable devices and flexible sensors etc. and have thus attracted much research interest in recent years. The working environment of flexible electronic devices may require them to go through repeating deformations, during which cracks may generate and grow in the metallic components of the devices, reducing service life of these devices. To address such challenges, it is desirable to investigate methods to improve the reliability of flexible electronics in these working conditions.

This research reported here will focus on topics related to laser-based fabrication of carbon nanotube-metal composites on flexible substrates:

Experimental studies were carried out to investigate the structures and properties of carbon nanotube – metal composites produced by a laser-based fabrication process on flexible substrates. Extensive characterizations and testes were carried out, including measurements of electrical resistivity of laser-sintered material, characterizations with SEM, TEM, EDS and XPS, and mechanical performance tests (bending fatigue test, static tensile test and adhesion test). The experimental study suggests that the laser-fabricated metal composites have promising potentials to help enhancing reliability and durability of metal components in flexible electronic devices.

A molecular dynamics model was also developed to study the coalescence of metal nanoparticles (gold NPs in this study) around the end of a multi-walled carbon nanotube (MWCNT)

and their interaction with the CNT at elevated temperatures. The MD model was first tested by comparing the MD-predicted NP melting points with experiment-deduced results from the literature. Then the coalescence of five 3-nm Au NPs around the end of a MWCNT and their interactions with the CNT were studied with MD simulations. The molecular system was studied under different elevated temperatures and for different carbon nanotube diameters, and the simulation results were analyzed and discussed.

1. INTRODUCTION

Flexible electronics, where electronic circuits are fabricated onto flexible substrates such as polymers, have several advantageous features, such as compactness, low weight, low energy consumption, and easiness in their integration with other devices, and hence the relevant market is expected to enjoy fast pace growth in the near future (Akogwu et al., 2010; Banks, 2010; Cordill, 2010; Perelaer et al., 2010; Wong & Salleo, 2009). Flexible electronics may find exciting applications in space exploration, sensors, displays, flexible solar cells and other areas(Akogwu et al., 2010; Banks, 2010; Short & Van Buren, 2014). Motivated by the promising future, tremendous research into flexible electronics has been ongoing in recent years. In the following sections of this chapter, a brief introduction will be presented on current research efforts for fabrication and enhancement of flexible electronics. Simulation methods are also introduced to help evolve better understanding of the fundamental problems and processes during fabrication of flexible electronics.

1.1 Methods of Fabrication for Flexible Electronics

Fabrication of flexible electronics often consists of two major processes: printing followed by sintering. Printing methods include inkjet printing, aerosol jet printing, sputter coating, etc. More details on the printing process technology and parameters that dictate the quality of printing are introduced elsewhere (Fukuda & Someya, 2017; Tekin, Smith, & Schubert, 2008). After drying the solvent in the ink, a thin layer of material is formed on top of the substrate. Commonly used sintering/melting methods consist of furnace, intense pulsed light, laser, microwave, electric current and plasma, etc. (Kamyshny & Magdassi, 2014). The temperature required for sintering depends on the size of metal nanoparticles: the melting temperatures of metal nanoparticles may

decrease drastically when the particle size is small enough. For example, the melting temperatures of gold nanoparticles at different particle size is shown in Figure 1.1. When the nanoparticle size is around 20 nm, the melting temperature of gold is close to that of bulk gold. As gold particle size drops below 10 nm, the melting point decreases sharply. At diameter of ~ 2.5 nm, the gold nanoparticle may even start to melt around 400K.

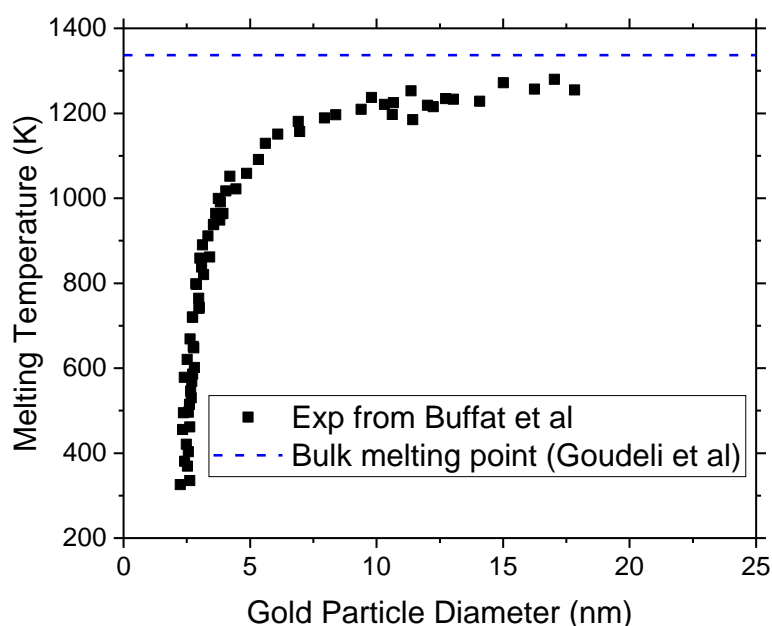


Figure 1.1 Size effect of melting temperature in gold nanoparticles. Data points in the figure are digitized from (Buffat & Borel, 1976), which gives experiment deduced data. The dashed blue line is the melting point of bulk gold (Goudeli & Pratsinis, 2016).

1.1.1 Conventional Sintering

The conventional sintering uses furnace/oven, hot plate or other apparatus where the temperature is controlled, and the samples can be heated for a certain amount of time (usually tens of minutes or hours). The printed materials, typically metal nanoparticles for flexible electronics, may melt or surface melt under the set temperatures and then a piece of conductive material will be formed. Quality of thermal sintering is dictated by temperature and duration of sintering, both

of which can be flexibly controlled. With proper duration of heating, good electrical resistivity can be obtained using thermal sintering. Y. J. Moon, H. Kang, K. Kang, S.-J. Moon, and J. Y. Hwang (2015) sintered silver nanoparticles at different temperatures. The electrical resistivity reduced from $18.4 \mu\Omega \cdot \text{cm}$ at sintering temperature of 150°C to $5.8 \mu\Omega \cdot \text{cm}$ at 250°C . However, with further increase of temperature, the electrical resistivity increases, which was attributed to stronger volumetric material transport at higher temperatures. As a result, disconnecting islands of materials were formed. Shen, Zhang, Huang, Xu, and Song (2014) printed ~ 30 nm silver NPs using inkjet and annealed at 180°C for 15 mins. The electrical resistivity was only $3.7 \mu\Omega \cdot \text{cm}$, which is about twice of bulk silver. Silver NPs with the size of 40-60 nm were embedded inside poly(dimethylsiloxane) (PDMS) and the sample was sintered at 150°C for as long as 2 hr (J. Jiang et al., 2016). This long duration of heating helps reduce the electrical resistivity to $1.67 \mu\Omega \cdot \text{cm}$.

1.1.2 Intense Pulsed Light Sintering

In intense pulsed light (IPL) sintering, a high-energy broadband light pulse is shot on nanostructures. IPL allows large area of sintering in milliseconds and is thus favorable in large scale roll-to-roll production (Hwang & Malhotra, 2018; H. Kang, Sowade, & Baumann, 2014). Hwang and Malhotra (2018) used multi pulses from a linear xenon lamp at a duration of 1.275 ms to sinter silver nanowires and nanospheres. Different ratios between silver nanowires and nanosphere are compared to explore neck growth dynamics and self-damping optical behavior. The self-damping effect is the mechanism that optical absorption tends to be hindered by neck growth and nanostructure change during sintering, and the optical absorption decrease further suppresses temperature rise and neck growth.

As a large area is covered with IPL sintering, parameters need to be calibrated to address certain issues brought by large exposure. Pulse duration, pulse energy and peak pulse intensity

need to be selected in IPL to avoid excessive energy damaging the substrate because the substrate is exposed in large area irradiation(Han, Hong, Kim, & Song, 2011). As IPL sheds light in a scale of cm^2 (Niittynen, Sowade, Kang, Baumann, & Mäntysalo, 2015), the resolution of IPL is determined by the printing process proceeding sintering, which is typically hundreds of micrometers (H. S. Lim, Kim, Jang, & Lim, 2017; Niittynen et al., 2015). Alternatively, a thick paper mask and a photo mask can be applied to achieve selective sintering (Zhong et al., 2016). With the application of 15 μm line pattern photomasks, IPL sintering produced line patterns with width of 18.7 μm . The broadening of line pattern width is mainly due to light diffraction as the mask has to be kept a distance away from the printed material.

1.1.3 Selective Laser Sintering

Unlike intense pulsed light sintering, where high energy of pulsed light is shot from a source to induce thermal effects in target materials, selective laser sintering uses coherent light emission with narrow bandwidth light wavelength. Compared to traditional sintering and other sintering techniques, laser sintering has the potential advantages such as: high spatial resolution, small heat affect zone and high flexibility (S. Hong et al., 2013; Ko, Pan, Grigoropoulos, Luscombe, Fr chet, et al., 2007a; W. Zhao et al., 2015).

Spatial resolution of selective laser sintering is usually determined by laser spot size, which is commonly available in the range of tens of micrometers or even several micrometers. The width of sintered lines can be adjusted flexibly by changing parameters such as operation mode of laser, scanning speed, number of scans and spot size, etc. Small heat affect zone by laser sintering is achieved by focused laser beam and/or short laser duration. Localized heat delivery helps reduce undesirable thermal effect or damage into the substrate. This feature of laser sintering is desirable to thermal sensitive materials. Furthermore, the sintering pattern or paths of laser sintering can be

easily controlled or programmed to accommodate different tasks, without the need of masks or vacuum.

With these advantages, laser sintering has attracted much research interest in the field of flexible electronics. Theodorakos et al. (2015) compared laser sintering performance with three different types of laser modes: continuous wave, nanosecond laser, and picosecond laser and two laser wavelengths: 532 nm and 1064 nm. They achieved electrical resistivity of $30 \mu\Omega\cdot\text{cm}$ with picosecond laser at 1064nm and concluded that better sintering can be obtained at wavelength of 1064 nm because the optical penetration depth is higher for silver at 1064 nm, enabling silver nanoparticles to be better sintered throughout the depth. Ko, Pan, Grigoropoulos, Luscombe, Fréchet, et al. (2007b) fabricated transistors with line width of $6 \mu\text{m}$ from gold nanoparticles. Low temperature sintering was achieved by thermodynamic size effect by using 1-3 nm gold nanoparticles, which has a melting point around $150 \text{ }^\circ\text{C}$. Transparent conductor grid pattern with an optical transmittance over 85% was developed using selective laser sintering of silver NPs (S. Hong et al., 2013). The line width was $\sim 11 \mu\text{m}$ and electrical resistivity was about $7 \mu\Omega\cdot\text{cm}$.

1.2 Issues with Flexible Electronics During Application

The working environment or applications often raise challenges for flexible electronics. Flexible devices often need to go through repeated deformations (such as bending, rolling, twisting, stretching, etc.) and related stresses and strains. This may cause the initiation and development of cracks in metallic components (e.g., metallic interconnects) that often exist in many flexible electronic devices (Akogwu et al., 2010; Begley, Scott, Utz, & Bart-Smith, 2009; Perelaer et al., 2010), which could obviously affect the long-term reliability and durability of the devices. Therefore, an effective approach to enhance the fatigue performance and durability of metallic

components in flexible electronics is desired. Among the candidate materials for enhancing flexible electronics, carbon nanotubes (CNTs) have attracted a lot of attention due to their superior mechanical and electrical properties. The tensile strength of CNT is reported to be about 30 GPa (Yu, Files, Arepalli, & Ruoff, 2000). Electrical resistivity of CNTs were measured to be about $30 \mu\Omega \cdot \text{cm}$ for multi walled CNTs (Bachtold et al., 1998). A current density of $2.5 \times 10^9 \text{ A/cm}^2$ was reported by McEuen, Fuhrer, and Park (2002).

With these exceptional properties, CNT has been used to strengthen various composites soon after its discovery in the early 1990s (Iijima, 1991). It has been found that CNT-metal composites could exhibit better mechanical properties than metals, such as improved strength, toughness and/or ductility (H. Li et al., 2009; Paramsothy, Hassan, Srikanth, & Gupta, 2010). By adding 5 vol% of aligned CNTs into copper matrix, S. Zhao et al. (2016) achieved 67.3% increase in hardness and 30.4% increase in tensile strength. Subramaniam et al. (2013) reported a CNT-copper composite that has an electrical conductivity similar to copper, but has a 100-times better ampacity (i.e., the capacity of carrying current).

However, previous work in the literature has been limited on producing CNT-metal composites onto flexible substrates. Obviously, several typical processes for CNT-metal composite fabrications, such as hot pressing and plasma spraying (Deng, Zhang, Wang, & Ma, 2007; Laha, Agarwal, McKechnie, & Seal, 2004), are difficult to use in this situation, because they may damage the fragile flexible substrates and/or often lack the desired spatial resolutions. D. Zhao et al. (2012) produced CNT-metal composites onto a Kapton polyimide film through aerosol-jet printing followed by furnace sintering, while Hwang, Joo, and Kim (2015) reported research work on the fabrication of CNT-metal composite films onto a polyimide substrate through intense pulsed light (IPL) sintering.

The present research reports a new approach (to our best knowledge) of producing CNT–metal composites onto flexible substrates through laser sintering of CNTs and metal nanoparticles (NPs), which was proposed by Wu (2017). With the favorable features discussed in earlier sections, selective laser sintering is a promising method of fabricating CNT-metal composites on flexible substrates. Although research work about laser sintering of metal nanoparticles (without CNTs) on polymer or other substrates has been performed by researchers (S. Hong et al., 2013; Ko, Pan, Grigoropoulos, Luscombe, Fréchet, et al., 2007b; Ko, Pan, Lee, Grigoropoulos, & Park, 2010; Pan, Ko, & Grigoropoulos, 2007; Theodorakos et al., 2015), the reported fabrication of CNT–metal composites onto a flexible substrate through laser sintering has been relatively rare to our best knowledge. Ji, Ajmal, Kim, Chang, and Baik (2017) reported laser sintering of conductive flexible adhesive (CFA) onto a flexible substrate. The CFA contains silver flakes, CNTs decorated by silver nanoparticles and a nitrile-butadiene-rubber matrix. The laser sintered material can have an electrical resistivity of about $40 \mu\Omega \cdot \text{cm}$. As introduced later, the novel approach in this research can achieve electrical resistivity that is much lower than that in Ji et al. (2017). This approach is different from that in Ji et al. (2017) and does not use CFA. Instead, a suspension of CNTs and silver nanoparticles (without a nitrile-butadiene-rubber matrix) in liquid is dispensed onto the flexible substrate, dried, and then laser-sintered.

1.3 Molecular Dynamics Simulation of Atomic Processes

Metallic nanoparticles have attracted lots of research attentions because of their current or potential applications in several areas, such as additive manufacturing, flexible electronics, catalysis, drug delivery and sensing, etc. (Asoro, Kovar, & Ferreira, 2013; Hu, Liu, Li, & Sun, 2014; Pan, Ko, & Grigoropoulos, 2008; J. Wang, Chen, Cui, Li, & Chen, 2016). During processes

related to some applications, coalescence of metal nanoparticles under certain conditions may often be involved. Therefore, it is important (and may be very valuable to related applications) to understand the interaction mechanisms and coalescence processes of metal nanoparticles, which has drawn lots of research attentions (Anand, Lu, Loh, Aabdin, & Mirsaidov, 2015; Arcidiacono, Bieri, Poulikakos, & Grigoropoulos, 2004; Asoro, Kovar, Shao-Horn, Allard, & Ferreira, 2009; González-Rubio, Guerrero-Martínez, & Liz-Marzán, 2016; Lange et al., 2016; H. B. Liu, Jos Yacaman, Perez, & Ascencio, 2003; Pan et al., 2008; J. Wang et al., 2016).

As mentioned above, carbon nanotubes (CNTs) have outstanding electrical and mechanical properties (Bachtold et al., 1998; McEuen et al., 2002; Treacy, Ebbesen, & Gibson, 1996; Yu et al., 2000), and hence are often applied in composites to enhance material properties. The fabrication of CNT-metal composites may often involve sintering of CNTs and metal NPs at elevated temperatures induced by laser or furnace heating. For example, the research (Z. Kang, Wu, Wang, & Wu, 2018a; D. Zhao et al., 2012) studied the fabrication of CNT-silver composites onto a flexible substrate through sintering of mixtures of CNTs and metal NPs with a laser beam and in a furnace, respectively. During laser or furnace-based sintering of CNTs and metal NPs, the coalescence of metal NPs in the presence of CNTs and the interactions among CNTs and different NPs at elevated temperatures are expected to occur, and are very critical processes that may strongly affect the properties and performance of the sintered composites. Hence, a good understanding of the coalescence and interaction processes is very important.

Molecular dynamics (MD) simulation provides a tool that is very powerful in the exploring and understanding of process mechanisms at the atomic scale. The simplest form of MD that consists of particles without structures involves mainly Newton's second law (Rapaport, 2004). But for those with rigid molecules, MD simulations may require Euler equations expressed in the

Hamilton's quaternions. More complex molecules with internal degrees of freedom might also involve Lagrange method which is required to include geometric constraints in the dynamical equations (Rapaport, 2004). MD simulation is largely dependent on development of computers. Now with the increasing availability of computation resources, MD has been applied more and more by researchers to investigate the interactions of metal NPs (Goudeli & Pratsinis, 2016; Guevara-Chapa & Mejía-Rosales, 2014; Pan et al., 2007).

Interactions of NPs during neck growth has been studied extensively as the core development process in the coalescence of metal NPs. Coalescence process typically consists of two stages (Pan et al., 2008; Goudeli & Pratsinis, 2016). At the first stage, two isolated metal NPs are attracted to each other. As two NPs adhere to each other, the NPs start to merge at the contacting surface and this stage is dominated with surface diffusion where atoms on NP surfaces, even if they are further away from the contacting area than nearby bulk atoms, tend to flow to the contact area and the neck grows. Meanwhile bulk atoms toward the inside of the surface, though they are close to contact area, are less mobile than surface atoms and they may retain initial crystalline structures. During the second stage of sintering, the neck growth stagnates, and it is dominated mainly by grain boundary diffusion (Asoro et al., 2009; Goudeli & Pratsinis, 2016). Goudeli and Pratsinis (2016) studied crystallinity of gold NPs to explore its effect on sintering rate and mechanism. Amorphous nanoparticles show much faster sintering rate than crystalline ones. S. J. Zhao, Wang, and Yang (2001) revealed that when the NP crystalline structures are not aligned, the NPs may experience rigid body rotation soon after adhesion, to reduce excessive surface energy and achieve a low-energy configuration. Lange et al. (2016) further elucidated the structures evolution during the sintering process of misoriented metal NPs, as presented in Figure 1.2. At lower temperature, i.e. 500K, rigid body rotation occurred immediately after NP adhesion, but it

did not stop at perfect alignment (Figure 1.2a). Grain boundary dislocations were observed after the rigid body rotation and the dislocations remained around the interface. Plastic deformation also formed in a region near the interface (Figure 1.2 iii). It is worth noting that the angular difference in the NPs showed little impact on the speed of rigid body rotation, at least in the first 25 ps of the coalescing process (Figure 1.2b). At temperature of 1100K, however, rigid body rotation was not observed after NP adhesion (Figure 1.2c). This was attributed to strong surface diffusion at this temperature. Slippage of dislocations occurred around the interface and led to plastic deformation.

The impact of laser heating on metal NPs has also been investigated (Pan et al., 2008; Pan et al., 2007). The laser heating process is simulated by applying proper heating rate to the system. As the particle sizes are typically much smaller than laser spot size, profile of laser was not considered. S. Jiang, Zhang, Gan, Chen, and Peng (2013) simulated the laser heating of hollow nanoparticles and discovered different deformation mechanisms than solid nanoparticles, implying the geometric shape of nanoparticles also plays a role in coalescence.

Furthermore, MD simulation has been applied to investigate the interaction of metal nanoclusters with *the sidewalls* of CNTs (Akbarzadeh & Abbaspour, 2016), or the interaction of a single NP with the ends of CNTs (J. Cui, Yang, Zhou, & Wang, 2014). Akbarzadeh and Yaghoubi (2014) reported MD simulations on the heating and cooling processes of silver nanoclusters supported by a single-walled CNT near its sidewall, while in another research (Akbarzadeh & Abbaspour, 2016) the processes of CNT-supported Ag-Au alloy nanoclusters (near the CNT sidewall) were studied through MD simulations. J. Cui et al. (2014) reported MD simulations of nanoscale soldering processes, where an Ag nanoparticle was positioned between the ends of two CNTs. However, to our best knowledge, previous research work has been rarely reported on the coalescence of multiple metal NPs and their interactions with a CNT, *near the end* (instead of the

sidewall) of the CNT, which is a common and hence important situation. It is expected that the coalescence and interactions that occur near the end of a CNT may have significant differences from those that occur near the sidewall of a CNT, and hence deserve further research attentions.

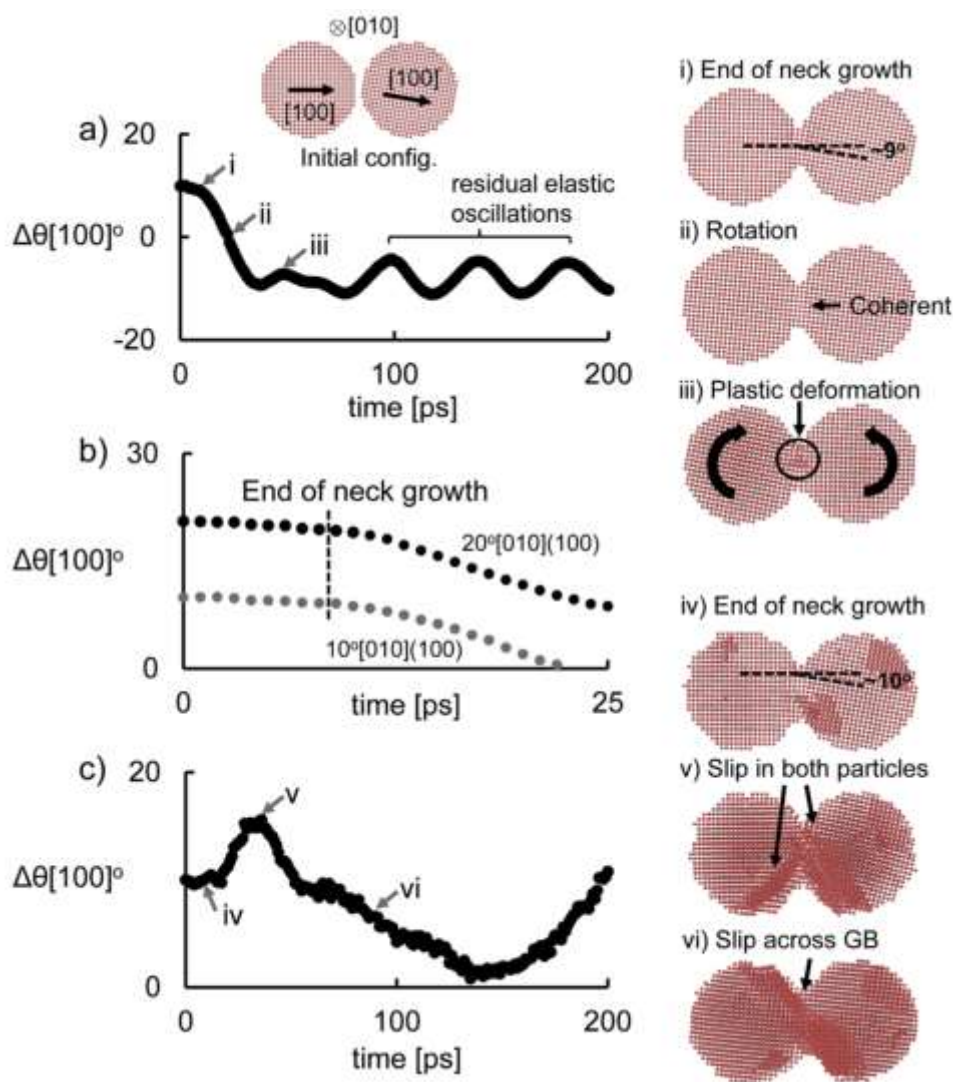


Figure 1.2 Structural evolution during the sintering process of misoriented metal NPs. Angular separations over time between two $[100]$ crystallographic axes ($\Delta\theta[100]$) are shown at (a) 500K with initial $\Delta\theta = 10^\circ$; (b) 500K comparing initial $\Delta\theta = 10^\circ$ with initial $\Delta\theta = 20^\circ$ and (c) 1100K with initial $\Delta\theta = 10^\circ$. Atomic structures at difference stages of the two particles coalescing in case (a) are shown in (i)-(iii). Angular velocities are not dependent on initial $\Delta\theta$ as shown in (b).

Corresponding structures (iv)-(vi) in case (c) show that particle rotation is minimal while slippage on planes parallel to neck groove improves particle co-alignment. Reproduced from (Lange et al., 2016) with permission from Elsevier. Copyright © Elsevier, 2016.

1.4 Dissertation Outline

In this chapter, an introduction and brief review is given to fabrication of flexible electronics. Different methods of sintering are introduced and discussed, including conventional sintering, intense pulse light sintering and selective laser sintering. Enhancement with carbon nanotubes is presented to address certain issues during applications of flexible electronics. To investigate the underlying mechanisms of sintering process, application of molecular dynamics simulation in the current study of the coalescence and interaction of metal nanoparticles has also been introduced. The current dissertation outline is presented as follows:

In Chapter 2, laser-based fabrication of carbon nanotube- silver composite onto a flexible substrate is introduced. The whole fabrication process is presented, including preparation of suspension, suspension deposition and laser sintering. The sintered lines were observed with SEM. Electrical performance and fatigue performance during bending tests are also compared between lines made from laser sintering of silver NPs and laser-sintered CNT-silver composite lines.

In Chapter 3, further characterizations are performed and analyzed, such as those using TEM, EDS in STEM mode, XPS, etc, to improve the understanding of the CNT-silver interfaces in laser-sintered CNT-silver composites and the composite-polyimide substrate interface.

In Chapter 4, static tensile tests and adhesion tests of sintered films (silver films VS CNT-silver composite films) were also carried out to further characterize the mechanical performance. In-situ microscope observation was used in static tensile tests to track crack initiation and development. Ex-situ SEM images were compared to explore the mechanisms of mechanical performance enhancement due to CNTs.

Chapter 5 presents an MD model for simulating the coalescence of metal nanoparticles and their interaction with a CNT for nanoparticles initially placed around the end of the CNT at elevated temperatures that can be potentially induced by laser heating. Structural evolutions under different temperatures were visualized and characterized with statistical variables. The impact of the multiwalled CNT diameter was also compared and discussed.

Chapter 6 summarizes overall conclusions obtained from research reported in this thesis and presents some recommendations for potential future work.

2. LASER-BASED FABRICATION OF CARBON NANOTUBE – SILVER COMPOSITES WITH ENHANCED FATIGUE PERFORMANCE ONTO A FLEXIBLE SUBSTRATE

The main content of this chapter has been published in the journal article: Zheng Kang, Benxin Wu, Ruoxing Wang, and Wenzhuo Wu, Laser-Based Fabrication of Carbon Nanotube–Silver Composites With Enhanced Fatigue Performance Onto a Flexible Substrate. Journal of Manufacturing Science and Engineering, 2018, 140(9), 091005. Copyright © 2018 by ASME

As introduced in Chapter 1, various method for the fabrication of flexible electronics are the focus of ongoing research and CNT is widely recognized as a promising candidate for performance enhancement. In this chapter, a new (to our best knowledge) approach is reported for producing CNT-metal composites onto flexible substrates through laser sintering of CNTs and metal nanoparticles, which was proposed by Wu (2017). Laser sintering has several potential advantages: (1) laser spot scanning trajectories on a flexible substrate can be easily controlled, programed and changed, and different and complicated composite patterns can be flexibly produced without the need of a mask or vacuum; (2) a laser beam can be focused to a very small spot, leading to a potentially very high spatial resolution; and (3) different from a furnace, laser beam can achieve precise and localized energy delivery during sintering, with small or little undesirable thermal effects to the flexible substrate and the other surrounding regions. Although research work about laser sintering of metal nanoparticles (without CNTs) on polymer or other substrates has been performed by researchers (Ko et al., 2010; Ko, Pan, Grigoropoulos, Luscombe, Fréchet, et al., 2007b; Pan et al., 2007), the reported fabrication of CNT-metal composites onto a flexible substrate through laser sintering has been relatively rare to our best knowledge. Ji et al. (2017) reported laser sintering of conductive flexible adhesive (CFA) onto a flexible substrate. The CFA contains silver flakes, CNTs decorated by silver nanoparticles and a nitrile-butadiene-

rubber (NBR) matrix. The laser-sintered material has a conductivity as high as 25012 S cm^{-1} . As introduced later, the novel approach in this research is different from that in Ji et al. (2017) and does not use CFA. Instead, a suspension of CNTs and silver nanoparticles (without NBR matrix) in liquid is dispensed onto the flexible substrate, dried and then laser-sintered. The obtained CNT-silver composites under the studied conditions can have an electrical conductivity of $\sim 1.1 \times 10^5 \text{ S cm}^{-1}$, which is ~ 4.4 times that obtained in Ji et al. (2017).

The major goal of the work in this chapter is to verify and demonstrate the feasibility of the novel laser-based approach to produce CNT-metal composite lines onto a polymer substrate, and the effectiveness of CNTs in enhancing the bending fatigue performance of the lines on the substrate. The main content of this chapter has been published in the research article (Z. Kang, Wu, Wang, & Wu, 2018).

2.1 Experiments

2.1.1 Laser-Based Fabrication of CNT-Silver Composite Lines on a Polyimide Substrate

As shown in Figure 2.1, the fabrication process of CNT-silver composite lines onto a polyimide substrate mainly consists of the following steps:

Step 1: Preparation of CNT & silver nanoparticle (NP) suspension in ethanol.

Step 2: Dispensing of the prepared suspension onto a polyimide substrate to obtain CNT & silver NP mixture lines.

Step 3: Sintering of the CNT & silver NP mixture lines into CNT-silver composite lines through laser irradiation

Step 1: Preparation of CNT & Silver NP Suspension

In preparing the CNT & silver NP suspension, 95% ethanol has been used as the solvent, and the prepared suspension has a silver nanoparticle concentration of ~ 0.45 g/ml (that is, ~ 0.45 g for every milliliter ethanol added to the suspension). To disperse CNTs and decrease their possible agglomeration, SDS (sodium dodecyl sulfate) is used to help the dispersion of CNTs in the suspension. When mixing CNTs, SDS and silver NPs, their weight ratio is chosen to be 1:4:100, where the CNT to SDS ratio is selected based on information from L. Jiang, Gao, and Sun (2003). The CNTs are multi-walled CNTs (Product code: TNM5, Chengdu Organic Chemicals Co., Ltd, Chinese Academy of Sciences), which have diameters typically in the range of ~ 20 to 30 nm and lengths in the range of ~ 10 to 30 μm with a purity $> 95\%$ based on the information from the vendor. Figure 2.2 shows an SEM image of the silver nanoparticles (from Inframat[®] Advanced Materials[™], LLC) purchased for this work (the silver nanoparticles are put into acetone, and a certain amount of the formed suspension is dropped onto a copper tape, and the SEM observation is made after the acetone is evaporated).

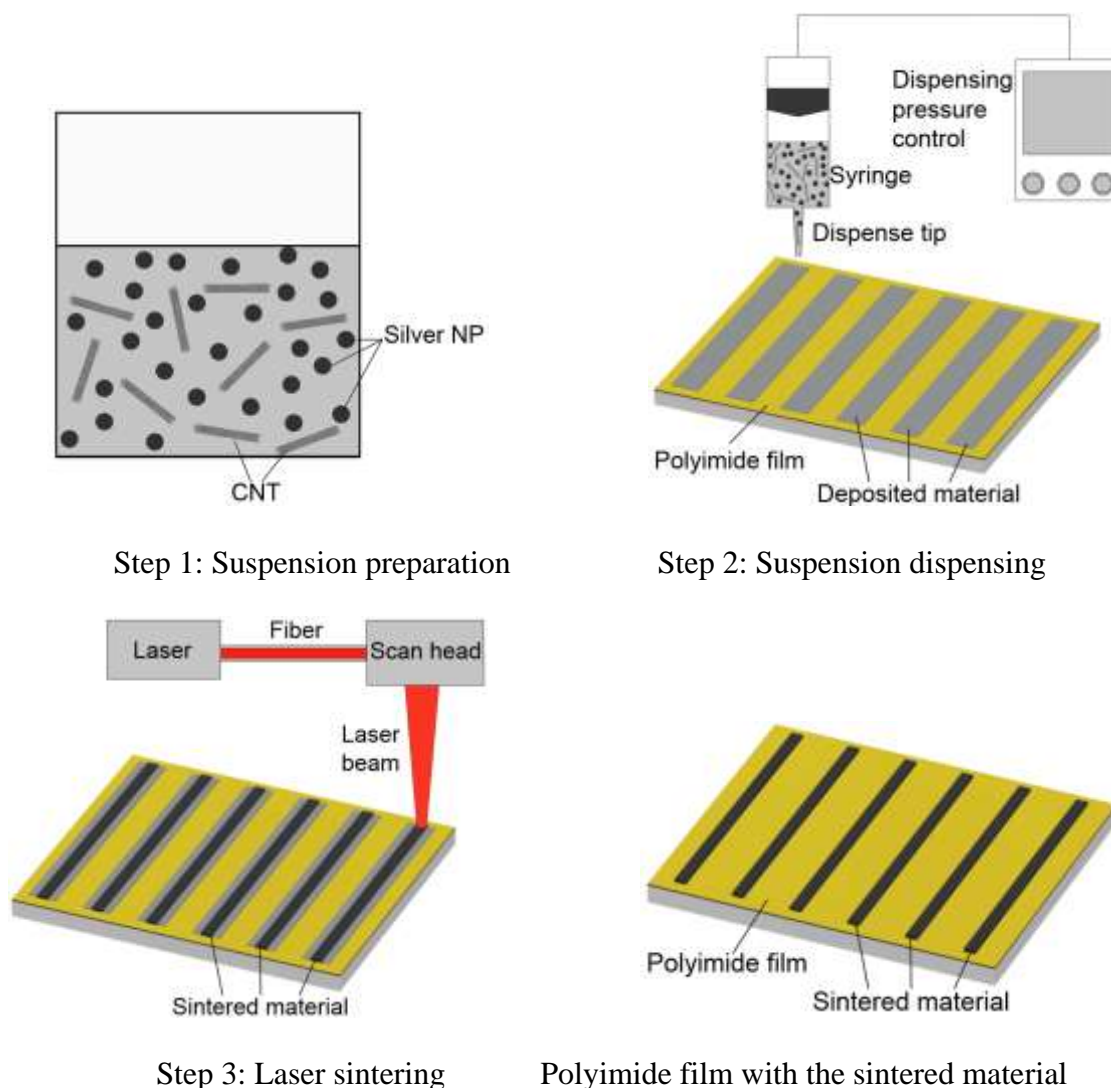


Figure 2.1 Schematic diagram of the fabrication process to produce CNT-silver composite lines onto a polyimide film (not drawn to scale, not all components or details given, and the demonstrated details not necessarily exact; there is a plastic layer below the polyimide film for mechanical support).

First, the SDS and ethanol are mixed and stirred using a magnetic stirrer for a period of 20 minutes. Next, CNTs are added and the obtained suspension is stirred using the stirrer for 10 minutes and then ultra-sonicated using an ultrasonic cleaner for 30 minutes. After this, silver nanoparticles are added to the suspension, which then go through a 3-round treatment. In each round, the suspension is stirred for 10 minutes and then treated by ultra-sonication for 30 minutes.

After the 3-round treatment, the suspension is stirred again using the magnetic stirrer for a period of ~20 minutes or longer. After this, the suspension is ready to be dispensed onto the polyimide substrate.

The suspension of silver nanoparticles in ethanol without CNTs has also been prepared following a similar procedure without using SDS and CNTs (and hence without the involved relevant steps). The prepared suspension also has a silver nanoparticle concentration of ~0.45 g/ml.

Step 2: Dispensing of the CNT & Silver NP Suspension onto Polyimide

The dispensing of the suspension onto a polyimide substrate is achieved through a Nordson EFD Ultimus II dispensing system, which is a pressure-based fluid dispensing system. The system includes a control unit, a syringe and a dispense tip (see Figure 2.1). The tip orifice used in this work has an inner diameter of 0.2 mm, and the tip – polyimide distance is typically controlled to be less than roughly around 0.1 mm during the dispensing process. The dispensing system is operated in the continuous mode with a dispense pressure of ~0.1 psi and a vacuum pullback of ~0.06 psi. During the dispensing process, the polyimide film (which is bonded onto another plastic layer through an intermediate adhesive layer for mechanical support when it comes from the vendor) is positioned on a three-dimensional (3D) motion stage, and the linear motion of the stage leads to a line of dispensed suspension on the polyimide surface. Then the polyimide samples with deposited suspension lines are kept in the ambient air for over ~24 hours to dry. After this the suspension lines become solid mixtures containing CNTs and silver nanoparticles, which are ready for the following laser sintering step. When dispensing silver NP suspensions without CNTs, the major process parameters, such as the dispense pressure and vacuum pullback applied in the dispensing device and the tip-substrate distance, are about the same. For both the suspensions with

and without CNTs, the moving velocity of the dispense tip relative to the substrate is typically in the range of ~20 mm/s to ~40 mm/s.

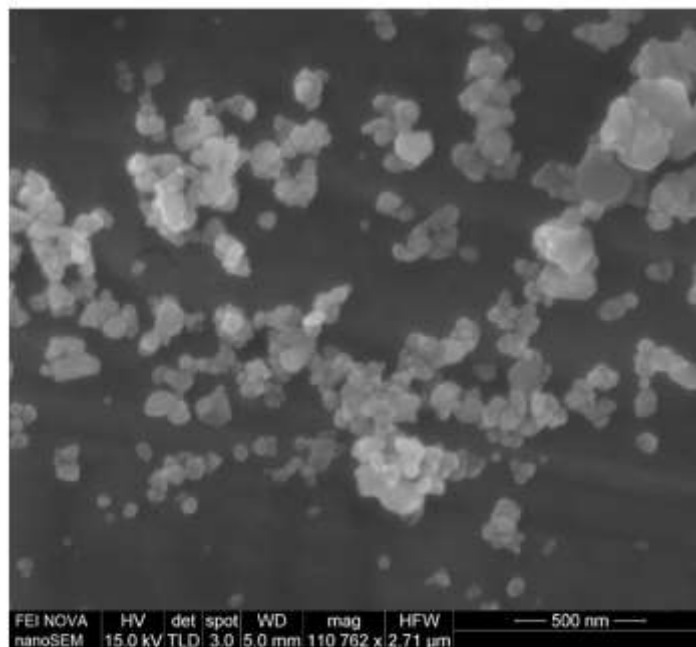


Figure 2.2 An SEM image of silver nanoparticles purchased for this work (some silver nanoparticles are put into acetone, and a certain amount of the formed suspension is dropped onto a copper tape, and the SEM observation is made after the acetone is evaporated).

Step 3: Laser Sintering of CNT & Silver NP Mixture Lines into CNT-Silver Composite Lines

The sintering of the dispensed CNT & silver NP mixture lines into CNT-silver composite lines is achieved through laser beam irradiation. The laser (SPI G3.0) used in this work is a fiber laser that can be operated in either a pulsed mode or a CW (continuous-wave) mode. In this work, the laser is operated in the CW mode with a power of around ~0.29 W to ~0.46 W. The laser beam, which has a ~1064-nm wavelength, is delivered onto the CNT & silver NP mixture line on the polyimide surface through a laser scan head (ScanLab, HurryScan 14), which has a lens with a focal length of $f = 100$ mm. During the sintering process, the sample is put in a small container

filled with argon and covered by a piece of glass, through which the laser beam can pass (the container is not drawn in Figure 2.1 for simplicity). The laser spot diameter on the sample surface is estimated to be approximately $\sim 30 \mu\text{m}$ using the knife-edge method (neglecting the effect of the aforementioned glass cover). During the sintering process, the laser spot is moved using the scan head at a speed of $\sim 20 \text{ mm/s}$ on the sample surface along the dispensed CNT & silver NP mixture line, and the laser beam irradiation can sinter the mixture line into a CNT-silver composite line on the polymer substrate. The width of laser-sintered region is typically narrower than the width of the initially deposited CNT & silver NP mixture line, and after the sintering process, the materials in the un-sintered region can be washed away using an organic solvent. During the laser sintering process, the plastic layer (as mentioned earlier) is still bonded below the polyimide film for mechanical support.

2.1.2 Characterizations

The sintered CNT-silver composites have been observed using a scanning electron microscope (SEM) (FEI NOVA nanoSEM Field Emission SEM). The electrical resistance of the sintered lines is measured using the 4-point probe method with a multimeter (Keysight Technologies Digital Multimeter 34461A). The approximate average width of a sintered line is determined through the observation using an optical microscope. The approximate average thickness of a sintered line is measured using a white-light interferometer (Bruker ContourGT). Based on the electrical resistance, the length, and the average width and thickness of a sintered line, the average electrical resistivity of the sintered line can be determined.

Fatigue bending tests of laser-sintered silver lines and CNT-silver composite lines on the polyimide substrate have been performed. Figure 2.3 shows the schematic diagram of the experimental setup for the bending test. The polyimide thin film (with laser-sintered line on its top

surface) is bonded onto a plastic support layer through an intermediate adhesive layer. The thickness of the polyimide film, the adhesive layer and the plastic support is $\sim 50 \mu\text{m}$, $\sim 10 \mu\text{m}$ and $\sim 75 \mu\text{m}$, respectively. One end of the plastic support is fixed while the other end is connected with a moving panel driven by a linear motor. The original un-deformed length of the plastic support is typically $\sim 50 \text{ mm}$. The motor drives the back-and-forth linear motion of the panel, which has a travel time of $\sim 1.3 \text{ s}$ per cycle and a total travel distance of $\sim 90 \text{ mm}$ per cycle (i.e., d_t given in Figure 2.3 is equal to $\sim 45 \text{ mm}$). During each cycle, the nearest distance between the fixed and the moving panels, d_{min} , is $\sim 2 \text{ mm}$. Hence, the smallest radius of curvature for the sintered line on the polyimide top surface is roughly estimated to be $\sim 1 \text{ mm}$ in the region near $x = 0$ during each cycle (see Figure 2.3c for the definition of $x = 0$). If it is roughly assumed that the sample's neutral axis is located at its middle-depth plane, then the maximum tensile strain in the laser-sintered line during the bending test can be approximately estimated as around $\sim 7.2\%$.

The real-time electrical resistance, $R(t)$, during each test has been measured using the two-probe method with a measurement frequency of 10 Hz (i.e., 10 measurements per second). The measured total electrical resistance includes both the resistance of the laser-sintered line and the “additional resistance” due to all the other involved components (e.g., metal wires connecting the laser-sintered line with the measurement device) and the related contact resistance. The crack generation and propagation in the sintered line (including possible sintered material loss that might be associated with the cracks) during the bending test may cause the increase of the measured electrical resistance. Based on the bending test setup, it is expected that material cracking in the sintered line will be relatively more severe in the region near $x = 0$ than the region that is relatively far away from $x = 0$. Based on microscopic observations of some samples after the bending test, it is expected that most of the major cracks should mainly occur within the region of $x = -2.5 \text{ mm}$ to

+2.5 mm as indicated in Figure 2.3c. Hence, in this study it is approximately assumed that the total electrical resistance change during the bending test, $\Delta R(t)$ ($= R(t) - R(0)$), is mainly due to the resistance change of the sintered material in the region of $x = -2.5$ mm to $+2.5$ mm, although the total length of the sintered line is typically larger (this is expected to be an approximate but reasonable assumption, and is expected to be sufficient for the purpose of the bending tests, which is to *relatively* compare the fatigue properties of laser-sintered silver lines and CNT-silver composite lines). The normalized average electrical resistivity of the sintered material in this region during the bending test can be approximately determined by:

$$\rho_N(t) = \frac{\rho_0 + \Delta\rho(t)}{\rho_0} = \frac{\rho_0 + WT\Delta R(t)/L}{\rho_0} \quad (1)$$

where ρ_0 is the initial average electrical resistivity for the laser-sintered line measured before the bending test, $\Delta\rho(t)$ is the real-time average resistivity change for the sintered material in this region, W and T are the average width and thickness of the laser-sintered line measured before the bending test, and L is the length of this region and is equal to 5 mm. The real-time total resistance change $\Delta R(t)$ can be obtained from the electrical resistance measurement in the bending test, and then based on Eq.(1) a plot of normalized electrical resistivity versus the number of bending cycles can be obtained for each bending test. As introduced earlier, each bending cycle is ~1.3-second long.

For the bending test, copper wires are bonded with the laser-sintered line using highly electrically conductive silver paint (from Ted Pella, Inc.); and then the copper wires are connected to the wires of the measurement device during each bending test. The silver paint, after being dried, can have sufficiently strong adhesions to the copper wires, the sintered line and the polyimide substrate, such that there is no contact failure during the tests for the studied cases. It should also

be noted that during the bending test, the copper wire-sample contact point is far away from the severe bending region of the sample, and hence is expected to be subject to relatively small bending-induced strains.

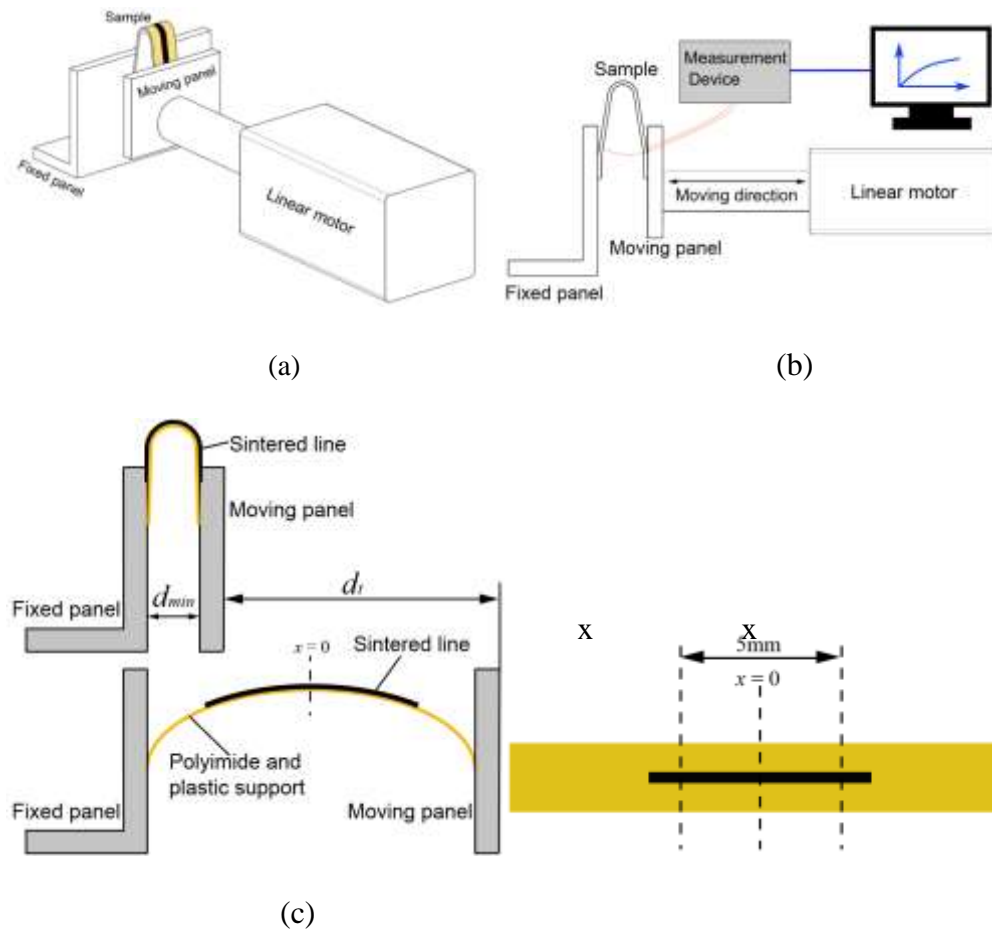


Figure 2.3 Schematic diagram of the experimental setup for the fatigue bending tests: (a) isometric view; (b) and (c) side view (not drawn to scale, not all components or details given, and the demonstrated details not necessarily exact).

2.2 Results and Discussions

In this study on the fabrication of CNT-silver composites through laser sintering, the following questions are very important and will be discussed based on the experimental results: (1) Has the laser irradiation effectively led to coalition of silver nanoparticles into a relatively more

continuous medium? (2) Do CNTs still exist in the sample after laser sintering? (3) What are the electrical resistivities of laser-sintered CNT-silver composite lines compared with silver lines? (4) How does the electrical resistivity change with the number of bending cycles during cyclic bending deformations (i.e., what is the bending fatigue performance) for laser-sintered CNT-silver composite lines compared with silver lines?

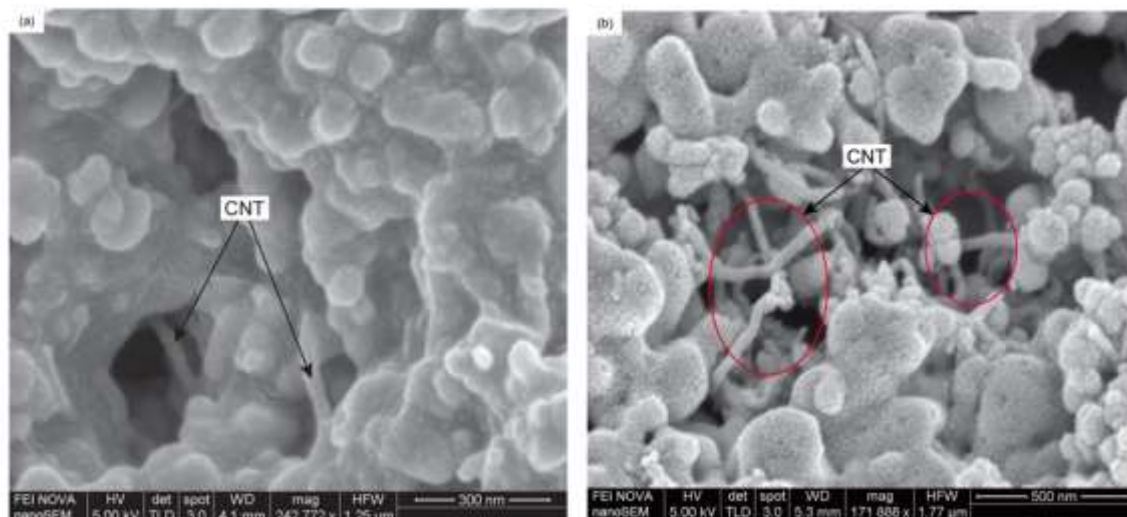
The first two questions can be answered based on the SEM images shown in Figure 2.4 for laser-sintered CNT-silver composite samples. It can be clearly seen from the SEM images that the laser irradiation during the sintering process has led to coalition of silver nanoparticles into a relatively more continuous medium, although some pores do still exist. CNTs can be clearly observed in the SEM images, and they appear to be bonded with the matrix phase in the images. The CNT-matrix bonding will be further investigated in future work.

Figure 2.5 shows the measured electrical resistivity for laser sintered CNT-silver composite lines and silver lines. The lowest average electrical resistivity in the figure for laser-sintered silver line and CNT-silver composite line is around $\sim 11 \mu\Omega\cdot\text{cm}$ and $\sim 9 \mu\Omega\cdot\text{cm}$, respectively. The values are within the electrical resistivity range obtained from the previous studies on laser sintering of silver particles (S. Hong et al., 2013; Kumpulainen et al., 2011; Theodorakos et al., 2015)(higher than those obtained in S. Hong et al. (2013) and Kumpulainen et al. (2011) and lower than that reported by Theodorakos et al. (2015)). The resistivity is a few times higher than that for bulk silver ($1.59 \mu\Omega\cdot\text{cm}$, S. Hong et al., 2013), and this is likely due to one or more factors, such as pores in the sintered material and electrical resistance due to granular boundaries (D. Zhao et al., 2012).

Figure 2.5 shows that for both single-scan and double-scan laser sintering, the electrical resistivity typically decreases as the laser power increases. One important reason is expected to be

that higher laser power can yield a better coalition of silver nanoparticles and a lower porosity in the sintered material. However, when the laser power is too high and reaches ~ 0.46 W, it has been found in the experiments that clearly observable damages can be induced on the polyimide substrate. It can also be seen from Figure 2.5 that under the same power, the double-scan sintering typically leads to a little lower electrical resistivity than the single-scan sintering. One important reason could be that when laser beam scans the sample for the second time, the laser irradiation can lead to a further enhanced nanoparticle coalition and porosity reduction.

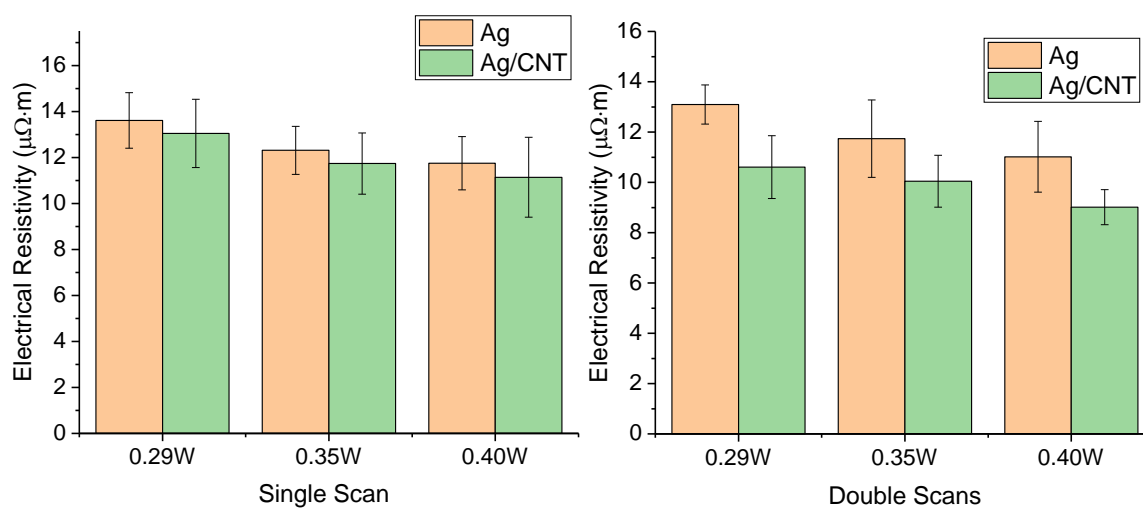
A very interesting finding from Figure 2.5 is that for all the given conditions, under the same laser power and number of laser scans, the laser-sintered CNT-silver composite lines have a lower average electrical resistivity than the laser-sintered silver lines without CNTs. For example, for the double-scan sintering results given in the figure the electrical resistivity for the CNT-silver composite lines is typically $\sim 14\%$ to $\sim 18\%$ lower than that for the silver lines without CNTs under the same laser power. The addition of CNTs may affect the electrical resistivity of the sintered material due to one or more factors that may include (but may not be limited to): (a) the CNT-silver interface in the composites may induce additional electrical resistance, and (b) the CNTs that run through the pores or granular boundaries in the sintered material may provide additional paths or channels for electrical currents to flow (D. Zhao et al., 2012). Factor (a) may increase the material electrical resistance while Factor (b) may decrease the resistance. The measurement results in Figure 2.5 imply that Factor (b) has likely played an important role in the studied cases. Certainly, future work may still be needed to better understand this interesting phenomenon.



(a)

(b)

Figure 2.4 SEM images of the sintered CNT-silver composite: (a) laser power: ~ 0.4 W, single scan; (b) laser power: ~ 0.4 W, double scans.



(a)

(b)

Figure 2.5 The measured electrical resistivity of laser-sintered silver lines and CNT-silver composite lines produced under different laser powers of ~ 0.29 W to ~ 0.40 W by: (a) single laser scan, and (b) double laser scans.

Figure 2.6 shows the normalized real-time electrical resistivity versus the number of bending cycles during fatigue bending tests for laser-sintered silver lines and laser-sintered CNT-silver composite lines on polyimide substrates. As introduced earlier, the plotted normalized electrical resistivity is for the sintered line region of $x = -2.5$ mm to $+2.5$ mm (within which most of the major cracks are expected to mainly occur), and is obtained based on the experimentally measured total electrical resistance change, $\Delta R(t)$, and Eq.(1). Each of the eight plots in Figure 2.6 gives the results for each of the eight comparison groups. Each comparison group includes one laser-sintered silver line and one laser-sintered CNT-silver composite line produced using about the same laser power, the same number of laser scans and with a similar line thickness after sintering as shown in Table 2.1.

It can be seen that in each plot in Figure 2.6 the overall trend is that the normalized electrical resistivity increases with the number of bending cycles, which is expected to be mainly due to the generation and growth of cracks in the sintered material (including possible material loss that might be associated with the cracks). It can be seen that for most of the tested cases given in Figure 2.6, the overall electrical resistivity increase is much slower for the CNT-silver composite line than the silver line in the same group (see Group 1, 3, 6, 7 and 8). If it is assumed that a fatigue life is defined as the number of bending cycles when the normalized electrical resistivity reaches 10, then the fatigue life for the lines in each group can be determined based on the data for Figure 2.6 and is given in Figure 2.7.

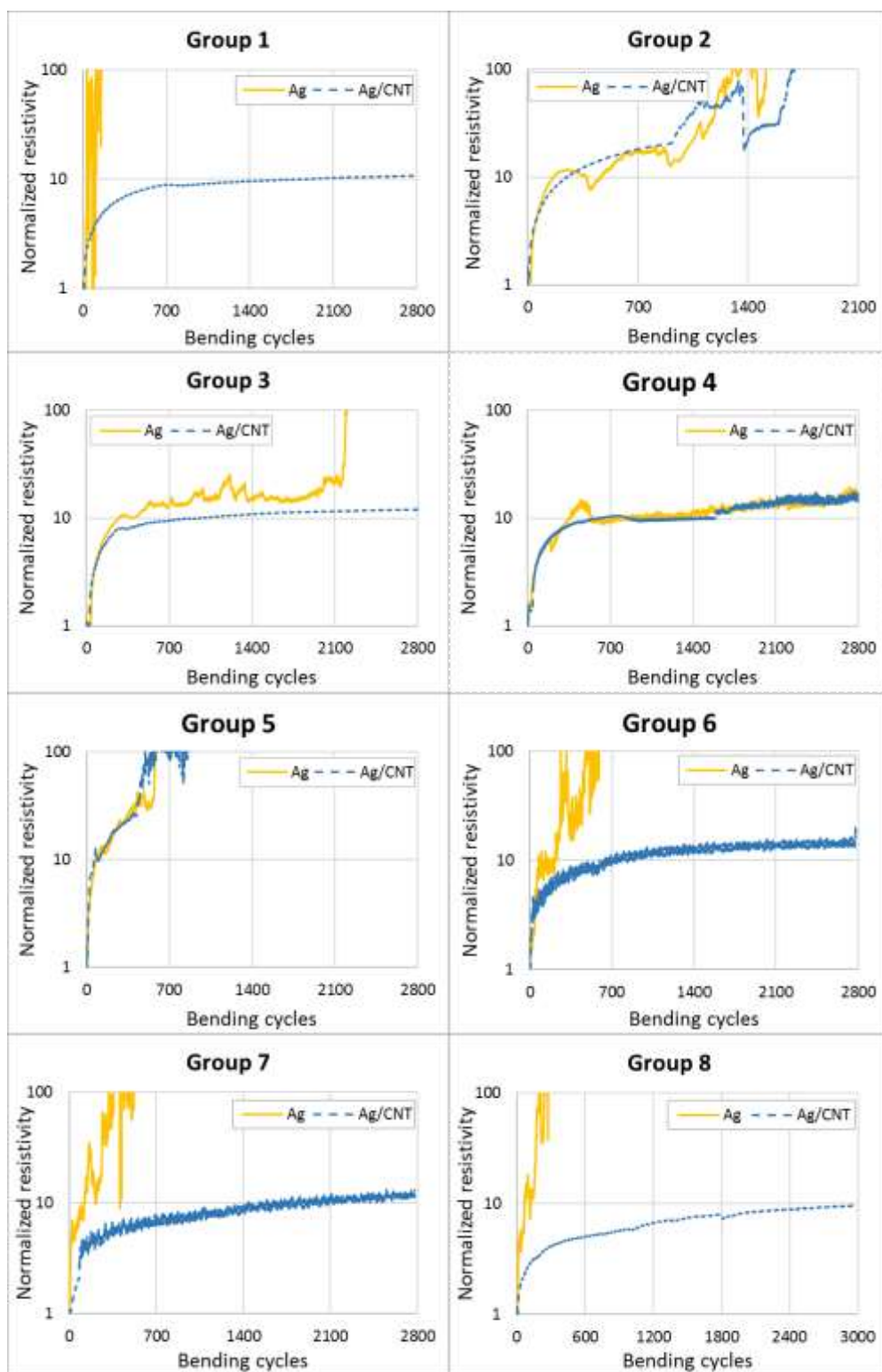


Figure 2.6 The normalized electrical resistivity versus the number of bending cycles obtained from the fatigue bending tests for laser-sintered silver lines and CNT-silver composite lines in different test groups (the “normalized” electrical resistivity is for the region of $x = -2.5$ to $+2.5$ mm for each line; the laser power, number of scans and line thickness for each group are shown in Table 2.1; data points when the normalized resistivity is above 100 are not shown).

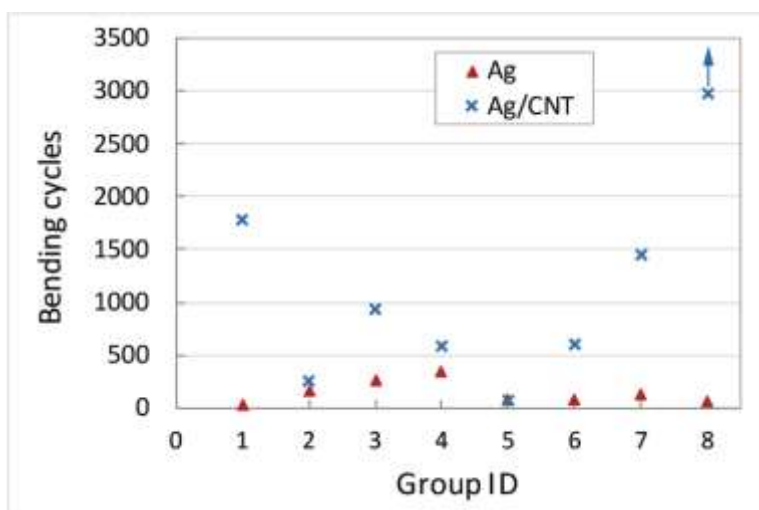


Figure 2.7 The fatigue life (in terms of the number of bending cycles) for each tested group of laser-sintered silver and CNT-silver composite lines based on the failure criterion of the normalized resistivity (as given in Figure 2.6) reaching 10 (the point with an upward-pointing arrow means that the normalized resistivity is still below the failure criterion at the maximum number of bending cycles tested in the experiment, and hence this maximum number is plotted here, but the actual fatigue life should be longer).

Table 2.1 Laser power (which is ~ 0.35 W or ~ 0.4 W), number of scans and line thickness for the eight groups of lines compared in the fatigue bending tests (the test results are shown in Figure 2.6 and 2.7).

| Group ID | Laser power(W) | Number of scans | Thickness after sintering, silver line (μm) | Thickness after sintering, CNT-silver composite line (μm) |
|----------|----------------|-----------------|--|--|
| 1 | 0.4 | Single | 0.82 | 0.81 |
| 2 | 0.4 | Single | 0.94 | 1.05 |
| 3 | 0.4 | Single | 0.86 | 0.86 |
| 4 | 0.35 | Double | 0.98 | 1.06 |
| 5 | 0.4 | Double | 1.29 | 1.26 |
| 6 | 0.4 | Single | 1.39 | 1.44 |
| 7 | 0.4 | Single | 1.28 | 1.22 |
| 8 | 0.4 | Single | 1.5 | 1.55 |

In Figure 2.7, the fatigue life of almost all the tested CNT-silver composite lines is longer than that for the silver line in the same group (except Group 5, where they are close to each other). Six out of the eight tested CNT-silver composite lines have a fatigue life longer than 500 cycles, while none of the tested silver lines has a fatigue life reaching 500 cycles. Half of the tested CNT-silver composite lines have a fatigue life that is close to or longer than ~1000 cycles. Therefore, the fatigue bending-test results in Figure 2.6 and 2.7 show that under the studied conditions and for the tested samples overall the laser-sintered CNT-silver composite lines on the polyimide substrate have a much longer bending fatigue life (as defined earlier) than the laser-sintered silver lines (in other words, the addition of CNTs has greatly enhanced the bending fatigue life of the laser-sintered material on the polyimide substrate).

Figure 2.8 and Figure 2.9 show the SEM images for the CNT-silver composite line and the silver line, respectively, for Group 7 after the bending test in certain areas within the region of $x = -2.5$ to $+2.5$ mm. The silver line has been bent for ~580 cycles, and the peak real-time normalized electrical resistivity is over 100 during the bending test. The CNT-silver composite line has been bent for ~2800 cycles, and the peak real-time normalized electrical resistivity during the bending test is still not too far from 10. Cracks can be observed in the lower-magnification SEM image on Figure 2.8 left for the CNT-silver composite line. It is expected that the cracks have contributed to the increase of the electrical resistivity. However, from the higher-magnification SEM image on Figure 2.8 right, it can be seen that there appear to be CNTs that run across the crack in the image. It is expected that these CNTs will: (1) provide channels for electrical currents to flow across the crack, and (2) help inhibit or slow down the further growth of the crack (Ahmad et al., 2010; Estili et al., 2008; Xia, Curtin, & Sheldon, 2004). These are expected to be among factors responsible for the better bending fatigue performance shown in Figure 2.6 and Figure 2.7 for the CNT-silver

composite lines. Certainly, future work may still be needed to confirm this and also check whether or not other mechanism(s) also plays an important role. Figure 2.9 shows the SEM images for the silver line, where it can be seen that the crack width in the images is larger than that in the images in Figure 2.8. Because there are no CNTs, the corresponding electrical current channels do not exist.

It should also be noted that in this study multiple samples (without or prior to bending tests) have been observed using an optical microscope at a magnification of 500 \times . The observations show that very few surface cracks (if any at all) are clearly observable for both laser-sintered silver lines and CNT-silver composite lines.

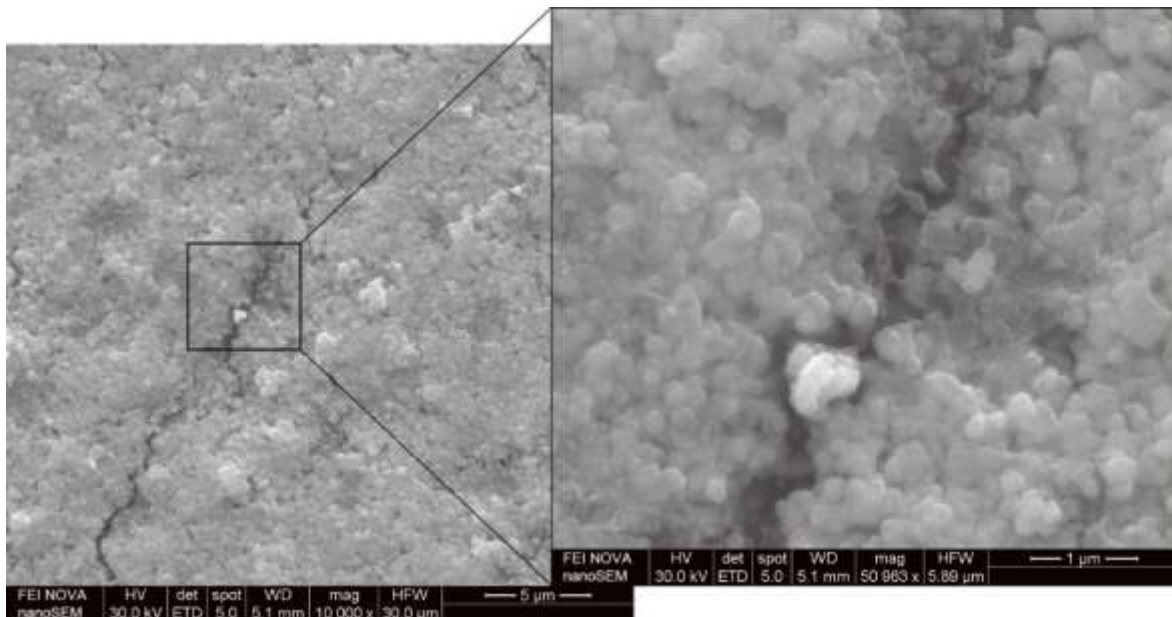


Figure 2.8 SEM images of the CNT-silver composite line in the tested Group 7 after the fatigue bending test (i.e., after being bent for ~2800 cycles).

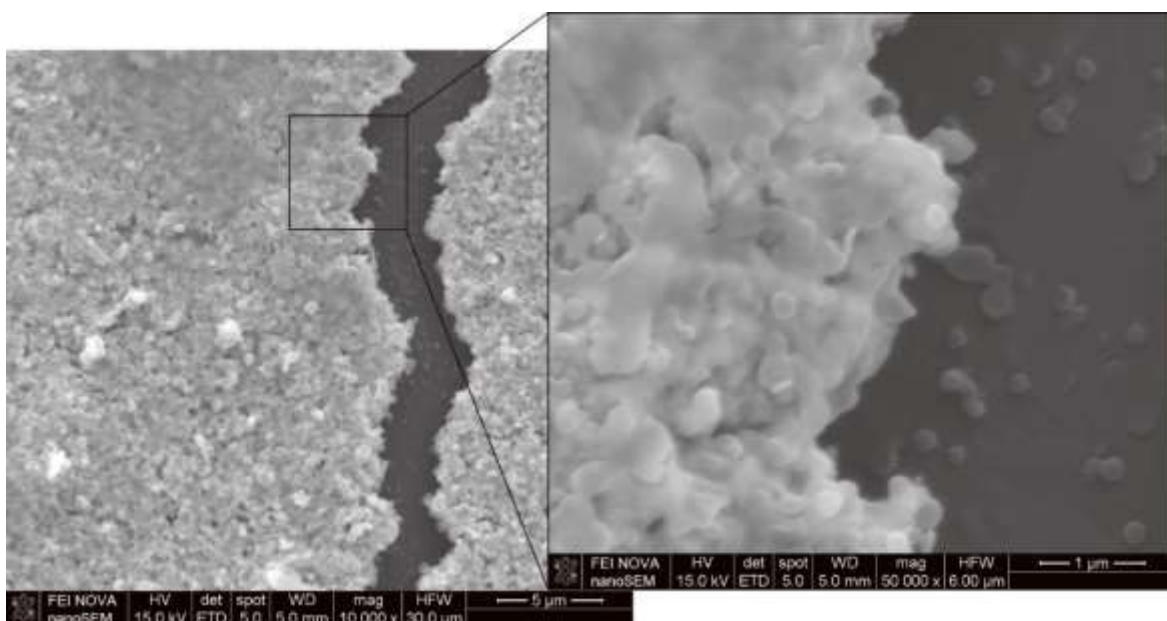


Figure 2.9 SEM images of the silver line in the tested Group 7 after the fatigue bending test (i.e., after being bent for ~580 cycles).

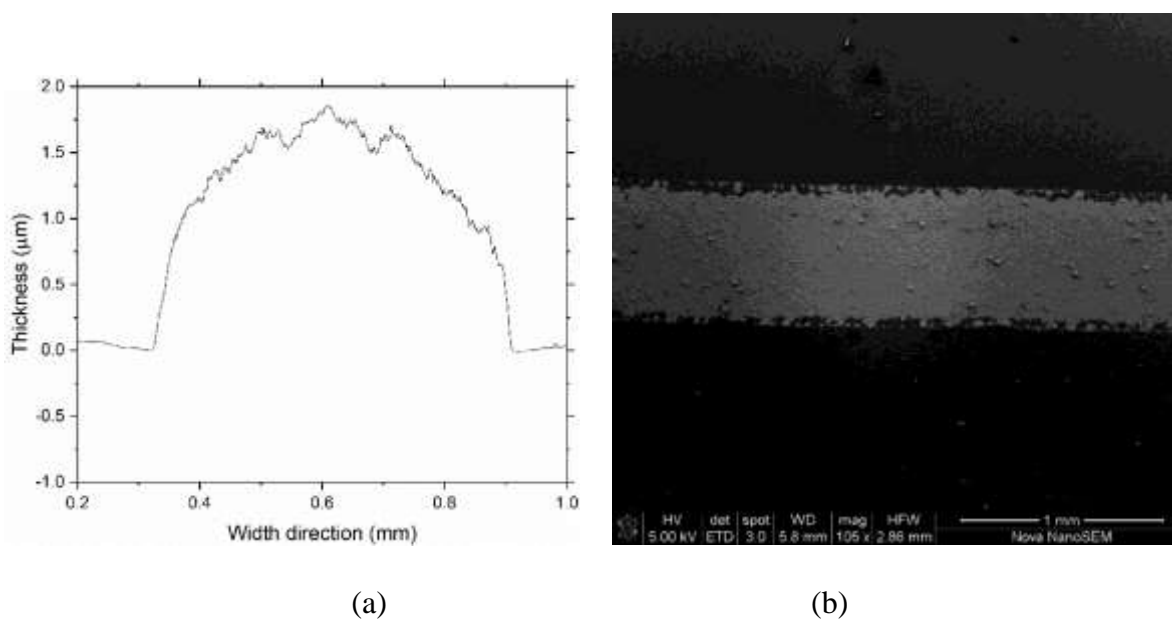


Figure 2.10 (a) Cross-section profile for an as-printed silver NP+ CNT line (an averaged profile measured using a white-light interferometer over a 0.5-mm long section of the line); and (b) SEM image of another as-printed silver NP+CNT line (the lines are dispensed onto a polyimide surface, and then dried, but not sintered).

Figure 2.10 shows an SEM image of one as-printed CNT-silver nanoparticle line and a cross-section profile for another as-printed line. The lines are dispensed onto a polyimide surface, and then dried in air, but not sintered. The cross-section profile is an averaged profile measured by a white-light interferometer over a 0.5-mm long section of the line. As mentioned earlier, the laser spot diameter on the sample surface is typically much smaller than the width of the as-printed line, and hence the eventually sintered line width is typically much narrower than that for the as-printed line. Hence, the exact width of the as-printed line does not matter much for this study. The printed line thickness is typically in the range of around ~ 1.0 to ~ 2.5 μm . For laser-sintered composite lines, Figure 2.4 shows that the CNTs and the matrix phase appear to be bonded. It is expected that the major CNT-silver bonding mechanism in the composite might be through the Van der Waals force (Feng, Yuan, & Zhang, 2005), and the exact bonding mechanism may still require further study.

2.3 Conclusions

This research has reported work on a novel laser-based approach to fabricate CNT-metal composites onto a polymer substrate. Suspensions containing CNTs and silver nanoparticles (NPs) are deposited onto the polymer substrate through a dispensing device and dried in the ambient air. Then the obtained mixture lines containing CNTs and silver NPs on the polymer are laser-sintered into CNT-silver composite lines. Under the investigated conditions and for the tested samples, it has been found:

1. The SEM observations of the laser-sintered composites show that: (a) CNTs still exist after the sintering process; (b) the sintering process has led to coalition of silver NPs, but some pores still exist; and (c) CNTs and the matrix phase appear to be bonded in the SEM images.

2. The addition of CNTs does not degrade the sintered material electrical conductivity; instead, the conductivity has even been slightly increased.
3. Overall, the laser-sintered CNT-silver composite lines have a much better bending fatigue performance than the laser-sintered silver lines.
4. It is expected that the underlying mechanisms for the observed better fatigue properties may include: (a) some CNTs could run across cracks and provide channels for electrical currents to flow across the cracks, and (b) CNTs can help inhibit the further growth of the cracks.

This study suggests that the laser-based approach of fabricating CNT-metal composites onto a flexible substrate has a great potential to enhance the durability and reliability of metallic components in flexible electronic devices without degrading their electrical properties.

3. STRUCTURAL AND INTERFACIAL CHARACTERIZATIONS OF CARBON NANOTUBE –SILVER COMPOSITE ON FLEXIBLE SUBSTRATE

The main content of this chapter comes from a journal paper under preparation: Zheng Kang, Jitendra Kumar Tripathi, Muxuan Wang, Ahmed Hassanein, Benxin Wu, Laser-Based Fabrication of Carbon Nanotube –Metal Composites on A Polymer Substrate: Experimental Study and Characterizations, a journal paper under preparation.

As introduced in Chapter 2, the CNT-silver composite lines fabricated with laser sintering have an overall improved bending fatigue performance without degrading electrical conductivity. However, to our best knowledge, the following important questions related to interfacial structures of laser-sintered CNT-metal composite films on polymer substrates have not been sufficiently studied and answered: (1) Is a significant amount of metal-carbon chemical bonds formed at the CNT-metal interfaces in the fabricated composite films? (2) What are the adhesion mechanisms at the composite film – polymer substrate interface (e.g., does the adhesion involve mechanical interlocking and/or significant metal diffusion into the polymer substrate?), and have chemical reactions occurred at the composite – polymer interface during the fabrication process?

This paper reports research work to address these questions. CNT-silver composite film lines were fabricated in a way similar to that in Chapter 2. The fabricated composite films were characterized through scanning electron microscopy (SEM), energy-dispersive X-ray spectroscopy (EDS), transmission electron microscopy (TEM) and X-ray photoelectron spectroscopy (XPS). Then, the characterization results are analyzed and discussed to answer the aforementioned important questions related to the composite interfacial structures.

3.1 Fabrication method and characterization approaches

3.1.1 Fabrication of CNT-silver composites on polyimide substrates

The fabrication approach of CNT-metal composite thin films onto polyimide substrates is similar to that reported in Chapter 2, and the major steps are introduced below (which are also illustrated in Figure 3.1):

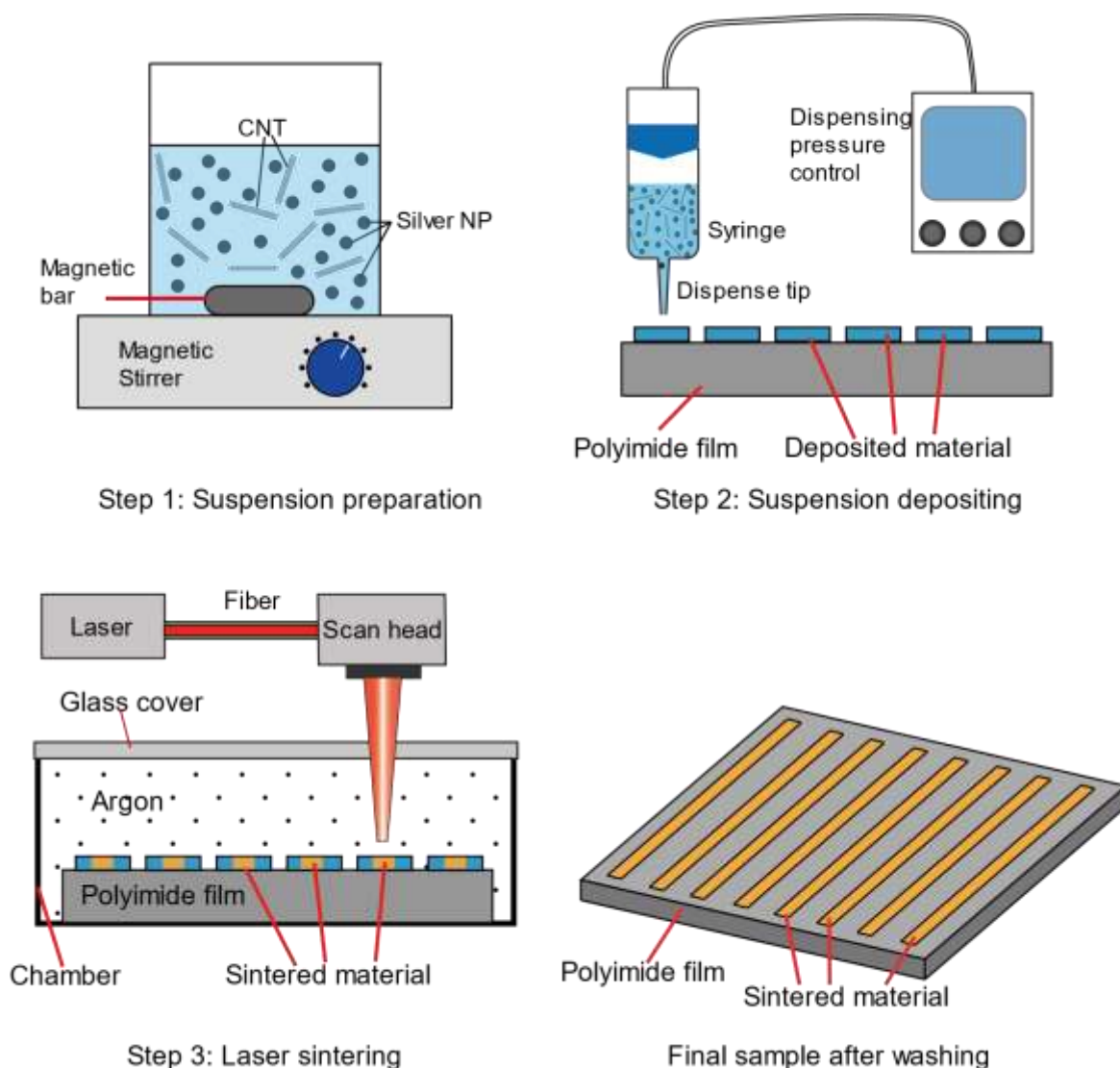


Figure 3.1 Schematic of the major procedure for laser-based fabrication of CNT-silver composite on a polyimide substrate (the chamber has an inlet and outlet for argon gas flow; not all components are shown in the schematic, which is not drawn according to the exact actual details).

1) *Step 1: Suspension preparation by mixing, stirring and ultrasonication multi-walled CNTs and silver nanoparticles in a solvent of 95% ethanol.* The silver nanoparticles were purchased from Inframat[®] Advanced Materials[™], LLC (Manchester, CT), of which an SEM image was given in Figure 3.2. The multi-walled CNTs (product code: TNM5, Chengdu Organic Chemicals Co., Ltd, Chinese Academy of Sciences, Chengdu, China) used in the composite fabrication have a purity larger than 95%, and diameters and lengths typically in the range of ~20-30 nm and the range of ~10-30 μm , respectively, based on the information from the vendor. For each 1 milliliter of the solvent, ~0.45 g of silver NPs and ~0.0045 g of CNTs were added. The typical procedure is the following: first CNTs were added to ethanol, and the obtained suspension was stirred for 10 minutes using a magnetic stirrer, and then ultrasonicated for 30 minutes in an ultrasonic cleaner. Next, silver NPs were added and treated by a three-round process. The treatment in each round involved 10-minute stirring using a magnetic stirrer followed by 30-minute ultrasonication. After this, the suspension was stirred for at least another 20 minutes before it went into the dispensing step introduced below.

2) *Step 2: dispensing of the suspension of CNTs and silver NPs onto a polyimide film.* The suspension was deposited onto a polyimide film using a Nordson EFD Ultimius II dispensing system, of which the major components were shown in Figure 3.1(step 2). The polyimide films were purchased from CS Hyde Company (Lake Villa, IL, USA), and they had a thickness of ~125 μm . The dispensing tip orifice used in this study in the system had an inner diameter of 0.2 mm, and the system was operated in the continuous mode, where a dispense pressure of ~0.1 psi and a vacuum pullback of ~0.06 psi were used. The tip-polyimide distance was typically controlled to be shorter than roughly ~0.1 mm during each dispensing process for this study. During dispensing, the polyimide film was moved using three-dimensional motion stages, and the translational

velocity of the tip relative to the polyimide was typically in the range of ~20 to ~40 mm/s. After the suspension was dispensed (typically as thin lines) onto the polyimide film, each sample was typically left in air for over ~24 hours to allow the ethanol to be evaporated. As a result, thin lines of CNT and silver NP mixtures were deposited onto polyimide films.

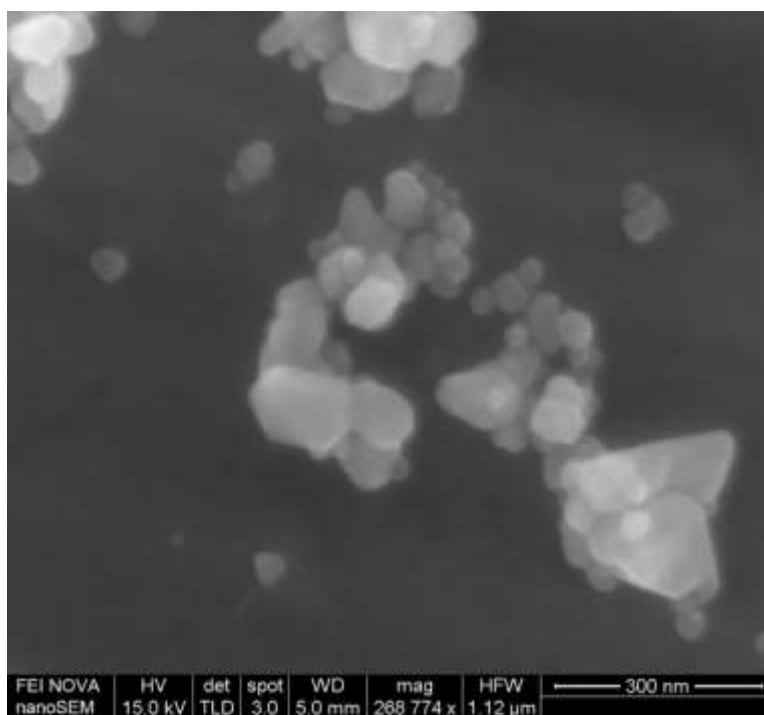


Figure 3.2 An SEM image of some silver nanoparticles (NPs) purchased to fabricate CNT-silver composites in this study (silver nanoparticles were stirred in acetone to form a suspension, several drops of which were dispensed onto a copper tape. Then the SEM image was taken after acetone on the copper tape was evaporated).

3) *Step 3: Laser sintering of CNT and silver NP mixtures into CNT-silver composites on the polyimide film.* The laser sintering processes were performed using a fiber laser (SPI G3.0), which was operated in the continuous-wave (CW) mode at a power of ~0.4 W. The laser beam had a wavelength of ~1064 nm. It was delivered by a scan head (ScanLab, HurryScan 14, with a lens that has a focal length of $f = 100$ mm) onto the sample surface with a spot size of approximately ~30 μm . The sample was placed in a chamber covered by a piece of glass that permitted the laser

beam to pass through. Argon gas was flowed into the chamber to protect the sample surface. During laser sintering, the laser spot moving speed on the sample surface was ~20 mm/s, and each line of the CNT and silver NP mixture was typically laser-scanned for four times. The laser-sintered region was normally narrower than the width of the initially deposited line. After laser sintering, the residual material in the un-sintered region of each line was washed away using an organic solvent. As a result, CNT-silver composite lines were fabricated onto polyimide film substrates.

3.1.2 Sample Characterizations

The sintered line electrical resistance, R , was measured with the four-point probe method using a multimeter (Keysight Technologies Digital Multimeter 34461A). The approximate average width and thickness of a sintered line, W and T , were measured through a white-light interferometer (Bruker ContourGT). Then the average electrical resistivity of the material in a sintered line, ρ , can be determined by:

$$\rho = \frac{W T R}{L} \quad (1)$$

where L is the length of the sintered line that can be easily measured.

SEM observations of CNT-silver composite samples were conducted using an FEI NOVA nanoSEM Field Emission SEM. EDS measurements through the SEM system were also performed. In addition to the top surfaces, the bottom surfaces of some CNT-silver composite lines (i.e., the surface adhered with the polyimide substrate) were also observed or measured with SEM and/or EDS (see Figure 3.3a for the definition of the top and bottom surface). The bottom surface of a laser-sintered CNT-silver composite line was exposed by peeling the line off from the polyimide film (as shown in the schematic in Figure 3.3b) through the following steps: 1) Strong glue (Loctite

Super Glue Ultra Gel) was applied on a piece of glass slide; 2) The top surface of a sintered CNT-silver composite line (on a polyimide film) was pressed onto the glass slide; 3) After the glue was fully cured (which then strongly connected the composite line top surface with the glass), the polyimide film was peeled off continuously and quickly from the composite line bottom surface. As a result, the composite line bottom surface was exposed.

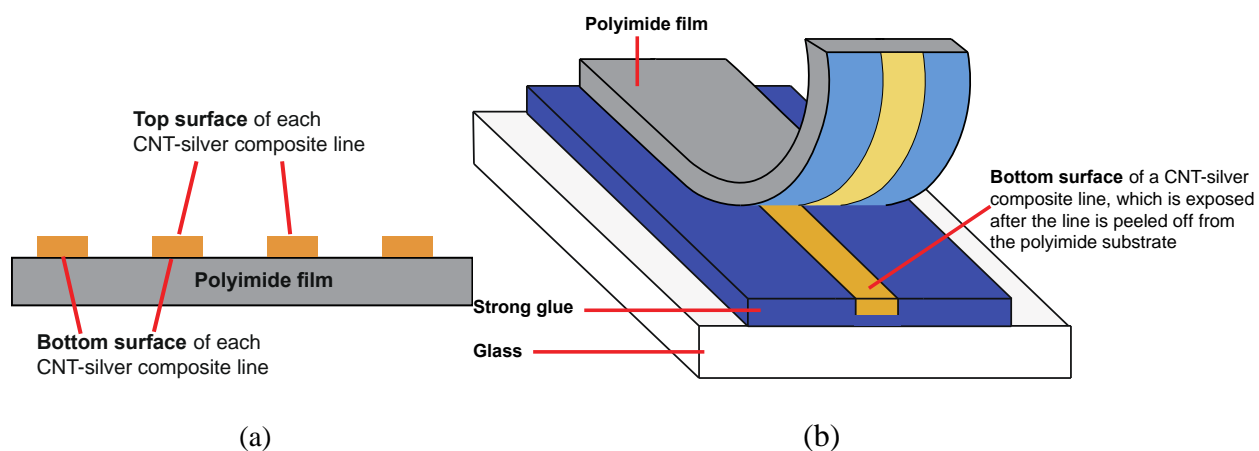


Figure 3.3 Schematics of: (a) the definition of the top and bottom surface of each CNT-silver composite line in a cross-sectional view; and (b) the setup to expose the bottom surface of a CNT-silver composite line by peeling the line off from the polyimide substrate.

TEM observations of a sample cross-section were conducted using a FEI Tecnai G2 20 Transmission Electron Microscope, which is a 200 KV LaB6 filament (S)TEM and includes a Fischione HAADF detector for STEM and an Oxford Instruments X-MAX SDD EDX detector (based on information from: <https://ag.purdue.edu/arce/Microscopy/Pages/TransmissionElectron.aspx>). EDS measurements in the STEM mode were conducted to obtain the elemental composition information at different locations across the composite – polyimide interface. The samples for TEM observations were prepared based on LR White (Medium) resin from Electron Microscopy Sciences (Hatfield, PA). The samples (i.e., CNT-silver composite lines on polyimide substrates) were put in a standard gelatin capsule and cured under the room temperature in a reflective

chamber using UV light (and the capsule was capped). The ultramicrotomy was performed on a Leica UC6 ultra microtome (Vienna, Austria). Semi-thin sections of the samples were cut at 500nm, and then they were heat fixed to a standard microscope slide and stained with toluidine blue. After this, selected areas of the CNT-silver composite samples were trimmed to 1mm x 1mm squares, sectioned at a thickness of 85nm for the TEM observation and put on 100-mesh formvar copper grids. The spot size of the electron beam used for the EDS measurements of the composite samples was estimated to be approximately ~28nm by focusing the electron beam with a condenser lens and taking direct images of the spot.

X-ray photoelectron spectroscopy (XPS) measurements were performed using a Kratos AXIS Ultra DLD Imaging X-ray photoelectron spectrometer for: (i) the top surface of a line of CNT and silver NP mixtures dispensed onto a polyimide substrate but not sintered (called Sample (a) in the discussion later on), (ii) the top surface of a laser-sintered CNT-silver composite line (Sample (b)), and (iii) the bottom surface of a laser-sintered CNT-silver composite line (which was exposed in a way as described earlier and shown in Figure 3.3b). The XPS measurements were based on monochromatic Al K α X-rays (1486.6 eV), and the X-ray spot size on the sample surface was about 110 μ m. The depth of probing for an XPS measurement is typically about 10 nm (Mather, 2009; Fairley & Casa, 2009).

3.2 Results and Discussions

In Section 3.2.1, the characterization results will be introduced; and then in Section 3.2.2 the results will be further analyzed to answer the aforementioned important questions on the CNT-metal interfaces in the composite and on the composite-polyimide substrate interface.

3.2.1 Introduction to Characterization results

3.2.1.1 SEM and EDS

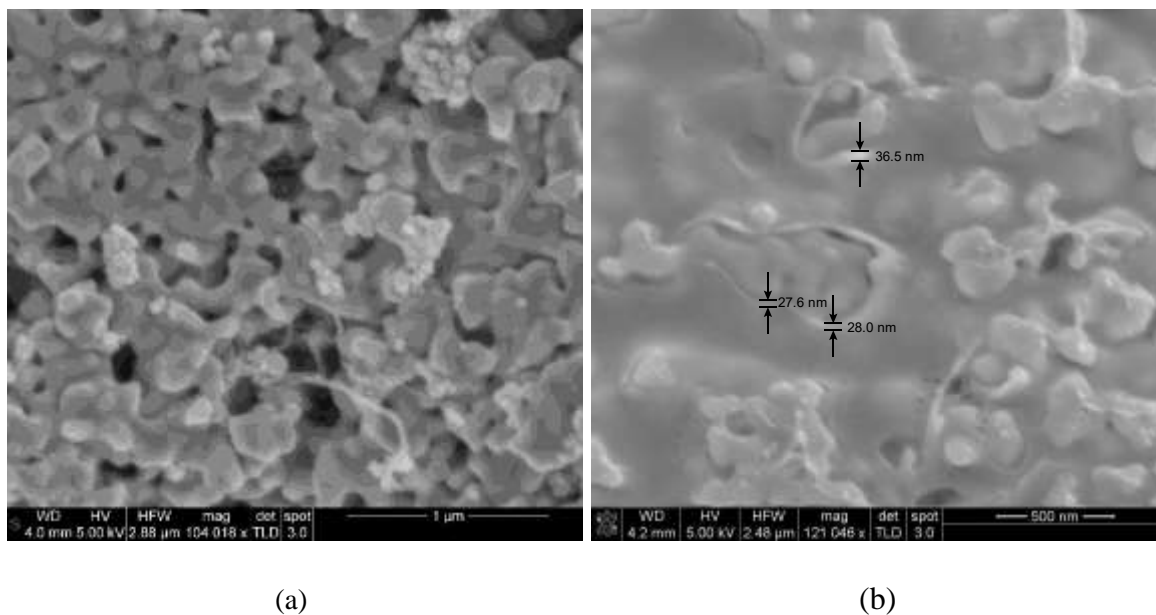


Figure 3.4 SEM images of: (a) the top surface of a laser-sintered CNT-silver composite line on a polyimide substrate; and (b) the bottom surface of a CNT-silver composite line, after the composite is peeled off from the polyimide substrate (the bottom surface is tilted by 25° in the image). The average electrical resistivity was measured to be $\sim 10.2 \mu\Omega\cdot\text{cm}$ for the whole group of CNT-silver composite line samples prepared for characterizations, where the average thickness of the group of composite lines was $\sim 1.49 \mu\text{m}$. The two images shown above are from two different samples.

Figure 3.4a and b show the SEM images for the top surface of a laser-sintered CNT-silver composite line and the bottom surface of another composite line (exposed in the way as described earlier and demonstrated in Figure 3.3b). From the image in Figure 3.4a for the top surface, it can be seen that the laser sintering process has induced coalition of silver NPs into a more continuous solid medium, while CNTs are still clearly observable, which extend among the silver medium. From the image in Figure 3.4b for the bottom surface of a composite line, it appears that the exposed bottom surface is partially covered by a thin film of material, which is expected to come from the polyimide substrate. The image was taken by tilting the bottom surface for 25°. The film

thickness that appears in the image is roughly ~ 27 to ~ 37 nm in the three locations labeled in the image. Hence, the actual thicknesses of the thin film at these locations are estimated to be in the range of ~ 60 to ~ 90 nm. This is certainly a very rough estimation due to uncertainties in the actual surface orientations at different locations, etc. However, from observations conducted, it is expected that the thickness of the film is typically very small, although it may have some variations at different locations of one sample and for different samples.

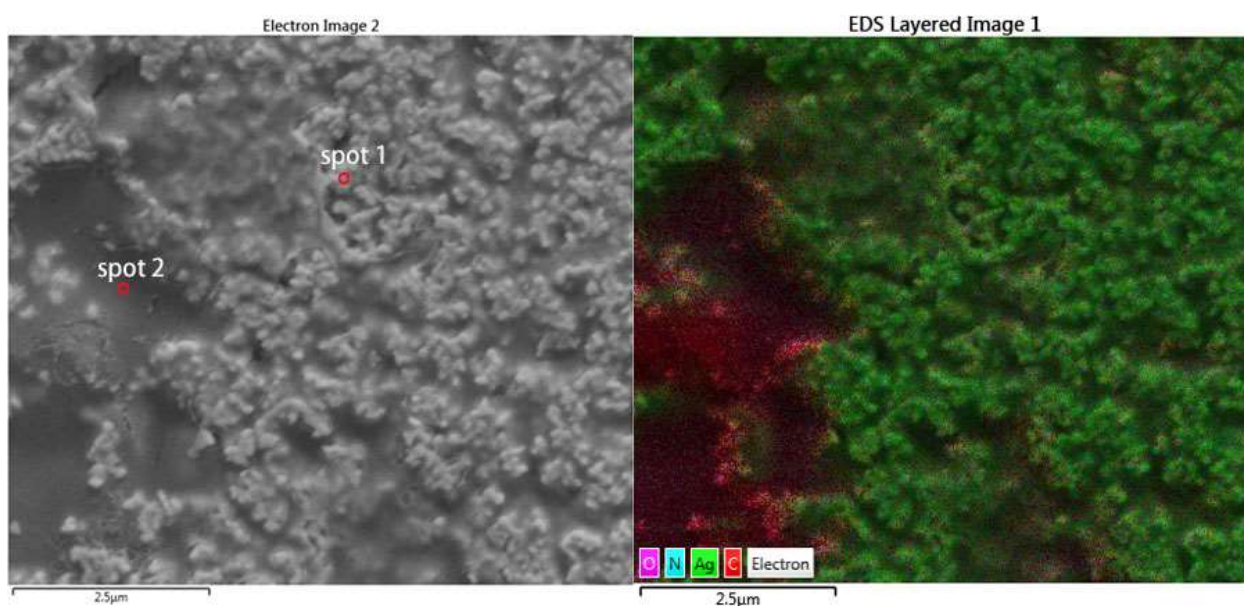


Figure 3.5 (left) An SEM image for a region of the bottom surface of a CNT-silve composite line (where the bottom surface is exposed in the way shown in Figure 3.3b); and (right) an image showing the distributions of some elements measured by EDS for the region.

Figure 3.5 shows an SEM image for a region of the bottom surface of a laser-sintered composite line, together with an image showing elemental distributions measured by EDS for the region. The images show that the bottom surface is covered (at least partially) by a thin film of material that is expected to come from the polyimide substrate. Film-covered regions like those around Spot 2 have high carbon concentrations, while regions like those around Spot 1 have high

silver concentrations, which should be either not covered by a thin film, or covered by a film whose thickness is much smaller than the EDS probing depth.

3.2.1.2 TEM and EDS in STEM Mode

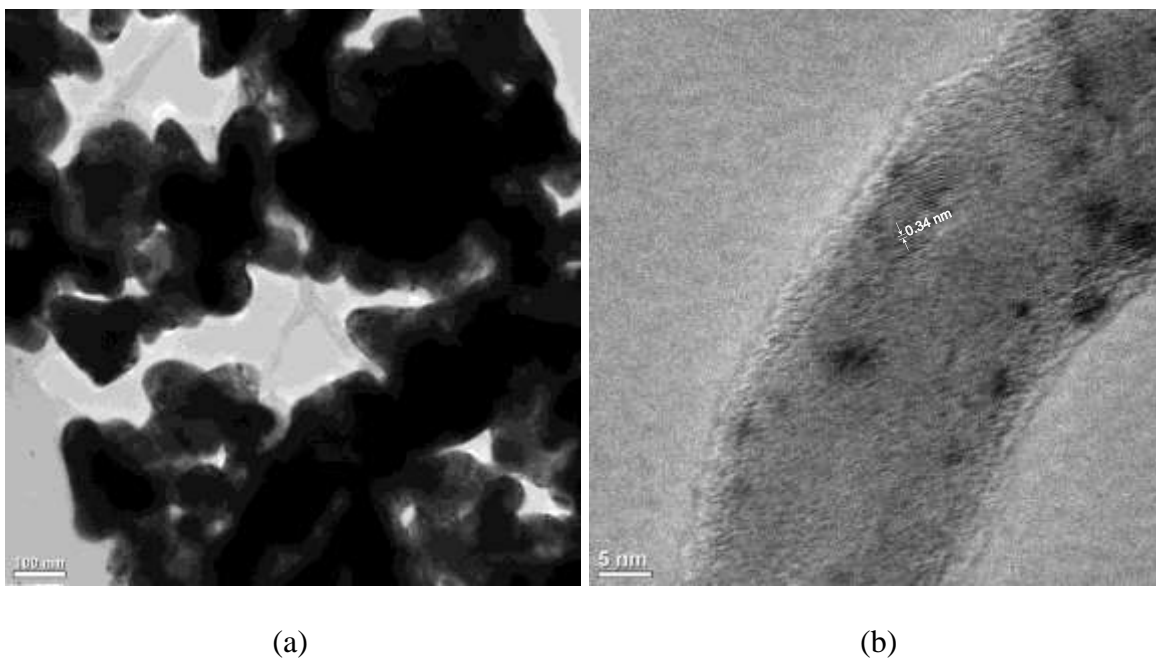


Figure 3.6 TEM image of a region in the cross-section of a laser-sintered CNT-silver composite sample (a), and TEM image of a CNT in the composite at a higher magnification (b).

Figure 3.6a shows a TEM image of a region in the cross-section of a laser-sintered CNT-silver composite sample. Similar to the SEM image in Figure 3.4a, the TEM image also shows coalition of silver NPs and the existence of CNTs that extend among the silver medium. Figure 3.6b shows a TEM image of CNT in the composite at a higher magnification. The CNT diameter that appears in the image is well consistent with the original CNT nominal diameter range based on the information from the CNT vendor. The image shows that a fringe distance of ~ 0.34 nm is obtained at the labeled location, which is consistent with the typical interlayer distance of a multiple-walled CNT (Georgantzinis & Anifantis, 2009).

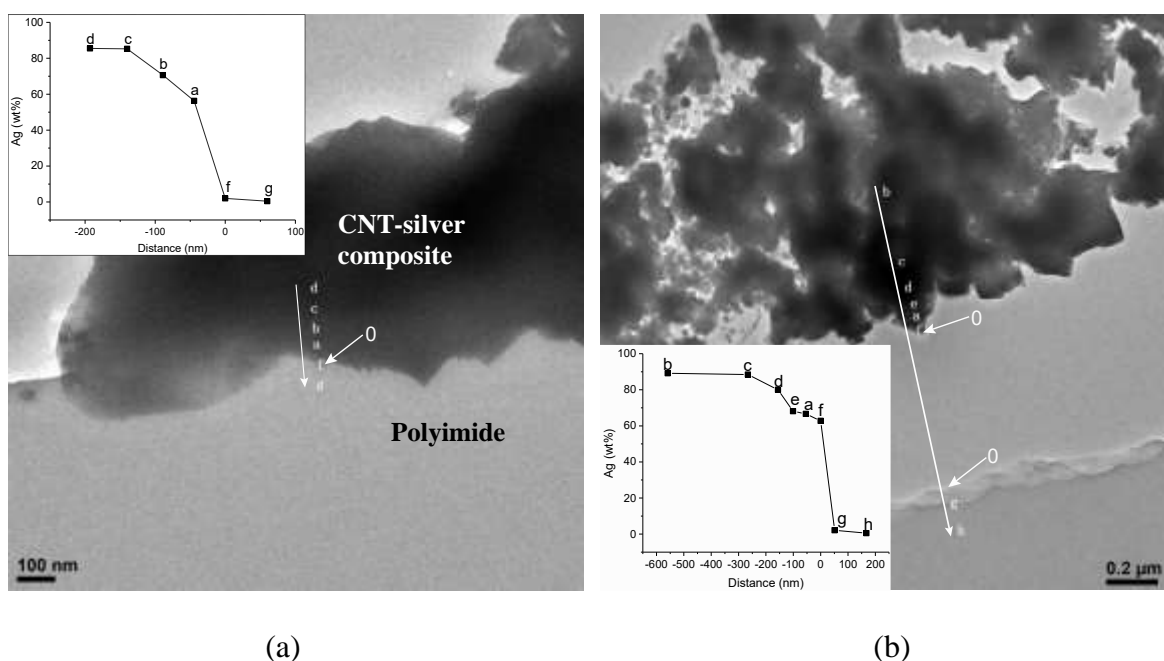


Figure 3.7 TEM images of the cross-section of a laser-sintered CNT-silver composite line on a polyimide substrate: (a) for a portion near the composite line side boundary; and (b) for a more central region of the line. The insets show silver weight percentage from EDS analysis performed in the STEM mode for multiple points approximately labeled on each TEM image.

Figure 3.7 shows TEM images for a cross-section of a laser-sintered CNT-silver composite line on a polyimide substrate. The cross-section plane shown in the images is perpendicular to the length direction of the laser-sintered line. Figure 3.7a is an image for the region near the side boundary of the line, while Figure 3.7b is an image for a more central region that is a little bit away from the boundary. In addition, the inset in each TEM image shows the silver elemental percentage measured by EDS (in the STEM mode) for multiple points that are roughly on a line approximately perpendicular to the composite-polyimide interface.

The CNT-silver composite layer in Figure 3.7a remains attached with the polyimide substrate, while that in Figure 3.7b is separated from the polyimide substrate. The separation should be induced by the TEM sample preparation process using ultramicrotomy, and is likely due to the significant difference in mechanical properties between the composite and the polyimide

substrate. In the insets for Figure 3.7, for each data point, the approximate corresponding EDS measurement location is indicated by a letter and marked in the TEM image. For each TEM image, the multiple EDS measurement locations are approximately on the same line that is roughly perpendicular to the composite-polyimide interface (assuming that for Figure 3.7b the composite side and the polyimide side have little lateral movements relative to each other during their separation process). The electron beam spot size used for the EDS analysis is about 28 nm. The analysis and discussions about the TEM and EDS results in Figure 3.7 will be given in Section 3.2.2.

3.2.1.3 XPS Analysis

As introduced earlier, XPS measurements were performed for: (a) the top surface of a line of CNT and silver NP mixtures dispensed onto a polyimide substrate but not sintered (called Sample (a)); (b) the top surface of a laser-sintered CNT-silver composite line (Sample (b)); and (c) the bottom surface of a laser-sintered CNT-silver composite line (exposed in the way as described earlier) (Sample (c)). The XPS results, together with deconvoluted spectra, are shown in Figure 3.8. The XPS survey spectra are shown on the top left side of Figure 3.8 (Fairley & Casa, 2009), while the high-resolution spectra around the binding energies for C 1s, Ag 3d and O 1s are shown on the top right, bottom left and bottom right side of the figure, respectively. For each group of spectra, the first, second and third row corresponds to the aforementioned Sample (a), (b) and (c), respectively. The deconvoluted XPS peaks and the corresponding chemical states identified based on analysis and information from the literature (Jackson & Nuzzo, 1995; Grunze & Lamb, 1988; Louette et al., 2005; Tjeng et al., 1990; Gaarenstroom & Winograd, 1977; Kaushik, 1991; NIST, 2001; Beamson & Briggs, 1992) are listed in Table 3.1. The atomic percentages of different states of silver deduced from the XPS measurement results are given and compared in Table 3.2.

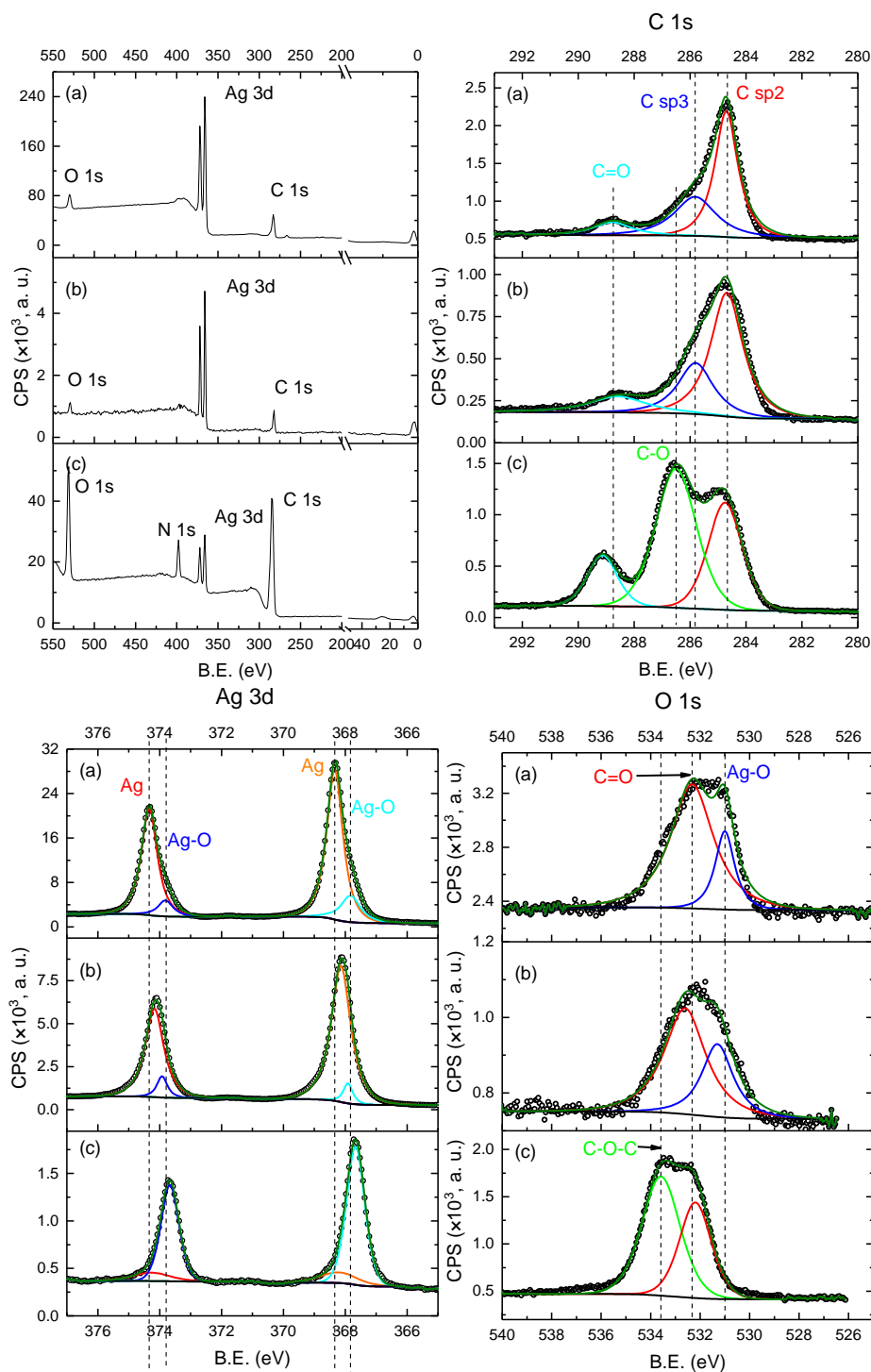


Figure 3.8 XPS results: survey spectra (the top left group), high-resolution spectra around C 1s peaks (the top right group), Ag 3d peaks (bottom left group) and O 1s peaks (bottom right group). For each group of spectra, Row (a), (b) and (c) are results for Sample (a) (top surface of a CNT and silver NP mixture before sintering), Sample (b) (top surface of a sintered CNT-silver composite line) and Sample (c) (exposed bottom surface of a sintered CNT-silver composite line), respectively. In spectra plots for C 1s, for simplicity “C=O” is used to roughly represent carbonyl carbon and “C-O” to represent aromatic carbon connected with an ether oxygen, respectively. In plots for O 1s, for simplicity “C-O-C” is used to roughly represent ether oxygen.

Table 3.1: Summary of the binding energy (BE) and the full-width at half-maximum (FWHM) (in the unit of eV) for each deconvoluted peak in the high-resolution XPS spectra in Figure 3.8 and the corresponding chemical state identified, for Sample (a), (b) and (c), respectively

| | | Ag 3d5/2 | | Ag 3d3/2 | | C 1s | | | | O 1s | | |
|------------------------------------|------|-------------------|--------|-------------------|--------|-------------------|-------------------|-------|--------|-------------------|--------|--------|
| | | Ag ₂ O | Ag | Ag ₂ O | Ag | C sp ² | C sp ³ | C-O | C=O | Ag ₂ O | C=O | C-O-C |
| Top before sintering; Sample (a) | BE | 367.83 | 368.34 | 373.81 | 374.33 | 284.7 | 285.82 | - | 288.78 | 531 | 532.32 | - |
| | FWHM | 0.75 | 0.61 | 0.58 | 0.6 | 0.97 | 1.75 | - | 1.62 | 0.92 | 2.04 | - |
| Top after sintering; Sample (b) | BE | 367.91 | 368.14 | 373.92 | 374.17 | 284.68 | 285.8 | - | 288.57 | 531.3 | 532.61 | - |
| | FWHM | 0.35 | 0.74 | 0.4 | 0.7 | 1.36 | 1.48 | - | 2.39 | 1.48 | 1.98 | - |
| Bottom after sintering; Sample (c) | BE | 367.66 | 368.2 | 373.67 | 374.26 | 284.75 | - | 286.5 | 289.14 | - | 532.19 | 533.58 |
| | FWHM | 0.7 | 1.46 | 0.68 | 1.43 | 1.43 | - | 1.72 | 1.26 | - | 1.52 | 1.81 |

Table 3.2: Atomic percentage of different chemical states of silver deduced from the XPS results in Figure 3.8(the bottom left group) for Sample (a), (b) and (c) respectively.

| Chemical state | at.% top before sinter Sample (a) | at.% top after sinter Sample (b) | at.% bottom after sinter Sample (c) |
|--------------------------|-----------------------------------|----------------------------------|-------------------------------------|
| Ag ₂ O, 3d5/2 | 10.68 | 4.01 | 50.93 |
| Ag ₂ O, 3d3/2 | 5.05 | 4.75 | 34.63 |
| Ag, 3d5/2 | 49.46 | 56.38 | 8.16 |
| Ag, 3d3/2 | 34.81 | 34.86 | 6.27 |

For sample (a), the top surface of a mixture of CNTs and silver NPs before laser sintering, the deconvoluted peaks at 284.70 eV, 285.82 eV and 288.78 eV can be recognized as peaks for C 1s in sp² bonded carbon, sp³ bonded carbon (Jackson & Nuzzo, 1995) and carbonyl carbon (which may be roughly written as C=O in this paper for simplicity) (Grunze & Lamb, 1988; Louette et al., 2005), respectively, because they appear to be reasonably close to the corresponding peak locations mentioned in the references cited. The deconvoluted silver peaks can be identified as those for Ag 3d in the metal state of silver (Ag) and in the oxidized state (Ag₂O) (Tjeng et al., 1990; Gaarenstroom & Winograd, 1977; Kaushik, 1991). From the XPS result, it can be deduced that silver atoms in the metal state (Ag) make up roughly about 84 at.% of all silver atoms in the

measured region of the top surface (Fairley & Casa, 2009). The spectrum peaks identified for carbon and silver are consistent with those for oxygen, which can be identified as the peaks for O 1s in Ag₂O and C=O (Grunze & Lamb, 1988; Louette et al., 2005; Kaushik, 1991).

For Sample (b), the top surface of a laser-sintered CNT-silver composite line, the C 1s peaks can still be identified as those for sp² bonded carbon, sp³ bonded carbon and carbonyl carbon, respectively, because they still appear to be reasonably close to the corresponding peak locations (Jackson & Nuzzo, 1995; Grunze & Lamb, 1988). Silver peaks can be identified as those for Ag 3d in the metal state of silver (Ag) and in the oxidized state (Ag₂O) (Tjeng et al., 1990; Gaarenstroom & Winograd, 1977; Kaushik, 1991). It can be deduced from the XPS result that silver atoms in the metal state (Ag) represent roughly ~91 at.% and those in the oxidized state (Ag₂O) represent roughly ~9 at.% of all silver atoms in the measured region. The percentage of silver atoms in the form of Ag and that in the form of Ag₂O for Sample (a) are correspondingly similar to (or at least do not significantly differ from) those for Sample (b) as shown in Table 2. The deconvoluted oxygen peaks for Sample (b) have a shift of ~0.3 eV relative to those for Sample (a), but they are still reasonably close to the corresponding peak locations for C=O and Ag₂O reported in literature (Louette et al., 2005; Kaushik, 1991), and hence can still be identified as these species.

For Sample (c), silver peaks can still be identified as those for the metal state of silver (Ag) and the oxidized state (Ag₂O) (Tjeng et al., 1990; Gaarenstroom & Winograd, 1977; Kaushik, 1991). However, the percentage of silver atoms in the form of Ag and Ag₂O deduced from the XPS result is roughly ~14 at.% and ~86 at.%, respectively, which shows that most of the silver atoms exist in the form of Ag₂O, instead of Ag as for Sample (a) and (b). Compared with Sample (a) and (b), for Sample (c) the oxygen peak for Ag₂O is not clearly observable while a new peak

at 533.58 eV shows up, which can be identified as the peak for O 1s in ether oxygen (which may be roughly written as C-O-C in this paper for simplicity) that is expected to initially come from the polyimide film (Grunze & Lamb, 1988; Louette et al., 2005). The missing of the O 1s peak for Ag₂O is likely due to the following: as introduced earlier, it is expected that a thin film of material coming from the polyimide substrate at least partially covers the exposed bottom surface of the CNT-silver composite (Sample (c)). As a result, the XPS elemental analysis based on the survey spectrum in Figure 3.8 shows that silver atoms only make up roughly ~2 at.% of all the atoms in the XPS-measured region of Sample (c). Therefore, the signal for the O 1s peak in Ag₂O could be much weaker than (and hence overwhelmed by) those for the O 1s peaks in C=O and C-O-C that may come from the polyimide substrate.

3.2.2 Analysis and Discussions on Characterization Results

In Section 3.2.1, the characterization results using SEM, TEM, EDS and XPS have been introduced. Next, these results will be analyzed and discussed to improve the understanding of the CNT-silver interface in the fabricated composite and the composite-polyimide interface.

3.2.2.1 CNT-Silver Interfaces in the Composite

For the CNT-silver interfaces in the composite, one major question to answer is whether a significant amount of Ag-C chemical bonds is formed at the interfaces during laser sintering. The answer is likely to be “No” based on the analysis and comparison of the XPS results for the sample before laser sintering (Sample (a)) and that after laser sintering (Sample (b)):

(1) For Sample (a) (i.e., a mixture of CNT and silver NPs before laser sintering), there should not be any significant amount of Ag-C chemical bonds on its top surface. As introduced earlier, the Ag 3d peaks can be identified as those in Ag and Ag₂O, because the peak locations appear to be reasonably close to the corresponding peak locations reported before (Tjeng et al.,

1990; Gaarenstroom & Winograd, 1977; Kaushik, 1991). For the top surface of Sample (b) (i.e., CNT-silver composite after laser sintering), although the locations of the silver peaks have slightly shifted, they can still be identified as those for Ag and Ag₂O, because they are still reasonably close to the corresponding peak locations reported in literature (Tjeng et al., 1990; Gaarenstroom & Winograd, 1977; Kaushik, 1991). In other words, compared with Sample (a), no new significant Ag 3d peak shows up for Sample (b) (the laser-sintered composite sample), which implies that a significant amount of Ag-C chemical bonds (if any at all) has unlikely formed during sintering. In particular, the Ag 3d peaks for Sample (b) are not close to the Ag 3d peak at 369.3 eV mentioned by Macková et al. (2008) for Ag-C (Ag bond with an organic structure).

(2) As introduced earlier, the C 1s peaks for Sample (a) can be identified as those for sp² bonded carbon, sp³ bonded carbon and carbonyl carbon. As mentioned earlier there should not be any significant amount of Ag-C chemical bonds in Sample (a), which is an un-sintered mixture of CNTs and silver NPs. The locations of the C 1s peaks for Sample (b) are reasonably close to those for Sample (a) and the same peak identifications can be made. In other words, compared with Sample (a) no new significant C 1s peak shows up for Sample (b) (the laser-sintered composite sample), which provides another piece of supporting evidence that that a significant amount of Ag-C chemical bonds (if any at all) has unlikely formed during sintering. In particular, the locations of the C 1s peaks obtained for Sample (b) are not close to the C 1s peaks reported in literature for typical metal carbides, such as WC and TiC (Galuska et al., 1988; Håkansson et al., 1994).

(3) As introduced in Section 3.2.1, the O 1s peaks for both Sample (a) and (b) can be identified as those for C=O and Ag₂O, which is consistent with (and hence supports the reasonableness of) the identifications of the Ag 3d and for C 1s peaks.

In summary, the analysis above for the XPS results suggests that a significant amount of Ag-C chemical bonds (if any at all) is unlikely to exist in the laser sintered CNT-silver composites (that is, significant Ag-C chemical bond formation at the CNT-silver interfaces has unlikely occurred during the laser sintering process).

3.2.2.2 Interface between the CNT-silver Composite and the Polyimide Substrate

Some related characterization results will be analyzed to improve the understandings of the composite–polyimide substrate interface, such as those related to mechanical interlocking, chemical reactions around the interface and silver diffusion into the polyimide (Kim, 2014).

The characterization results suggest that mechanical interlocking is expected to play an important role in the adhesion at the composite-polyimide interface. The TEM image in Figure 3.7a clearly shows a jigsaw or roughened interface between the composite and the polyimide. The jigsaw structure (i.e., the interface roughness) increases the interfacial contacting area and may help form mechanical interlocking between the sintered composite and the polyimide substrate. Figure 3.9 shows a TEM image with a smaller magnification and hence a broader field of view. It can be seen from the image that for both the portion where the composite remains attached with the polyimide and the portion where they separate during the TEM sample preparation, the composite-polyimide interface appears obviously rougher than the original polyimide film surface observed in the image. This indicates that the interface roughness or jigsaw structure is formed due to the composite fabrication process. As introduced earlier, Figure 3.4b shows an SEM image of the bottom surface of a laser-sintered composite line, which is exposed by peeling off the composite from the polyimide substrate. The bottom surface is partially covered by a thin layer of material coming from the polyimide, which implies that the composite-polyimide adhesion at their interface is strong enough to make an obvious amount of material be taken away from the

polyimide during the peeling process. The morphology shown in Figure 3.4b also suggests a rough composite-polyimide interface and likely mechanical interlocking at the interface.

The XPS results obtained suggests that chemical reactions have likely occurred during laser sintering at around the composite-polyimide interface, which have led the formation of Ag_2O . As shown in Table 2, for both *the top surface* of Sample (a) (an un-sintered mixture of CNTs and silver NPs) and *the top surface* of Sample (b) (laser-sintered CNT-silver composite), silver atoms in the state of Ag_2O make up less than 16 at.% of all silver atoms in the measured region as deduced from the XPS measurement results. However, for the *bottom surface* of Sample (c) (laser-sintered CNT-silver composite), silver atoms in the state of Ag_2O make up a dominant fraction of roughly 86 at.% of all the silver atoms in the measured region. This suggests that chemical reactions (which generate Ag_2O) have likely occurred around the composite-polyimide interface during laser sintering, where silver in the composite and oxygen from the polyimide have reacted and formed Ag_2O . Otherwise, it would be difficult to explain the significant difference in the Ag_2O percentage between the top surface of Sample (b) and the bottom surface of Sample (c). For example, such a big difference is obviously difficult to be explained by the chemical reaction of silver with the ambient environment alone, which would have led to a similar or even larger Ag_2O percentage for the top surface of the composite compared with the bottom surface.

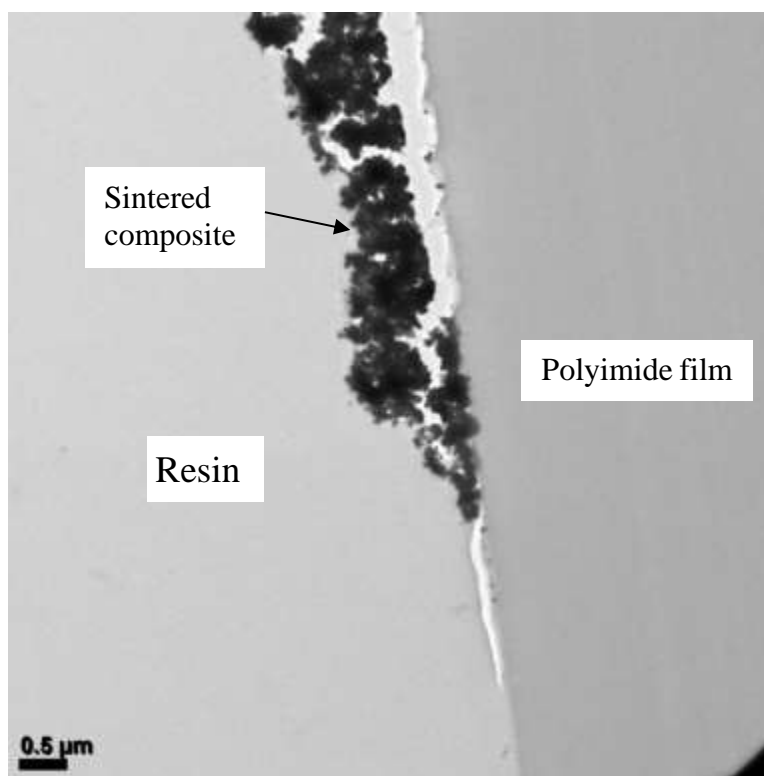


Figure 3.9 TEM image of a cross-section of a laser-sintered CNT-silver composite line on a polyimide substrate

The characterization results do not show significant diffusion of silver into polyimide. If such significant diffusion had occurred, then a smeared composite-polyimide interface could be potentially observed through TEM (Faupel et al., 1998), and sometimes some silver clusters could even go into the inner region of the polyimide and show up as dark spots on a TEM image as reported in (Faupel et al., 1998; Foitzik & Faupel, 1990) for metal diffusion into a polymer. However, these are not clearly observed in the TEM images in Figure 3.7 or Figure 3.9. Instead, the TEM images in Figure 3.7 and Figure 3.9 (the un-separated portion) show that the composite-polyimide interface is relatively sharp; and no dark spots are clearly observable in the inner region of the polyimide film in the TEM images in Figure 3.7 and Figure 3.9. Hence, significant silver diffusion into polyimide has unlikely occurred. In Figure 3.9, in the portion where the composite and the polyimide are separated during the TEM sample preparation process, some small dark

spots can be seen on the polyimide side, which are expected to be residual silver-containing clusters left by the composite layer during the separation process. However, all the silver-containing clusters are located on the surface, and none of them appear to diffuse into the inner region of the polyimide film in the image. The EDS results in Figure 3.7 show that the silver weight percentage drops quickly to almost zero in a relatively thin transition layer near the interface; and it is possible that the thin transition-layer in the EDS results could be due to (or partially due to) interface roughness or variations along the direction normal to the observed cross-section (i.e., roughly along the electron beam propagation direction during the EDS measurements). The EDS results show that silver percentage is zero or close to zero in the inner region of polyimide, which imply that there is no significant diffusion of silver into the inner region of the polyimide substrate.

It is mentioned by Faupel et al. (2005) that the aggregation of metal atoms (such as continuous metal films or large metal clusters) on a polymer surface impedes the metal diffusion into the polymer. In this study, the silver NPs and their coalition during laser sintering make the metal atoms near the polyimide surface mostly in the aggregated state. As a result, their diffusion into the polyimide substrate may be impeded.

The diffusion depth of silver into polyimide, L , can be approximately estimated by Mehrer (2007):

$$L = 2\sqrt{D \tau} \quad (2)$$

where D is the diffusion coefficient and τ is the time duration of the diffusion process. However, the diffusion coefficient of silver in polyimide at temperatures above 500 °C has not been found by the authors. Faupel et al. (2005) reported a value of $\sim 4 \times 10^{-14}$ cm²/s for the diffusion coefficient of ^{110m}Ag in PMDA-ODA polyimide at a temperature around 500 °C. During the laser sintering

process in the current paper, the maximum total laser irradiation duration for an irradiated sample surface point is roughly about 6 ms, which is estimated by the laser spot diameter of $\sim 30 \mu\text{m}$, the spot scanning speed of $\sim 20 \text{ mm/s}$ and the number of times for which each point is scanned (which is 4). If it is assumed that $D = 4 \times 10^{-14} \text{ cm}^2/\text{s}$ and $\tau = 6 \text{ ms}$, then the calculated diffusion depth L is less than $\sim 1 \text{ nm}$. In the actual laser sintering process, the peak sample material temperature could be much higher than $500 \text{ }^\circ\text{C}$ and elevated sample temperatures may be maintained for a duration longer than 6 ms. However, even if an assumption of $D = 1 \times 10^{-10} \text{ cm}^2/\text{s}$ and $\tau = 100 \text{ ms}$ is made, the diffusion depth calculated by Eq.(2) is still only $\sim 63 \text{ nm}$. Although the theoretical estimation of the diffusion depth is very rough, the result is qualitatively consistent with the characterization results from this study in that significant diffusion of silver into polyimide is not observed under the conditions investigated.

3.3 Conclusions

This paper reports experimental studies and structural characterizations for CNT-silver composites produced on polyimide substrates through a laser-based fabrication process. The major purpose of the reported study is to improve the understandings of CNT-metal interfaces in the composites and the composite-polymer interface, which have not been sufficiently studied yet to our best knowledge. In this work, the composite structures are characterized through SEM, EDS, TEM and XPS, and the results have been analyzed. Under the conditions studied and for the samples characterized, it has been found that:

- 1) For the CNT-silver interfaces in the composites, XPS measurement results suggest that a significant amount of Ag-C chemical bonds is unlikely to exist.

2) For the composite-polyimide substrate interface: (i) Based on the TEM and SEM observations, it is expected that “mechanical interlocking” should play an important role in the composite-polyimide adhesion. (ii) The characterizations conducted do not show a significant silver diffusion into the polyimide substrate. The TEM images show a relatively sharp composite-polyimide interface and no silver clusters in the inner region of the polyimide. The result is qualitatively consistent with a rough theoretical estimation of silver diffusion depth into polyimide. (iii) The XPS results suggest that chemical reactions have likely occurred at around the composite-polyimide interface, where silver and oxygen coming from the polyimide react and form Ag_2O .

4. STATIC TENSILE TESTS AND ADHESION TESTS OF LAESR SINTERED CNT-SILVER COMPOSITE ON FLEXIBEL SUBSTRATE

In Chapter 2, laser sintered CNT-metal composite lines were fabricated on polyimide and bending fatigue was evaluated by cyclic bending tests. However, further mechanical performance evaluation is still needed. Previous research in literature (D. Zhao et al., 2012; Hwang et al., 2015; Z. Kang et al, 2018a; Ji et al., 2017) produced CNT-metal composite on flexible substrate, but the samples were not characterized with mechanical tests or characterized with only bending tests. In this chapter, static tensile tests and adhesion tests are employed to further evaluate the performance of laser sintered CNT-silver composite films and laser-sintered silver films on polyimide substrates. During static tensile tests, the tested samples are stretched at very low strain rate and real-time electrical resistance is recorded every 1% increment of strain, until 15% of strain or until the sample fails. During adhesion tests, an area of sintered materials, instead of lines, are stretched until the adhesion interface fails (Maekawa et al., 2009). All tested samples are stretched at very low strain rate and the applied tension is measured using a load cell. In both tests, results from laser-sintered CNT-silver composite films and from laser-sintered silver films are compared and the impact of addition of CNTs is evaluated.

4.1 Experiment Setup

The samples used in static tensile tests are prepared following the same procedures as introduced in Chapter 3. After laser sintering and washing with organic solvent, both ends of the sample line are covered with silver paint (Ted Pella, Inc) and left in air to dry for at least 12 hr. The samples used for adhesion tests are prepared slightly differently: during ink deposition, the distance between adjacent paths are adjusted to form a continuous area of material; during laser

sintering, an overlapping ratio of 67% is used to produce a continuous sintered film for test. Other than these, all processing parameters used in suspension preparation, suspension deposition and laser sintering are the same as introduced in Chapter 3, except that laser power used may be either ~0.35 or ~0.4 W as labeled in the results in this chapter. The top surface of the sintered area is then bonded to another piece of PI film with strong glue (Loctite Super Glue Ultra Gel), which has a nominal shear strength about 15 - 25 MPa (Loctite, 2014). The strong glue is fully cured before the experiments are executed. For the samples used in the adhesion tests, the glued area between the sintered area and PI is about 8~13 mm².

Static tensile test is employed to study the capability of the sintered lines to resist tensile strain. The setup is shown in Figure 4.1. The PI film is stretched manually using a micrometer linear stage at a low average speed (less than 3 $\mu\text{m/s}$) to increase the applied strain on the sintered lines. Strain applied on the samples ranges from 0 to 15% or until failure (criteria of failure is given later). At every 1% increment of strain, resistance of the sintered lines is recorded. The resistance is measured in-situ using two-point probe method with Keysight digital multimeter 34461A. To eliminate the impact of contact resistance and wire resistance, etc., during the experiment, performance of the samples is compared by means of normalized resistance change, which can be calculated by:

$$\delta = \frac{R(\epsilon) - R(0)}{R_0}$$

where R_0 is resistance of the sintered line measured with four-point probe method, $R(0)$ is in-situ resistance before tests begin which includes R_0 , contact resistance, silver paint resistance and copper wire resistance, ϵ is applied strain, and $R(\epsilon)$ is in-situ resistance after strain is applied. The equation above is based on the approximate assumption that all resistance change during a tensile

test comes from the resistance change in the laser-sintered film due to the tensile strain. Normalized resistance change is essentially extent of resistance change during static tensile tests.

In-situ observations through optical microscope is used during some static tensile tests to track crack initiation and development within the areas in view. In-situ observation is necessary because the tested samples may change after unloading. Ex-situ images are taken with a scanning electron microscope (SEM) (FEI NOVA nanoSEM Field Emission SEM) to explore the structure of cracks after the tensile tests.

Adhesion tests have been employed to explore the adhesion shear strength of bonding at the interface between sintered material and PI film. Figure 4.2 shows the schematic setup of the adhesion test. Both ends of PI films are manually applied on with an increasing tensile force F (by means of elongation at an average rate of less than $3 \mu\text{m/s}$), which is measured with an Interface SM-200N load cell and an SGA signal conditioner, and the results are displayed and recorded with a Lecroy LC534AL oscilloscope at small force steps (less than 0.15N applied per step when close to failure). The shear force F is applied on both ends of the sample until the adhesion fails and the sintered area separates from the PI substrate underneath. The shear strength is then calculated as $\tau = F/A$, where A is the contact area. However, it is noteworthy that the load is not recorded at the instant when the contact fails because the force data is not recorded in-situ (only displayed in-situ). The last recorded force data before failure is used for adhesion strength calculation. As a result, the adhesion strength is overall slightly underestimated.

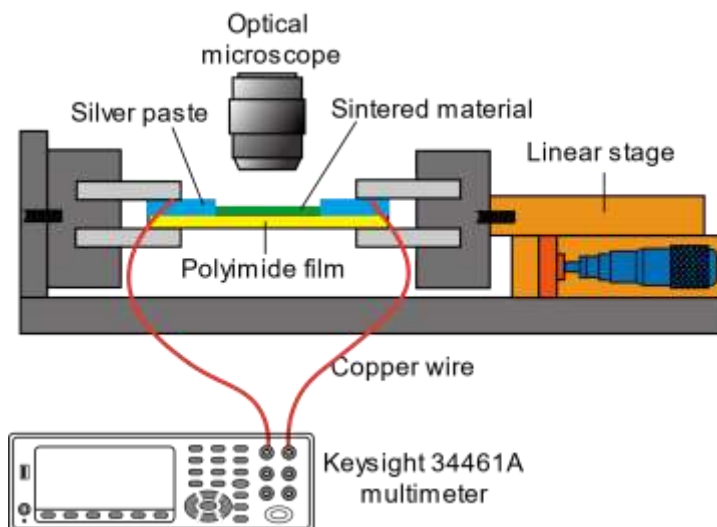


Figure 4.1 Schematic setup of static tensile tests

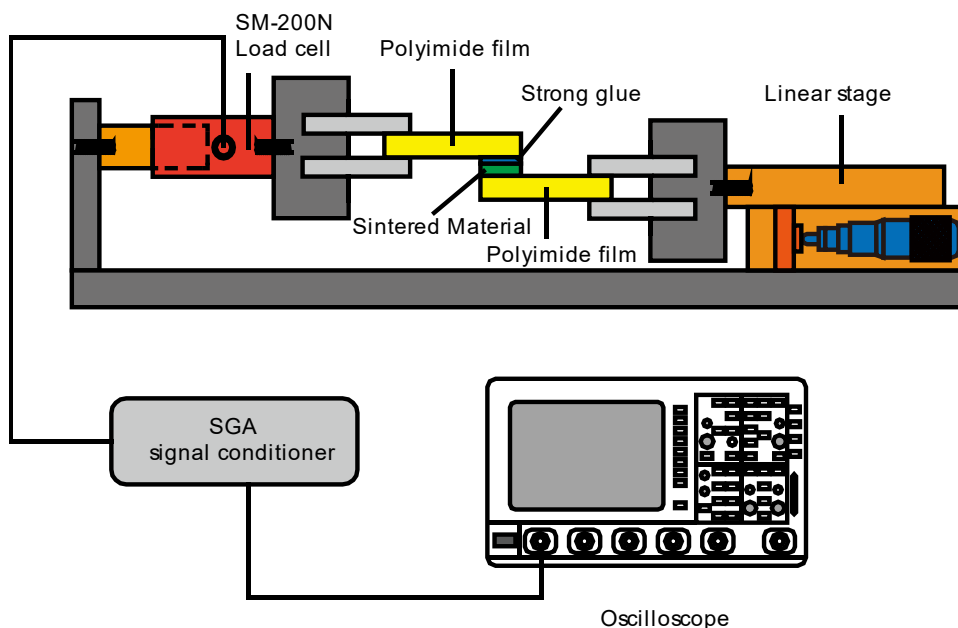


Figure 4.2 Schematic setup of adhesion test.

4.2 Results and Discussion

4.2.1 Static Tensile Test

During static tensile tests, three groups of samples are compared: a) Ag samples sintered at laser power of $\sim 0.35\text{W}$, b) Ag samples sintered at laser power of $\sim 0.40\text{W}$, c) CNT-silver

composite samples sintered at laser power of $\sim 0.35\text{W}$. The average thickness of the three groups of samples in static tensile tests are $\sim 1.58\ \mu\text{m}$, $\sim 1.57\ \mu\text{m}$ and $\sim 1.68\ \mu\text{m}$ respectively. Resistance of the samples is tracked in-situ every 1% of strain from 0 to 15% strain or until sample fails. When the normalized resistance change is over 10, the line is considered failed.

The results of static tensile tests are shown in Figure 4.3. Ag lines sintered at laser power of $\sim 0.35\text{W}$ fail soon after test begins, before a tensile strain of 3%. Ag lines sintered at laser power of $\sim 0.4\text{W}$ all failed before a tensile strain of 7%. However, all of the nine CNT-silver lines sintered at laser power of $\sim 0.35\text{W}$ survive after 15% tensile strain except one. The final resistance of the surviving CNT-silver lines at the tensile strain of 15% is about 6-8 times more than their initial resistance.

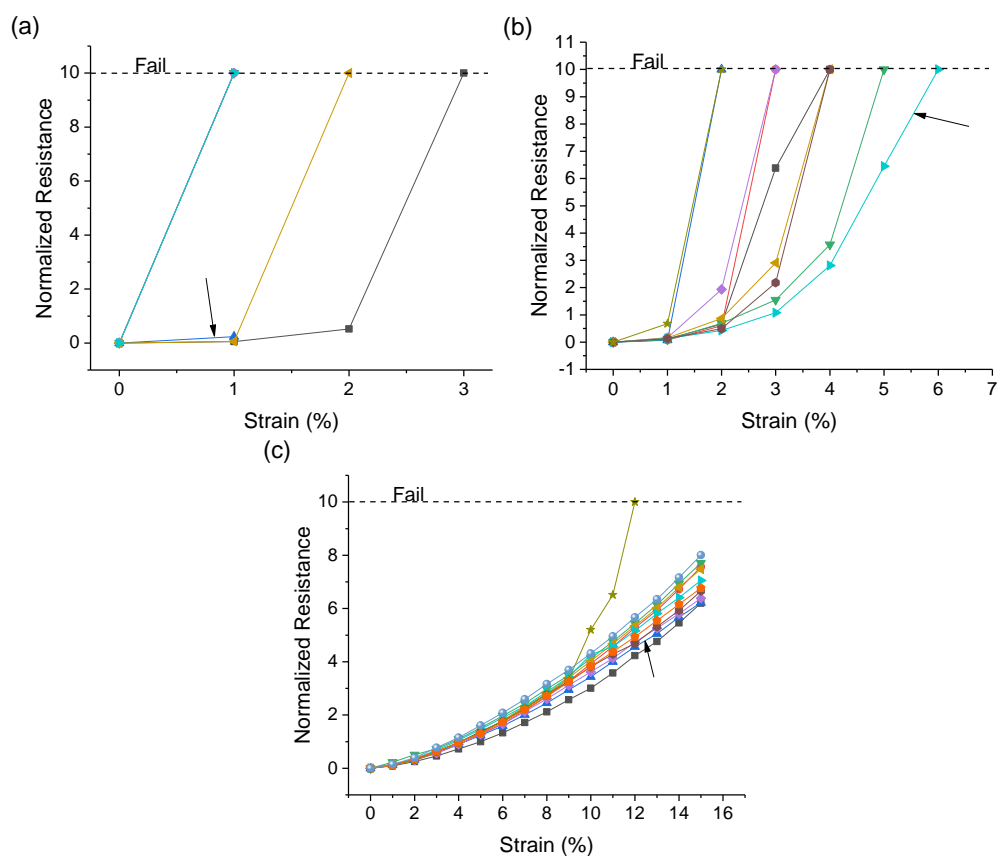


Figure 4.3 Normalized resistance change curve during static tensile tests. (a) Ag sintered with $\sim 0.35\text{W}$ laser. (b) Ag sintered with $\sim 0.4\text{W}$ laser. (c) CNT-silver sintered with $\sim 0.35\text{W}$ laser.

During some of the experiments, optical microscope images of tested CNT-silver lines and Ag lines are recorded every 1% increase of tensile strain, to track the initiation and development of cracks on the top surface of sintered lines. Images of typical samples during the static tensile tests are displayed in Figure 4.4. Samples displayed in Figure 4.4 are those marked with arrows in the test results shown in Figure 4.3. Ag lines sintered at laser power of $\sim 0.35\text{W}$ fail soon after tests begin, with only one or two through cracks in the entire line where the cracks propagate very fast across the width of the lines and the lines break. Ag lines sintered at laser power of $\sim 0.40\text{W}$ can resist more cracks and larger strain before failure. Small cracks start to become visible around the strain of 4% at multiple locations from the edge and propagate roughly in the width direction. Some cracks develop faster across the width and all tested lines break before 7% tensile strain. Cracks start to be visible at a higher strain in CNT-silver lines sintered at laser power of $\sim 0.35\text{W}$. Propagation of cracks is slower and more consistent along the length. At the end of 15% tensile strain, the lines are still not broken although large number of cracks exist. Comparing CNT-silver lines at strain of 15% with the failed silver samples at strain 6% sintered at $\sim 0.4\text{W}$, it is interesting to notice that: a) CNT-silver lines generally develop a similar number of cracks or more cracks than Ag lines, but the cracks are shorter; b) Many of these cracks in CNT-silver lines have wider openings on the edge than cracks on Ag lines. These observations support that CNT-silver lines can resist more cracks and wider cracks without failing. Ex-situ SEM images of samples after static tensile tests are displayed in Figure 4.5. Ag line sintered at $\sim 0.4\text{W}$ shows separation at location of cracks while in CNT-silver lines sintered at $\sim 0.35\text{W}$, two sides of a crack are still connected with CNTs in the middle of the extending crack.

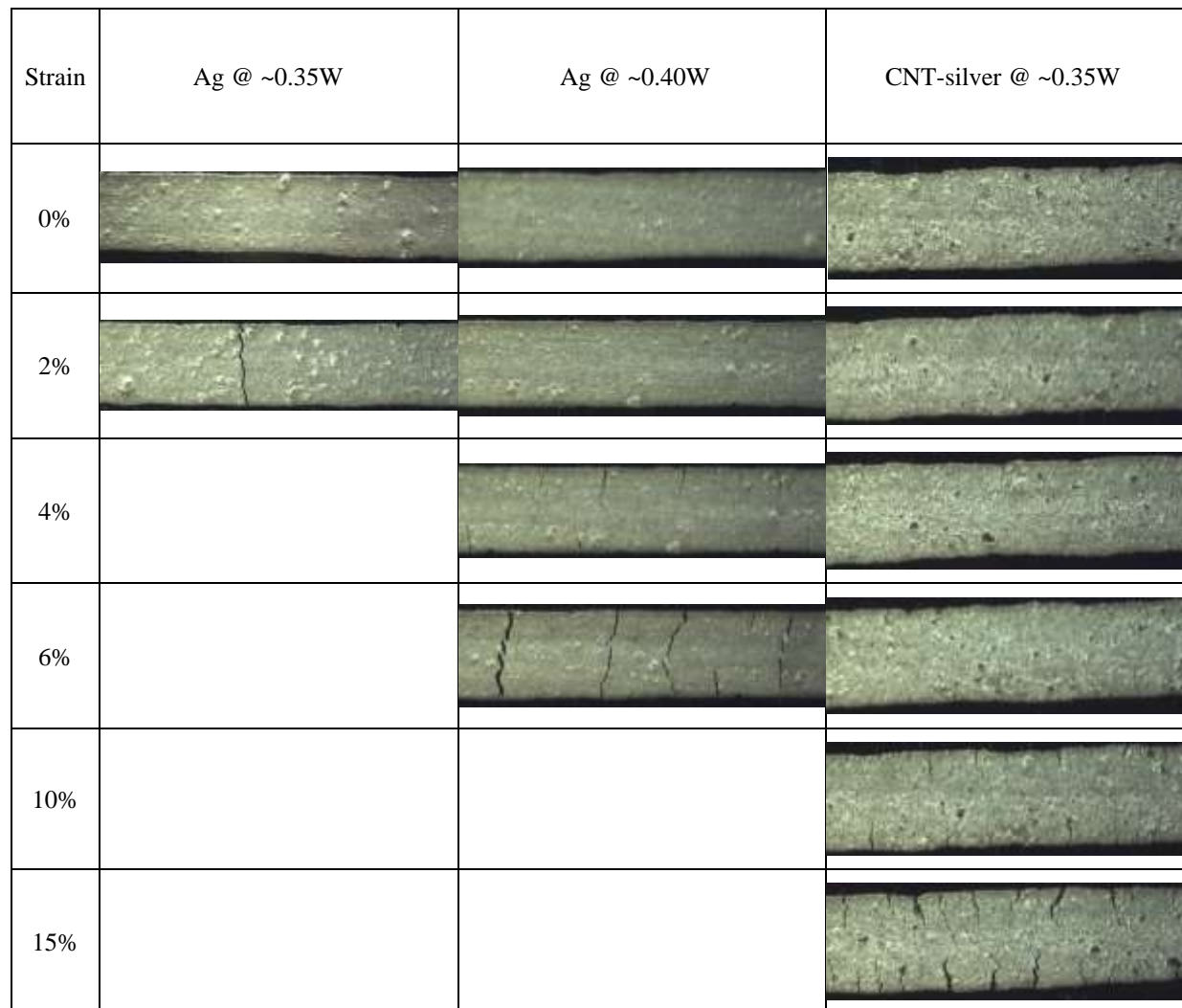


Figure 4.4 Optical microscope images of sintered lines during static tensile tests at different strains. The images under different strains may be captured at different locations.

The major difference in performance during static tensile tests is attributed to addition of CNTs and it shows great potential advantage of CNT-silver composite. First, the optical microscope images in Figure 4.4 show that crack development slows down substantially when CNTs exist. Comparing the crack distribution of Ag lines sintered at ~0.35W and ~0.40W under 2% strain, several minor cracks have initiated on the edge in the observed area of Ag line sintered at ~0.40W, but the Ag line sintered at ~0.35W has already failed with only one observed crack in view. Although the CNT-silver line is sintered at ~0.35W, it is expected that the CNTs inside the

composite may help connect and hold together sintered silver. Consequently, crack generation is inhibited. For the same reason, it is expected that crack propagation may have to overcome stronger resistance than in Ag lines because the two sides of an existing crack may still be connected by CNTs, as shown Figure 4.5. Due to the crack inhibition effect, cracks in CNT-silver lines are clearly visible at a higher strain. Second, good electrical properties of CNTs can potentially help reduce normalized resistance change during the static tensile tests by connecting two sides of a crack, providing additional conductive channels, as shown in Figure 4.5.

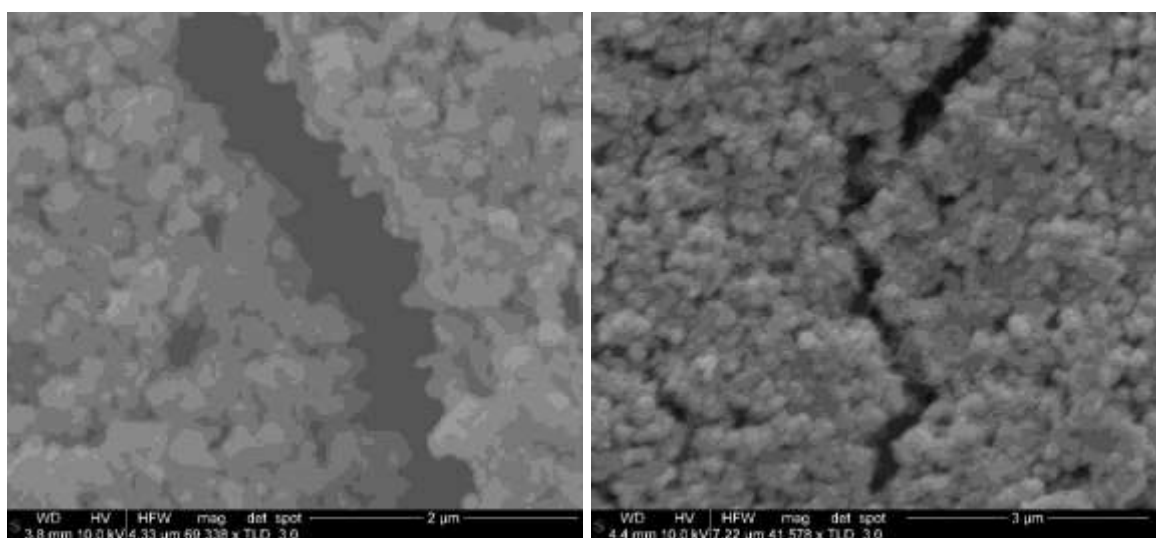


Figure 4.5 SEM images of Ag @~0.4W laser(left) and CNT-silver @~0.35W laser(right) samples after static tensile tests.

4.2.2 Adhesion Test

The adhesion shear strength at the interface between sintered materials and PI film at different laser powers has been investigated by adhesion tests. A schematic setup of adhesion test is given in Figure 4.2. An area of deposited material is sintered by means of sintering overlapping lines. The overlapping ratio between adjacent lines is about ~67%. Three groups of samples are used for adhesion tests: a) Ag film samples sintered at a laser power of ~0.35W; b) Ag film samples

sintered at a laser power of $\sim 0.40\text{W}$; c) CNT-silver composite samples sintered at a laser power of $\sim 0.35\text{W}$.

Results of shear strength are shown in Figure 4.6. Average shear strength of Ag samples increased from $\sim 4.4\text{MPa}$ to $\sim 5.9\text{MPa}$ as the laser power is raised from $\sim 0.35\text{W}$ to $\sim 0.40\text{W}$. The CNT-silver samples, although sintered at a lower laser power of $\sim 0.35\text{W}$, achieve average shear strength of $\sim 6.5\text{MPa}$, which is similar to Ag samples sintered at $\sim 0.40\text{W}$. These results are comparable to those obtained from Ag films sintered on polyimide reported by Maekawa et al. (2009).

The shear strength is expected to be mainly determined by adhesion at the interface. As discussed in Chapter 3, mechanical interlocking is expected to play an important role in the adhesion mechanism. CNTs extending inside the composite may help hold together sintered silver. This may further improve shear strength of the composite in areas away from the interface. With the stronger CNT-silver composite, mechanical interlocking can also be potentially improved at the interface.

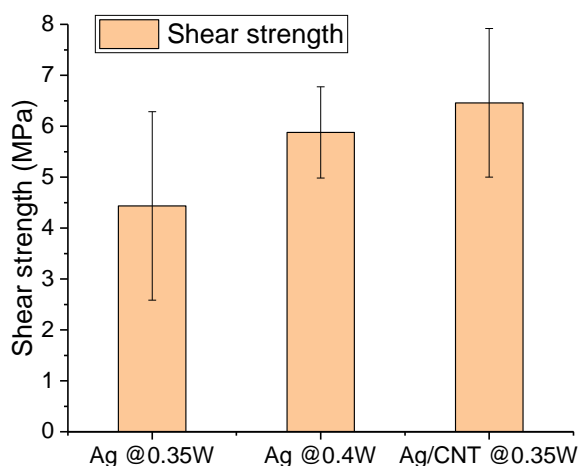


Figure 4.6 Shear strength of laser sintered materials on PI film under different conditions.

4.3 Conclusions

In this chapter, static tensile tests and adhesion tests are carried out to study Ag films and CNT-silver composite films sintered on flexible PI substrate. Under the conditions investigated and for the samples tested, the following conclusions may be drawn from the test results and analysis:

- 1) Ag lines sintered at the laser power of $\sim 0.35\text{W}$ and $\sim 0.40\text{W}$ all failed before the tensile strain of 7% of while only one of the nine CNT-silver lines sintered at laser power $\sim 0.35\text{W}$ failed before the strain of 15%. In adhesion tests, CNT-silver samples sintered at $\sim 0.35\text{W}$ also show better performance than Ag samples sintered at $\sim 0.35\text{W}$ and comparable performance to Ag samples sintered at $\sim 0.40\text{W}$.
- 2) Addition of CNTs can improve material performance during the static tensile tests and adhesion tests. Excellent mechanical properties of CNT may help bond sintered silver and inhibit the initiation and growth of cracks. CNTs can also potentially provide additional electrically conductive channels in cracks, slowing down increase of resistance change in static tensile tests.

5. COALESCENCE OF GOLD NANOPARTICLES AROUND THE END OF A CARBON NANOTUBE: A MOLECULAR-DYNAMICS STUDY

The main content of this chapter has been published in the journal article: Zheng Kang and Benxin Wu, Coalescence of gold nanoparticles around the end of a carbon nanotube: A molecular-dynamics study. Journal of Manufacturing Processes, 2018, 34, 785–792. Copyright © Elsevier, 2018

The advantages of Molecular Dynamics (MD) simulation have been introduced in Chapter 1. In this chapter, MD simulations have been conducted to study and help understand the coalescence of gold nanoparticles (Au NPs) initially placed around the end of a multi-walled carbon nanotube (MWCNT), and the interactions among the NPs and the CNT, under elevated temperatures that can be potentially induced by pulsed-laser heating. First, the MD modeling approach is tested (at least partially) by comparing model-predicted melting points of NPs with experiment-deduced results from the literature. Then the model is expanded and adjusted to study and help understand the interactions among multiple Au NPs and a multi-walled carbon nanotube (MWCNT); and model calculations have been performed under different elevated temperatures and for different nanotube diameters. Adaptive common neighbour analysis (CNA), radial distribution function (RDF) and mean squared displacement (MSD) have been employed to help obtain a good understanding of the coalescence and interaction processes. The main content in this chapter has been published in research article (Kang and Wu, 2018b)

5.1 Model Setup

Figure 5.1 shows the overall initial configuration and geometrical setup of the MD model to investigate the coalescence and interactions of five Au NPs initially positioned around one end of a MWCNT (which is a double-walled nanotube in this work). Such a setup has been used in the

simulated cases (when a CNT exists) shown later in Figures 5.3-5.9. Initially, the center-to-center distance between adjacent Au NPs is 3.4 nm, while the distance between the center of the central Au NP and the end of the MWCNT is 1.9 nm. In this study, the initial diameter of each Au NP is set as 3 nm, while the MWCNT has an armchair structure and could have different diameters in different simulated cases (see Table 5.1 for some of the CNT parameters). The initial length of the MWCNT is set as 8 nm for all the simulated cases with a CNT. The non-periodic shrink-wrapped boundary condition (Theodorakos et al., 2015) is applied in all directions, which sets the faces of the MD simulation domain box in a way to include all the atoms inside the box.

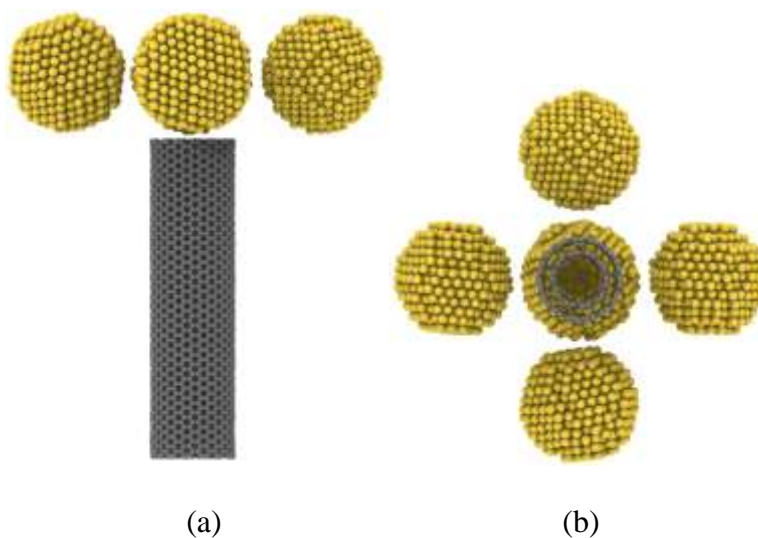


Figure 5.1 Initial configuration and geometrical setup of the MD model: (a) side view, and (b) view from the bottom end of the MWCNT (Yellow atoms represent Au atoms, while black atoms represent carbon atoms. Four Au NPs surround the central Au particle with a center-to-center distance of 3.4 nm; and the center of the latter is 1.9 nm away from the end of the CNT whose diameter in different cases is listed in Table 5.1)

First, the whole system (including the CNT and the NPs) is equilibrated for 500 ps at the temperature of 300K. The moment at the end of the equilibration stage is set as time $t = 0$ ps. Then the whole system is heated to around a certain targeted heating temperature in 100 ps, and is maintained in the constant-energy ensemble (NVE) for another 500 ps. The heating stage period

is set at 100 ps to mimic the heating effect that can be potentially induced by a laser pulse with a duration on the order of ~ 100 -picosecond (ps). Different targeted temperatures will be studied, which can be potentially achieved with laser pulses at different fluences in practice. It is assumed that the whole system is in vacuum and the gravity force has been neglected. The possible heat dissipation into the ambient vacuum environment is not considered in the MD simulations. During the equilibration and heating stages, the system is kept in the NVT ensemble where the Nose-Hoover thermostat (Hoover, 2012) has been applied to control the temperature. Then the NVE ensemble is used during the subsequent 500-ps period. Throughout each simulation, the motion of each carbon atom in the CNT has been constrained in a region near its initial location to avoid the possible CNT drifting or rotation; and under such conditions the interactions among the Au NPs and the MWCNT will be studied in this work through MD simulations.

In this work, the well-known embedded-atom-method (EAM) potential (Foiles, Baskes, & Daw, 1986) has been employed for the Au-Au interaction, while the C-C interaction is described using the adaptive intermolecular reactive empirical bond-order (AIREBO) potential (Stuart, Tutein, & Harrison, 2000), and the Au-C interaction is described using the Lennard-Jones (LJ) potential with parameters taken from (Neek-Amal, Asgari, & Rahimi Tabar, 2009), where the primary energy well depth $\varepsilon = 0.0341$ eV and the collision diameter $\sigma = 3.003$ Å. The Molecular Dynamics (MD) simulations are carried out based on the open source code called “Large-scale Atomic/Molecular Massively Parallel Simulator” (LAMMPS) (Plimpton, 1995). The equation of motion for the involved atoms is numerically integrated with the Verlet algorithm (Allen & Tildesley, 1989; Plimpton, 1995) using a time step of 2 fs. In each simulation, the CNT is generated in VMD (Humphrey, Dalke, & Schulten, 1996). Visualization of the simulation results has been processed with OVITO (Stukowski, 2009).

5.2 Results and Discussions

5.2.1 MD Model Comparison with Experiment-Deduced Results

First, the MD-predicted melting points of Au NPs at different sizes will be compared with experiment-deduced results shown in (Buffat & Borel, 1976) to test (at least partially) the modeling approach employed in this study. A separate MD model is set up, which only involves one or more Au NPs of certain sizes without a CNT. The center of mass of each NP is assumed to be fixed during the MD calculations. It should be noted that for very small Au NPs, e.g., diameters of 3 nm or 4 nm, the MD model setup consists of multiple non-interacting NPs (which are positioned relatively far away from each other) to reduce the fluctuation of results. For larger NPs, in each simulation the MD model setup only consists of one NP. During each MD simulation, after a 1-ns equilibration stage at 300 K, the Au NPs are then heated from the temperature of 300K to 1400K with a step of 100K. At each step, after the heating is finished, the system is maintained at the targeted temperature in the NVT ensemble for a period of 500 ps; and the average potential energy per atom (PE/atom) time-average for the last 300 ps of the period is calculated and recorded. Similar steps have been employed for a cooling process following a reverse temperature order. During each simulation, the temperature step is changed to a smaller value of 20K when the temperature is around the melting or freezing point of the gold nanoparticles. Similar to Section 2, the shrink-wrapped boundary condition and the Nose-Hoover thermostat have been used in the simulations.

Table 5.1 MWCNT parameters used in the MD simulations of this work

| | Case 1 | | Case 2 | | Case 3 | |
|-----------|-----------|---------------|-----------|---------------|-----------|---------------|
| | Chirality | Diameter (nm) | Chirality | Diameter (nm) | Chirality | Diameter (nm) |
| Inner CNT | (5,5) | 0.68 | (10,10) | 1.36 | (15,15) | 2.04 |
| Outer CNT | (10,10) | 1.36 | (15,15) | 2.04 | (20,20) | 2.71 |

Figure 5.2a shows the melting points of gold nanoparticles versus the particle diameters. It can be seen that the model-predicted melting points agree with the experiment-deduced results taken from (Buffat & Borel, 1976) reasonably well, although some differences do exist. The results in the figure show that the melting point drops as the particle size decreases, and this phenomenon is the melting point depression that depends on particle sizes (Sambles, 1971). During the MD simulations, the melting points of the nanoparticles are determined based on the jumps in the PE/atom-versus-temperature curves for the particles (J. Cui et al., 2014; Goudeli & Pratsinis, 2016). For example, typical PE/atom curves for the heating and cooling processes for 3-nm Au NPs are shown in Figure 5.2b, which are plotted based on MD simulation results. When the NPs are heated from a starting temperature of 300K, the PE/atom value increases approximately linearly with the temperature until the temperature is close to the melting point, where a jump of the PE/atom value occurs. After the jump, the PE/atom continues increasing approximately linearly with the temperature. The temperature right after the jump is assumed to be the melting point of the NPs in the MD simulation, because this is where the full melting of the NPs have occurred. During the cooling process, the freezing point of the NPs can be determined from the sudden drop in the PE/atom-versus-temperature curve through a similar approach. As shown in the curves in Figure

5.2b, the melting and freezing points are different from each other even for the same Au NPs; and they are also different from the bulk gold melting point of 1337K (Goudeli & Pratsinis, 2016). In Figure 5.2c, the curves of PE/atom versus temperature during the heating process for gold nanoparticles with different sizes have been plotted. As the gold particle size increases, the PE/atom curve shifts to the right, which means the melting point increases with the particle size under the conditions studied.

5.2.2 MD Study of NP Coalescence and NP-CNT Interaction Near the End of the CNT

After the model comparison with experiment-deduced results introduced in Section 5.2.1, next the MD model, in the setup shown in Figure 5.1, will be applied to simulate the coalescence of Au NPs and their interactions with a MWCNT around the end of the MWCNT. The major details of the model have been introduced earlier in Section 5.1. Simulations have been performed for armchair MWCNTs with different tube diameters (as listed in Table 5.1) and for targeted heating temperatures that are below, around and above the melting point of 3-nm gold nanoparticles shown in Figure 5.2a. It should be noted that system temperatures may change under an NVE ensemble; and in this work when a MD-simulated case is labeled by a temperature, that temperature typically refers to the targeted temperature in the simulated case right at the end of the heating stage.

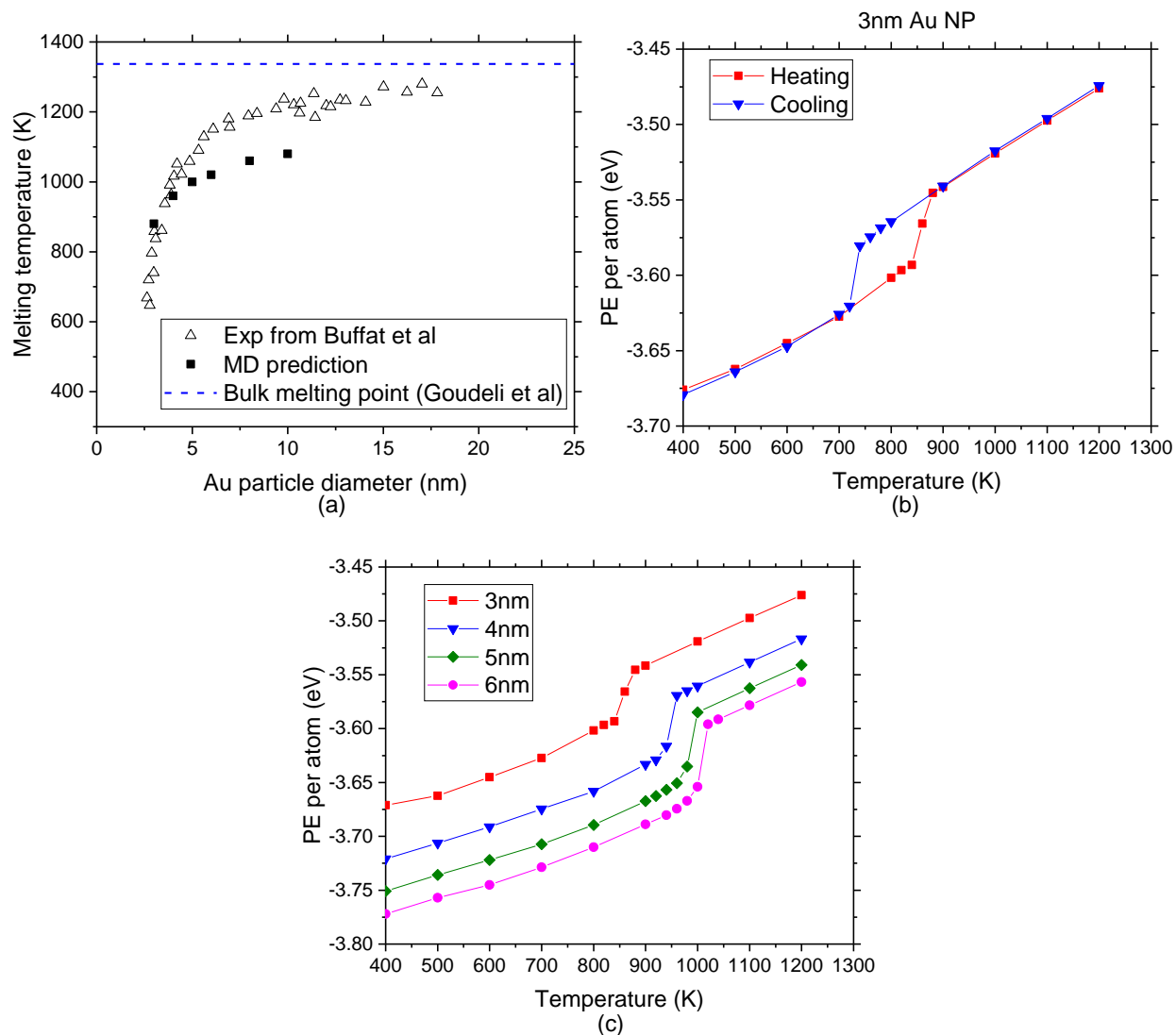


Figure 5.2 (a) Melting points of Au NPs at different sizes predicted by MD simulations in this work, in comparison with experiment-deduced melting points digitized from a figure in Ref. (Buffat & Borel, 1976). (b): MD-predicted PE per atom versus temperature for 3-nm Au NPs during heating and cooling processes. (c) MD-predicted PE per atom versus temperature for Au NPs of different sizes during a heating process.

5.2.2.1 Effect of CNT diameter on coalescence and interactions under the targeted temperature of ~600 K

The first column of Figure 5.3 shows the results for the situation without a CNT. From $t = 0$ ps to 100 ps (which is the 100-ps heating stage), the fcc structure in the gold nanoparticles have been changed during the merging of the particles. Most atoms have become disordered,

particularly at grain boundaries between adjacent Au NPs. After the 100-ps heating stage ends, in the subsequent 500-ps period (during which the system is maintained in the NVE ensemble), more atoms are identified as structured in the simulated system.

The second to the fourth columns of Figure 5.3 show the simulations with a CNT of different diameters. The two stages of structural evolutions, as described in the previous paragraph, can still be seen for these situations. However, some different morphology evolutions are very obvious when a MWCNT is present. At $t = 100$ ps, when the heating process has just finished, the Au NPs on the first column of Figure 5.3 have merged with each other, but the necks between adjacent particles are still visible in the image. However, for systems with a MWCNT, overall the neck becomes less visible in the image as the CNT diameter increases. For the situation with a (15,15)-(20,20) MWCNT (the fourth column), no neck can be observed at $t = 100$ ps in the image. At $t = 600$ ps, which is 500 ps after the end of the heating stage, no neck is visible for all the four simulated systems shown in the figure. The merged Au nanocluster appears more spherical in the image for the situation with a CNT of a larger diameter. Another interesting phenomenon revealed from the MD simulations is the entrance of gold atoms into the MWCNT. For the situation with the 0.68-nm-diameter MWCNT, the simulation results on the second column in Figure 5.3 show that only two gold atoms have entered the nanotube in the simulated case; and after entering the tube, the two atoms move back and forth between two ends of the tube without running out of the tube from the other tube end or merging back to the gold cluster during the simulated period. More gold atoms enter the MWCNT as the tube diameter increases, which can be seen in the cases with the 1.36-nm-diameter and 2.04-nm-diameter CNTs. In these two cases, after the migration of some gold atoms into the nanotube for a certain amount of time, the length of gold cluster inside the tube becomes relatively stable during the simulated period. Previous experimental studies in the

literature (e.g., (Govindaraj, Satishkumar, Nath, & Rao, 2000; Sloan et al., 1999)) reported the filling of CNTs by molten materials. In Ref. (Sloan et al., 1999), the maximum temperature during the filling process is higher than the filling material's melting or liquidus temperature. Ref (Dujardin, Ebbesen, Krishnan, & Treacy, 1998) reported experimental studies on the wetting of single-shell CNTs by several molten materials. (J. Cui et al., 2014; Schebarchov & Hendy, 2008) observed a capillary effect in the performed MD simulations that involved single-walled CNT(s) and a single metal NP, where the metal NP reached a molten state in the simulations. However, it should be noted that in the simulations for Figure 5.3, the system temperature at the end of the heating stage is $T = 600$ K, which is below the melting point of gold NPs shown in Figure 5.2a. This suggests that the capillary effect of a MWCNT with a sufficiently large diameter may draw some atoms of metal NPs into the tube at temperatures below the NPs' melting point. This is a very interesting phenomenon revealed by this study, which has been rarely reported in the literature to our best knowledge. Further studies may still be needed to confirm and fully understand this.

Figure 5.4 shows MSD evolutions for gold NPs in different simulated cases, where the MSD is defined as (Pan et al., 2008):

$$\text{MSD} = \frac{1}{N} \sum_{i=1}^N [r_i(t) - r_i(0)]^2$$

where N denotes the quantity of sampled atoms, $r_i(t)$ represents the location of atom i at the time t , and $r_i(0)$ denotes the location of the atom at $t = 0$. In this work, typically all the Au atoms in the system are used in the MSD calculations.

The MSD curves can help provide an insight into the diffusion process of the gold nanoclusters for the studied cases. It should be noted that because MSD is defined based on displacements of atoms, the entrance of gold atoms into the CNT will influence its absolute values.

The MSD curves can be approximately divided into two stages. The first stage corresponds to the fast diffusion of gold NPs that occurs in each simulated system during roughly the first ~120 ps, and the stage ends soon after the completion of the heating process. Although the duration of the fast diffusion stage is similar for different simulated systems in Fig. 4, the overall diffusion rate increases as the diameter of the MWCNT in the system increases. In the second stage of each MSD curve, the MSD becomes relatively stable and no longer has a fast change. In the second stage, Au atoms in the nanocluster become more structured than those at $t = 100$ ps (the end of the heating stage), which can be seen from the colors of atoms given in Figure 5.3 based on adaptive CNA and from the RDF curves given in Figure 5.5.

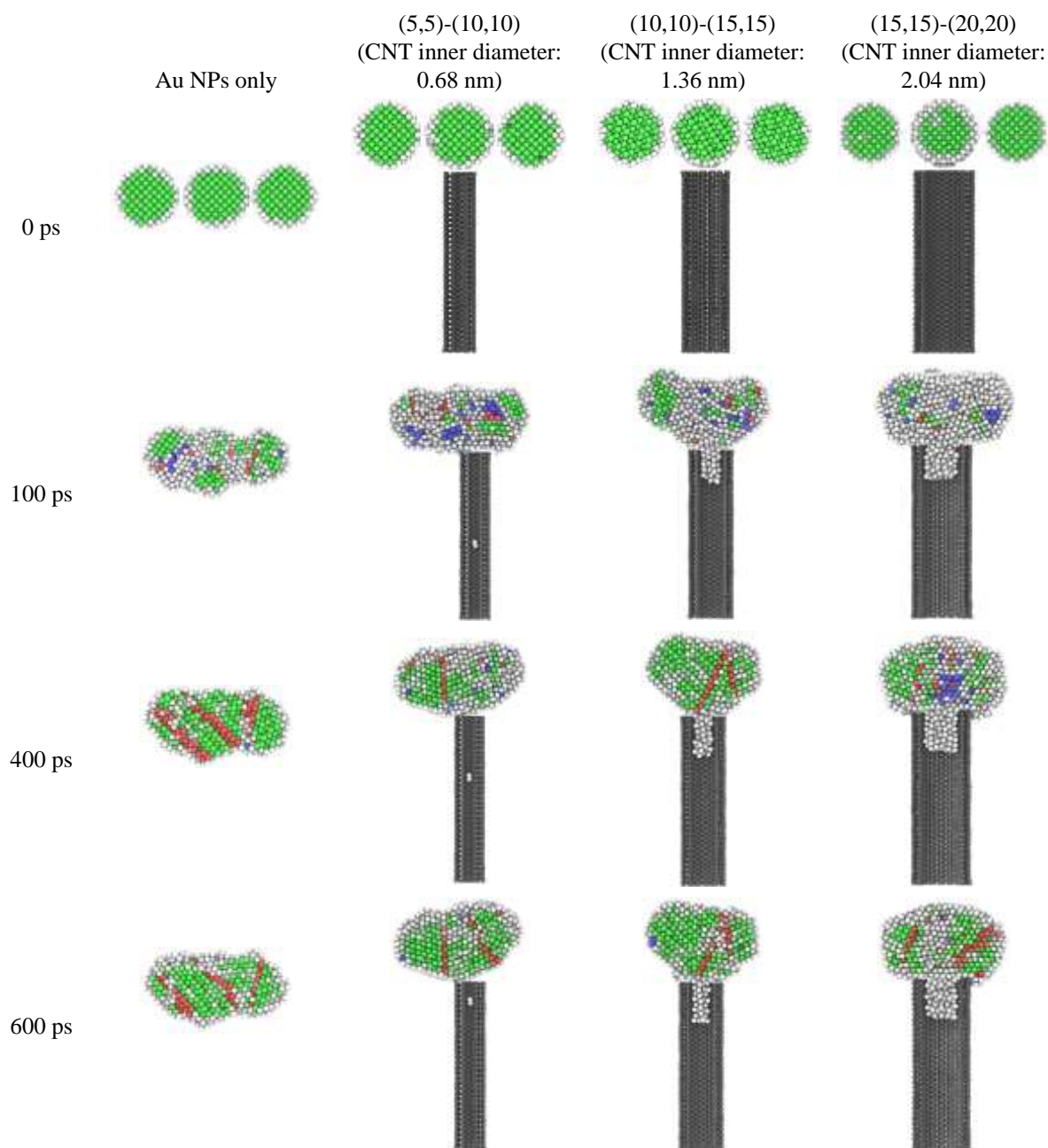


Figure 5.3 MD-predicted system evolution where the system temperature is 600 K at the end of the 100-ps heating stage. Column 1: system that only consist of Au NPs; Column 2, 3 and 4: system with Au NPs initially near the end of a MWCNT with different diameters (The heating stage starts at $t=0$ ps and ends at $t=100$ ps, after which the system is maintained in the NVE ensemble during the simulation. Images shown are for cross-sections of NPs and/or CNTs. Carbon atoms are plotted in black. Gold atoms are plotted in colors denoting their local atomic structures identified through the adaptive CNA approach (Stukowski, 2012). The green, blue and red colors correspond to fcc (face-centered cubic), bcc (body-centered cubic), and hcp (hexagonal close packed) structures respectively while the white color is used to plot atoms with unidentified structures (such as surface atoms or disordered atoms)).

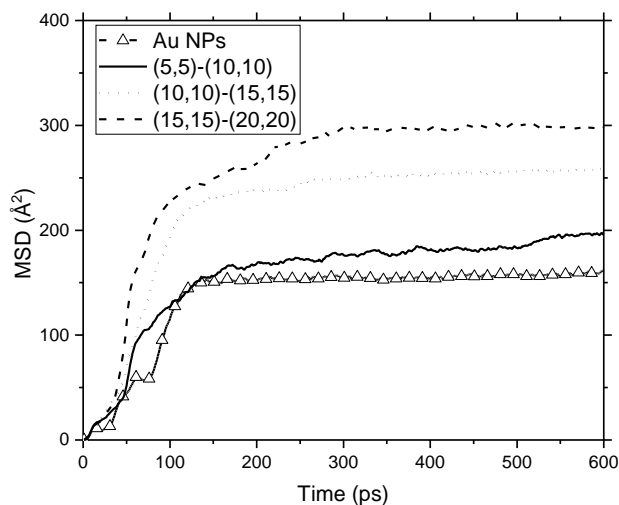


Figure 5.4 Mean squared displacement (MSD) of gold (Au) atoms for the different simulated systems shown in Figure 5.3.

The MSD curves can help provide an insight into the diffusion process of the gold nanoclusters for the studied cases. It should be noted that because MSD is defined based on displacements of atoms, the entrance of gold atoms into the CNT will influence its absolute values. The MSD curves can be approximately divided into two stages. The first stage corresponds to the fast diffusion of gold NPs that occurs in each simulated system during roughly the first ~120 ps, and the stage ends soon after the completion of the heating process. Although the duration of the fast diffusion stage is similar for different simulated systems in Figure 5.4, the overall diffusion rate increases as the diameter of the MWCNT in the system increases. In the second stage of each MSD curve, the MSD becomes relatively stable and no longer has a fast change. In the second stage, Au atoms in the nanocluster become more structured than those at $t = 100$ ps (the end of the heating stage), which can be seen from the colors of atoms given in Figure 5.3 based on adaptive CNA and from the RDF curves given in Figure 5.5.

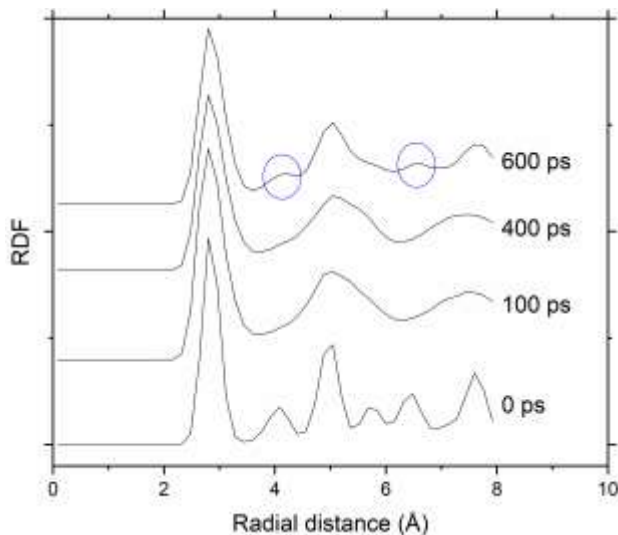


Figure 5.5 Radial distribution function (RDF) evolution of gold atoms for the simulated system in Figure 5.3 with the 2.04-nm inner diameter CNT.

Radial distribution function (RDF) is often utilized to reveal material structural features during MD simulations (Goudeli & Pratsinis, 2016; Akbarzadeh & Yaghoubi, 2014; Akbarzadeh & Abbaspour, 2016). The RDF curves given in Figure 5.5 show that the small peaks observable at $t = 0$ have mostly disappeared by $t = 100$ ps. However, at $t = 600$ ps, two small peaks, which are marked by small circles on the curve, show up again, which implies that the gold cluster has become more structured than that at $t = 100$ ps.

In a short summary, from the results in Figures 5.3 to 5.5 based on adaptive CNA, MSD and RDF, respectively, the simulated processes in the studied cases can be approximately divided into two stages. The first stage, which starts from $t = 0$ ps and lasts for roughly ~ 120 ps, features the fast approaching and merging of gold NPs. During this stage, the multiple gold NPs merge into one gold nanocluster and the atoms tend to change into a more disordered structure. The MSD value has a quick increase while in Figure 5.5 the initially observable small peaks on the RDF curve in the given radial distance range mostly disappear by $t = 100$ ps. The MSD increases faster as the diameter of the CNT in the system is larger. Then, the evolution during the second stage

features a partial restructuring of gold atoms in the nanocluster. The MD simulations have also revealed an interesting phenomenon (which has been rarely reported before to our best knowledge): a MWCNT with a sufficiently large diameter may draw atoms of metal NPs near the tube end into the tube at a temperature well below the melting point of the NPs.

5.2.2.2 Effect of Temperature on Coalescence and Interactions

Three targeted system temperatures at the end of the heating stage have been selected to study the effect of the temperature: ~600 K (below the melting point of 3-nm Au NPs), ~800 K (around the melting point) and ~1000 K (above the melting point). Figure 5.6 shows the cross sections of the systems at the end of the simulations ($t = 600$ ps).

Based on the adaptive CNA of the atomic structures, it can be seen from the second row of Figure 5.6 that when the targeted temperature is 800 K, all gold atoms in the image have become disordered at $t = 600$ ps in the presence of the CNT. However, for the system without the CNT on the first column, lattice structures can still be observed. This indicates that the existence of the CNT has helped the disordering of the adjacent gold nanocluster in the studied cases.

The entrance of gold atoms into the MWCNT is further promoted when the system temperature at the end of the heating stage is higher. At 800K and 1000K, gold atoms can fill out the inner tubes of the (10,10)-(15,15) and (15,15)-(20,20) MWCNTs; but no outflow of atoms has been observed at the other end of the tube. The remaining gold atoms outside of the tube tend to eventually form a reasonably spherical shape. Meanwhile, under the same high temperatures, the entrance of gold atoms into the (5,5)-(10,10) CNT (which has a small inner diameter of 0.68 nm) is still quite rare. There seems to be poor bonding between the gold cluster and the end of the CNT. Gold atoms may even detach from the end of the (5,5)-(10,10) CNT, and then attach to its sidewall at 1000 K. The MD-predicted results appear to suggest that in actual laser sintering process,

MWCNTs with larger diameters may have a better coalition and bonding with the gold phase due to the entrance of gold atoms into the tube. Certainly, this may still require further study to confirm.

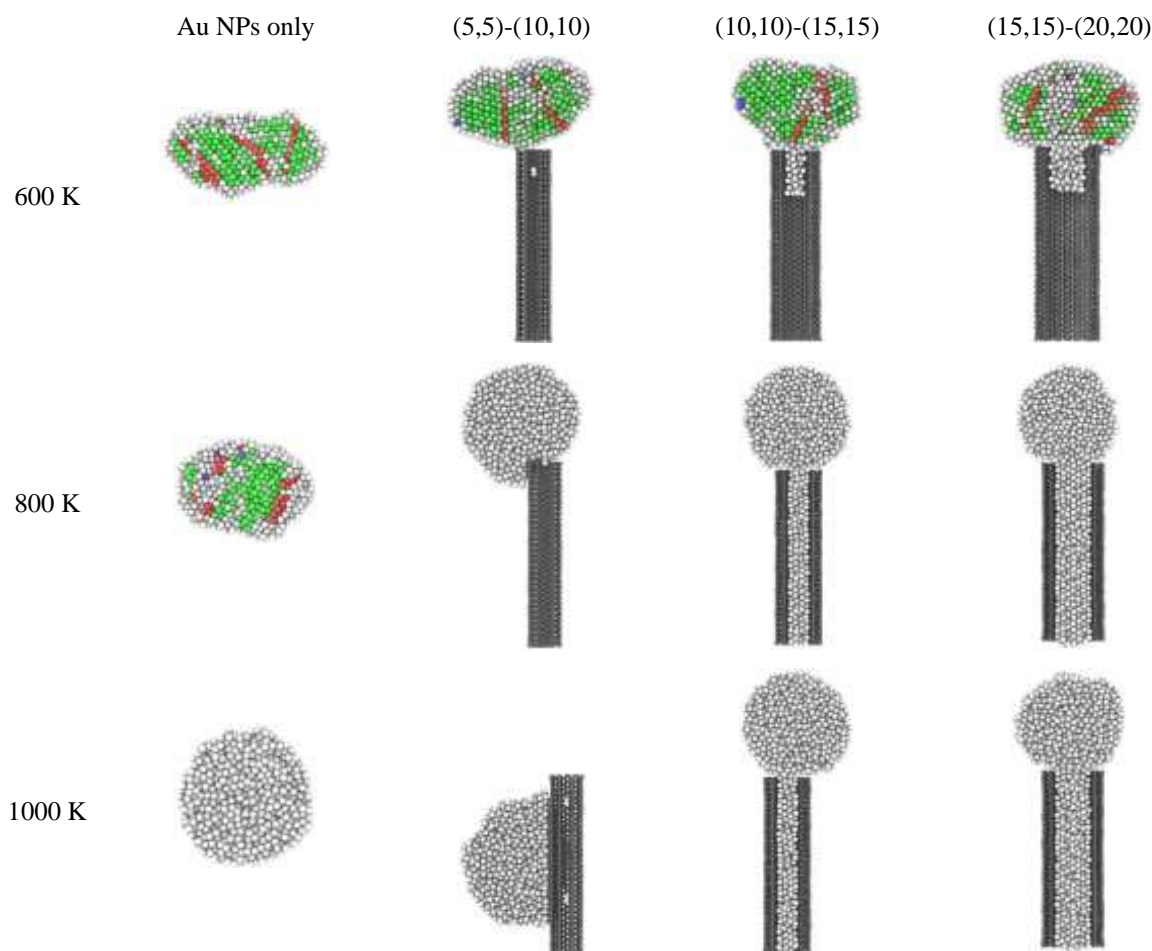


Figure 5.6 MD-predicted system situation at the end of the simulation period ($t = 600$ ps) (Column 1: system that only consists of Au NPs; Column 2, 3 and 4: system with Au NPs initially near the end of a MWCNT with different diameters. Different rows correspond to systems with different temperatures at the end of the heating stage. Images shown are for cross-sections of the systems. Carbon atoms are plotted in black, while gold atoms are plotted in colours representing their local atomic structures that are identified with the adaptive CNA approach (Stukowski, 2012). The green, blue and red colours represent fcc, bcc and hcp structures, respectively, while atoms with unidentified structures are plotted in white (such as surface atoms or disordered atoms))

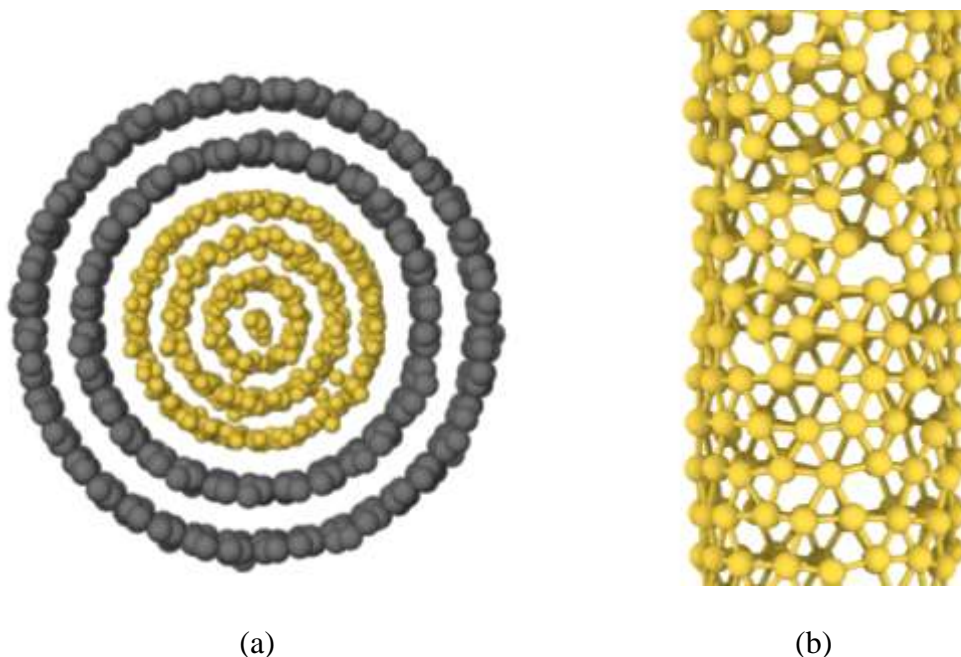


Figure 5.7 The (15,15)-(20,20) CNT and the gold atoms inside the CNT at $t = 600$ ps based on the MD simulation (system temperature at the end of the heating stage: $T = 800\text{K}$). (a) Top view of a cross section of the CNT. (b) Side view of the most external layer of the gold atoms inside the CNT. Carbon and gold atoms are plotted in black and yellow, respectively. In (b), bonds are drawn for the visualization purpose only.

It has been found from the simulations that the arrangement of the gold atoms inside a CNT is greatly affected by the tube. For example, for the system with $T = 800$ K at the end of the heating stage, the (15,15)-(20,20) MWCNT and the gold atoms inside the tube at $t = 600$ ps are shown in Figure 5.7. Figure 5.7a shows that most of the gold atoms inside the MWCNT are arranged in a multi-layer tube pattern. The three tube layers of the Au atoms have diameters of around 1.4, 0.9 and 0.45 nm, respectively. The most external layer of the gold atoms is shown in Figure 5.7b. Please note that the plotted bonds in Figure 5.7b are only for the visualization purpose and do not necessarily denote actual bonds between the gold atoms. Such an arrangement has been observed in all the simulated cases where significant entrance of Au atoms into the MWCNT occurs.

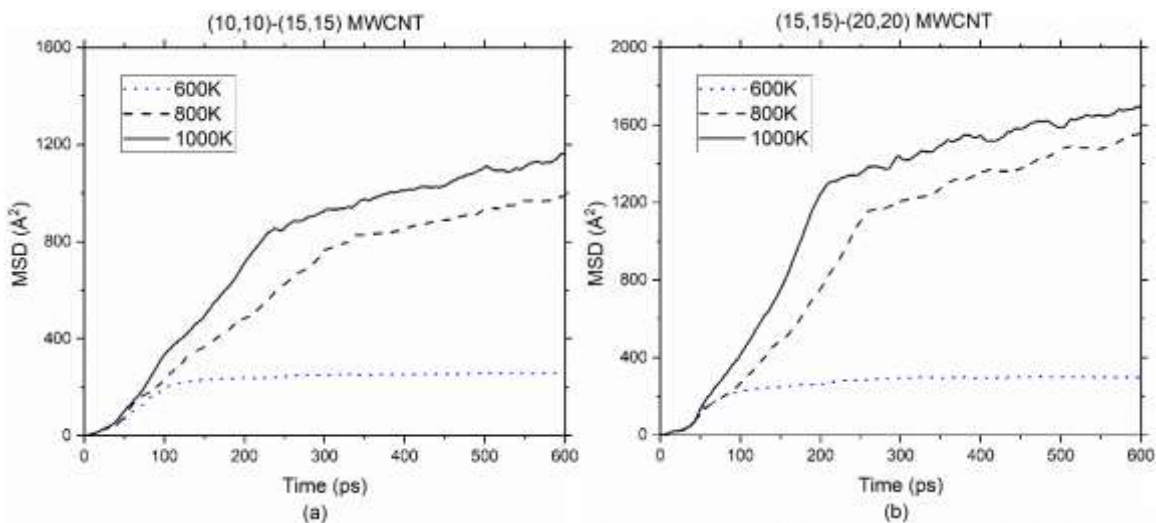


Figure 5.8 MD-predicted Mean Squared Displacement (MSD) of gold atoms around a: (a) (10, 10)-(15, 15) MWCNT, and (b) (15, 15)-(20, 20) MWCNT (the system temperature at the end of the 100-ps heating stage is indicated in the plots).

The curves of MSD versus time for gold NPs around a (10,10)-(15,15) MWCNT and those around a (15,15)-(20,20) MWCNT are shown in Figure 5.8a and b, respectively. For the first 100-ps period (which is the heating stage), the MSD curves at 600K and 800K are quite similar to each other. After $t = 100$ ps, the difference grows larger. The MSD curve for the situation of $T = 600$ K reaches a plateau while the MSD at 800K keeps growing very fast. It is expected that one important reason for the difference should be the larger amount of gold atoms entering the CNT at 800 K. The curves for 800K and 1000K look similar, except that overall the MSD at 1000 K is higher. For both the 800K and the 1000K situations, the gold atoms have saturated the MWCNT at the end of the simulation, and the shape of the gold nanocluster outside the CNT is reasonably spherical. Hence, the difference of the MSD values for the two situations should be mainly due to fiercer movements of atoms at the higher temperature of 1000 K.

Figure 5.9(a) and (b) shows the RDF curves for gold atoms at different times for a system with gold NPs and a (15, 15)-(20, 20) CNT and for a system with gold NPs only, respectively

(where the system temperature at the end of the heating stage is 800 K). Figure 5.9(a) shows that the small peaks initially on the RDF curve in the given radial distance range have mostly disappeared by the end of the 100-ps heating stage, and they do not clearly appear again by $t = 600$ ps. However, for the system with Au NPs only, Figure 5.9(b) shows two small peaks at $t = 600$ ps, which should be due to atomic restructuring. For all the simulated systems at $T = 1000\text{K}$, similar small peaks are absent at $t = 600$ ps. These observations from the RDF curves are consistent with the structural evolution results given in Figure 5.6 based on the adaptive CNA.

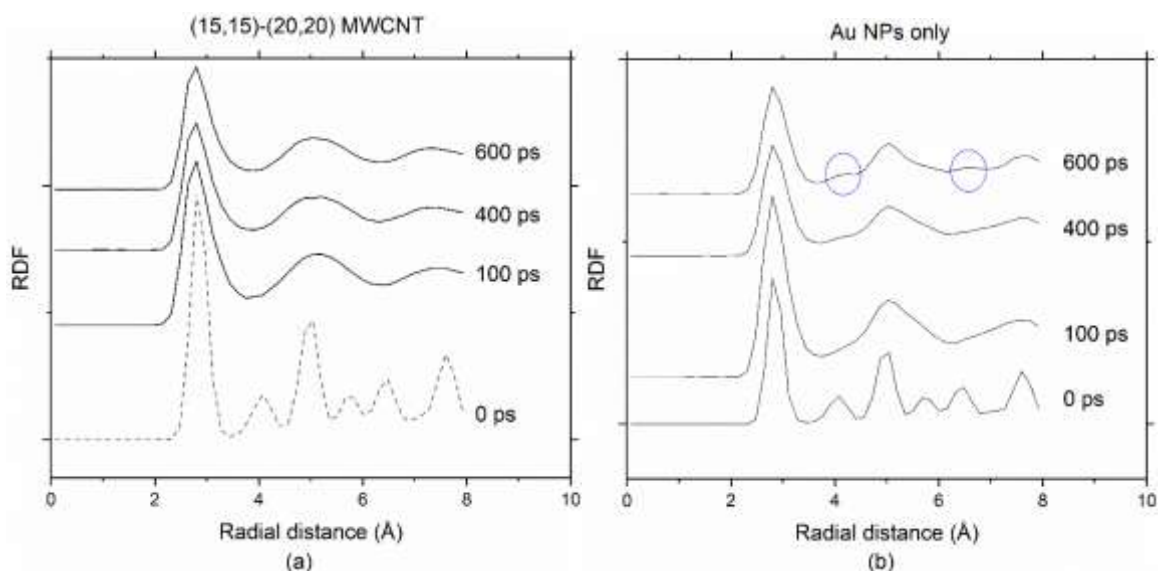


Figure 5.9 Radial distribution function (RDF) evolution of gold atoms for (a) a system with Au NPs initially around the end of a (15,15)-(20,20) MWCNT, and (b) a system with Au NPs only (the system temperature at the end of the heating stage is 800 K).

In this work, MD simulations have been performed for CNTs with parameters listed in Table 5.1 where the diameter of each CNT is calculated based on its chirality information (Georgantinos & Anifantis, 2009). It may be a good work in the future to study gold NPs' coalescence and interactions near the end of a CNT with other different parameters.

5.3 Conclusions

In this work, coalescence of 3-nm Au NPs around the end of a MWCNT and their interactions with the CNT have been studied through MD simulations. The simulated period includes a 100-ps heating period (at the end of which the system is raised to a certain heating temperature) followed by another 500-ps period in the NVE ensemble. Studies have been performed under different CNT diameters, and for different heating temperatures of 600 K (below the melting point of 3-nm Au NPs), 800 K (around the melting point) and 1000 K (above the melting point). From the simulated cases, the following discoveries have been made under the studied conditions:

1. Under a heating temperature of 600 K:
 - i. For the system with Au NPs only, two distinct evolution stages have been identified: the first stage features the merging of NPs into one gold nanocluster and the quick increasing of the gold MSD value; during the second stage, MSD no longer increases quickly, and restructuring of Au atoms occurs.
 - ii. For the systems with both Au NPs and a CNT, the system evolution still exhibits a similar two-stage behavior, but with a larger MSD at the end of the simulation period. However, when the CNT has a sufficiently large diameter, it can draw some Au atoms into the tube, even though the heating temperature (600 K) is well below the melting point of the NP. Such an interesting capillary effect of CNT below the NP melting point has been rarely reported before to our best knowledge. The MSD value at the end of the simulated period increases with the CNT diameter.
2. Under a heating temperature of 800 K:

- i. For the system with Au NPs only, lattice structures can still be observed in the merged Au nanocluster at the end of the simulated period.
 - ii. However, for the systems with both Au NPs and a CNT, the Au atoms become mostly disordered at the end of the simulated period. When the CNT has a sufficiently large diameter, Au atoms can fill out the inner tube of the CNT at the end of the simulated period; However, if the CNT diameter is too small, the entrance of Au atoms into the tube is rare.
3. Under a heating temperature of 1000 K, for both the system without a CNT and the systems with a CNT, the Au atoms become mostly disordered at the end of the simulated period. However, the entrance of Au atoms into the tube is still rare in the simulated period when the CNT diameter is too small, where the merged Au nanocluster may move away from the tube end to the tube sidewall.
4. If significant entrance of Au atoms into the CNT occurs, the arrangement of most Au atoms inside the CNT also follows a multi-layer tube pattern, where the axial direction of the gold tubes is the same as that for the CNT.

6. CONCLUSIONS AND FUTURE WORK

This chapter reviews the conclusions drawn from research reported in this thesis and gives some recommendations for potential future research.

6.1 Research Review and Conclusions

In this research, laser sintering of CNT- silver nanocomposites on flexible polyimide substrate have been studied. The samples are compared with those fabricated from laser sintering of silver nanoparticles by means of extensive characterizations and performance tests. Under the studied conditions and for the characterized samples, the following conclusions can be obtained from the current experimental study (the conclusions involving comparisons are for CNT-silver composite films and silver films fabricated under similar conditions):

1. SEM observations show that a) silver NPs are sintered together although pores still exist; b) some CNTs and the matrix phase appear to be in good contact.
2. Composites with addition of CNTs show no signs of degradation in electrical conductivity.
3. Laser sintered CNT-silver composite lines have an overall much better bending fatigue performance than the laser-sintered silver lines.
4. Performance in static tensile tests and adhesion tests is also improved with existence of CNTs in the composites. CNT-silver composite lines can resist larger tensile strains and have stronger adhesion with PI substrate.
5. It is expected that the underlying mechanisms for the better performance in mechanical tests may include: (a) some CNTs could run across cracks and provide channels for

electrical currents to flow across the cracks, and (b) CNTs can help inhibit the initiation and growth of the cracks.

6. Mechanical interlocking is expected to play an important role in the adhesion mechanism at the interface between the sintered CNT-silver composite and the PI substrate. Chemical reactions have likely occurred around the interface, while a significant diffusion of silver into the polyimide substrate is not observed.
7. For CNT-silver interfaces in laser-sintered CNT-silver composites, a significant amount of Ag-C chemical bonds is unlikely to exist.

A molecular dynamics simulation model was also developed to study the coalescence of gold nanoparticles around the end of a carbon nanotube. In the model calculations, five 3-nm Au nanoparticles were initially placed around the end of a multi-walled carbon nanotube with varying diameters. The system was assumed to be heated to different elevated temperatures that can be potentially achieved by laser heating and the nanoparticles started to coalesce and interact with the MWCNT. The following can be concluded from the simulation under the conditions studied:

1. Under a heating temperature of 600 K:
 - i. For the system with Au NPs only, two distinct evolution stages have been identified: during the first stage, NPs merge with each other and form one gold nanocluster, along with the quick increasing of the gold MSD value; during the second stage, MSD value stabilizes, and restructuring occurs in Au nanocluster.
 - ii. For the systems with both Au NPs and a CNT, the system evolution still consists of similar two stages, but with a larger MSD at the end of the simulation period. However, an interesting capillary effect was noted though the heating temperature (600 K) is well below the melting point of the 3-nm NP. Such a capillary effect of

CNT below the NP melting point has been rarely reported before to our best knowledge.

2. Under a heating temperature of 800 K:
 - i. For the system with Au NPs only, lattice structures can still be observed in the merged Au nanocluster at the end of the simulated period.
 - ii. For the systems with both Au NPs and a CNT, the Au atoms become mostly disordered at the end of the simulated period. When the diameter of CNT is sufficiently large, Au atoms can fill up the inner tube of the CNT during the simulated period; However, if the CNT diameter is too small, the entrance of Au atoms into the tube is rare.
3. Under a heating temperature of 1000 K, the Au atoms become mostly disordered at the end of the simulation in both systems. However, the entrance of Au atoms into the tube is still rare during the simulation when the CNT diameter is too small, where the merged Au nanocluster may move away from the tube end and attach to the tube sidewall.
4. If significant entrance of Au atoms into the CNT occurs, the arrangement of most Au atoms inside the CNT also follows a multi-layer tube pattern, where the axial direction of the gold tubes is the same as that for the CNT.

6.2 Recommendations for Potential Future Research

Laser-based fabrication of CNT-metal composite on flexible substrate has potential applications in flexible electronics for enhancing the durability and reliability. Several related areas are worth more exploration in the future, for example:

First, it could be good work in the future to study the spatial resolution aspect of laser fabrication by using smaller laser spot sizes.

Second, future work may also explore the application of the laser-based nanocomposite fabrication process in the manufacturing of specific flexible electronic devices.

REFERENCES

- Ahmad, I., Unwin, M., Cao, H., Chen, H., Zhao, H., Kennedy, A., & Zhu, Y. Q. (2010). Multi-walled carbon nanotubes reinforced Al₂O₃ nanocomposites: Mechanical properties and interfacial investigations. *Composites Science and Technology*, *70*(8), 1199–1206. <http://doi.org/10.1016/j.compscitech.2010.03.007>
- Akbarzadeh, H., & Yaghoubi, H. (2014). Molecular dynamics simulations of silver nanocluster supported on carbon nanotube. *Journal of Colloid and Interface Science*, *418*(C), 178–184. <http://doi.org/10.1016/j.jcis.2013.12.006>
- Akbarzadeh, H., & Abbaspour, M. (2016). Investigation of melting and freezing of Ag–Au alloy nanoclusters supported on carbon nanotube using molecular dynamics simulations. *Journal of Molecular Liquids*, *216*(C), 671–682. <http://doi.org/10.1016/j.molliq.2016.02.007>
- Akogwu, O., Kwabi, D., Midturi, S., Eleruja, M., Babatope, B., & Soboyejo, W. O. (2010). Large strain deformation and cracking of nano-scale gold films on PDMS substrate. *Materials Science and Engineering: B*, *170*(1-3), 32–40. <http://doi.org/10.1016/j.mseb.2010.02.023>
- Allen, M. P., & Tildesley, D. J. (1989). *Computer Simulation of Liquids*. Clarendon Press.
- Anand, U., Lu, J., Loh, D., Aabdin, Z., & Mirsaidov, U. (2015). Hydration Layer-Mediated Pairwise Interaction of Nanoparticles. *Nano Letters*, *16*(1), 786–790. <http://doi.org/10.1021/acs.nanolett.5b04808>
- Arcidiacono, S., Bieri, N. R., Poulidakos, D., & Grigoropoulos, C. P. (2004). On the coalescence of gold nanoparticles. *International Journal of Multiphase Flow*, *30*(7-8), 979–994. <http://doi.org/10.1016/j.ijmultiphaseflow.2004.03.006>
- Asoro, M. A., Kovar, D., & Ferreira, P. J. (2013). In situ transmission electron microscopy observations of sublimation in silver nanoparticles. *ACS Nano*, *7*(9), 7844–7852. <http://doi.org/10.1021/nn402771j>

- Asoro, M. A., Kovar, D., Shao-Horn, Y., Allard, L. F., & Ferreira, P. J. (2009). Coalescence and sintering of Pt nanoparticles: in situ observation by aberration-corrected HAADF STEM, *21*(2), 025701–7. <http://doi.org/10.1088/0957-4484/21/2/025701>
- Bachtold, A., Henny, M., Terrier, C., Strunk, C., Schönenberger, C., Salvetat, J. P., et al. (1998). Contacting carbon nanotubes selectively with low-ohmic contacts for four-probe electric measurements. *Applied Physics Letters*, *73*(2), 274–276. <http://doi.org/10.1063/1.121778>
- Banks, M. (2010). Flexible electronics enters the e-reader market. *Physics World*. <http://doi.org/10.1088/2058-7058/25/07/13>
- Beamson, G., & Briggs, D. (1992). High Resolution XPS of Organic Polymers. The Scienta ESCA300 Database. Chichester, New York. John Wiley & Sons. <https://pubs.acs.org/doi/10.1021/ed070pA25.5>
- Begley, M. R., Scott, O. N., Utz, M., & Bart-Smith, H. (2009). Fracture of nanoscale copper films on elastomer substrates, *95*(23), 231914–4. <http://doi.org/10.1063/1.3268458>
- Buffat, P., & Borel, J.-P. (1976). Size effect on the melting temperature of gold particles. *Physical Review A*, *13*(6), 2287–2298. <http://doi.org/10.1103/PhysRevA.13.2287>
- Cordill, M. J. (2010). Flexible film systems: Current understanding and future prospects. *Jom*, *62*(6), 9–14. <http://doi.org/10.1007/s11837-010-0096-5>
- Cui, J., Yang, L., Zhou, L., & Wang, Y. (2014). Nanoscale Soldering of Axially Positioned Single-Walled Carbon Nanotubes: A Molecular Dynamics Simulation Study. *ACS Applied Materials & Interfaces*, *6*(3), 2044–2050. <http://doi.org/10.1021/am405114n>
- Deng, C. F., Zhang, X. X., Wang, D. Z., & Ma, Y. X. (2007). Calorimetric study of carbon nanotubes and aluminum. *Materials Letters*, *61*(14-15), 3221–3223. <http://doi.org/10.1016/j.matlet.2006.11.037>

- Dujardin, E., Ebbesen, T. W., Krishnan, A., & Treacy, M. M. J. (1998). Wetting of Single Shell Carbon Nanotubes. *Advanced Materials*, *10*(17), 1472–1475.
[http://doi.org/10.1002/\(SICI\)1521-4095\(199812\)10:17<1472::AID-ADMA1472>3.0.CO;2-R](http://doi.org/10.1002/(SICI)1521-4095(199812)10:17<1472::AID-ADMA1472>3.0.CO;2-R)
- E. I. du Pont de Nemours and Company. (2018). *DuPont Kapton HN polyimide film datasheet* (pp. 1–4). Retrieved from <http://www.dupont.com/content/dam/dupont/products-and-services/membranes-and-films/polyimide-films/documents/DEC-Kapton-HN-datasheet.pdf>
- Erol, M., Han, Y., Stanley, S. K., Stafford, C. M., Du, H., & Sukhishvili, S. (2009). SERS Not To Be Taken for Granted in the Presence of Oxygen. *Journal of the American Chemical Society*, *131*(22), 7480–7481. <http://doi.org/10.1021/ja807458x>
- Estili, M., Kawasaki, A., Sakamoto, H., Mekuchi, Y., Kuno, M., & Tsukada, T. (2008). The homogeneous dispersion of surfactantless, slightly disordered, crystalline, multiwalled carbon nanotubes in α -alumina ceramics for structural reinforcement. *Acta Materialia*, *56*(15), 4070–4079. <http://doi.org/10.1016/j.actamat.2008.04.029>
- Fairley, N.; Casa Software Ltd. (2009). CasaXPS manual 2.3.15 Introductino to XPS and AES. <http://www.casaxps.com/ebooks/XPS%20AES%20Book%20new%20margins%20rev%201.2%20for%20web.pdf>
- Faupel, F., Willecke, R., & Thran, A. (1998). Diffusion of metals in polymers. *Materials Science and Engineering: R: Reports*, *22*(1), 1–55. [http://doi.org/10.1016/S0927-796X\(97\)00020-X](http://doi.org/10.1016/S0927-796X(97)00020-X)
- Faupel, F., Zaporojtchenko, V., Thran, A., Strunskus, T., & Kiene, M. (2005). Metal Diffusion in Polymers and on Polymer Surfaces. In *Diffusion Processes in Advanced Technological Materials* (pp. 333–363). Springer, Berlin, Heidelberg. https://doi.org/10.1007/978-3-540-27470-4_7
- Feng, Y., Yuan, H. L., & Zhang, M. (2005). Fabrication and properties of silver-matrix composites reinforced by carbon nanotubes. *Materials Characterization*, *55*(3), 211–218. <http://doi.org/10.1016/j.matchar.2005.05.003>

- Foiles, S. M., Baskes, M. I., & Daw, M. S. (1986). Embedded-atom-method functions for the fcc metals Cu, Ag, Au, Ni, Pd, Pt, and their alloys. *Physical Review B*, 33(12), 7983–7991. <http://doi.org/10.1103/PhysRevB.33.7983>
- Foitzik, A., & Faupel, F. (1990). Structural Investigation of the Silver—Polyimide Interface by Cross—Sectional Ten and Ion—Beam Sputtering. *MRS Online Proceedings Library Archive*, 203, 1–6. <http://doi.org/10.1557/PROC-203-59>
- Fukuda, K., & Someya, T. (2017). Recent Progress in the Development of Printed Thin-Film Transistors and Circuits with High-Resolution Printing Technology. *Advanced Materials (Deerfield Beach, Fla.)*, 29(25). <http://doi.org/10.1002/adma.201602736>
- Gaarenstroom, S. W., & Winograd, N. (1977). Initial and final state effects in the ESCA spectra of cadmium and silver oxides. *The Journal of Chemical Physics*, 67(8), 3500–3506. <http://doi.org/10.1063/1.435347>
- Galuska, A. A., Uht, J. C., & Marquez, N. (1988). Reactive and nonreactive ion mixing of Ti films on carbon substrates. *Journal of Vacuum Science & Technology a: Vacuum, Surfaces, and Films*, 6(1), 110–122. <http://doi.org/10.1116/1.574992>
- Georgantzinis, S. K., & Anifantis, N. K. (2009). Vibration analysis of multi-walled carbon nanotubes using a spring–mass based finite element model. *Computational Materials Science*, 47(1), 168–177. <http://doi.org/10.1016/j.commat.2009.07.006>
- González-Rubio, G., Guerrero-Martínez, A., & Liz-Marzán, L. M. (2016). Reshaping, Fragmentation, and Assembly of Gold Nanoparticles Assisted by Pulse Lasers. *Accounts of Chemical Research*, 49(4), 678–686. <http://doi.org/10.1021/acs.accounts.6b00041>
- Goudeli, E., & Pratsinis, S. E. (2016). Crystallinity dynamics of gold nanoparticles during sintering or coalescence. *AIChE Journal*, 62(2), 589–598. <http://doi.org/10.1002/aic.15125>
- Govindaraj, A., Satishkumar, B. C., Nath, M., & Rao, C. N. R. (2000). Metal Nanowires and Intercalated Metal Layers in Single-Walled Carbon Nanotube Bundles. *Chemistry of Materials*, 12(1), 202–205. <http://doi.org/10.1021/cm990546o>

- Grunze, M., & Lamb, R. N. (1988). Adhesion of vapour phase deposited ultra-thin polyimide films on polycrystalline silver. *Surface Science*, 204(1-2), 183–212. [http://doi.org/10.1016/0039-6028\(88\)90276-2](http://doi.org/10.1016/0039-6028(88)90276-2)
- Guevara-Chapa, E., & Mejía-Rosales, S. (2014). Molecular dynamics of coalescence and collisions of silver nanoparticles. *Journal of Nanoparticle Research*, 16(12), 2757–10. <http://doi.org/10.1007/s11051-014-2757-8>
- Han, W.-S., Hong, J.-M., Kim, H.-S., & Song, Y.-W. (2011). Multi-pulsed white light sintering of printed Cu nanoinks. *Nanotechnology*, 22(39), 395705. <http://doi.org/10.1088/0957-4484/22/39/395705>
- Håkansson, K. L., Johansson, H. I. P., & Johansson, L. I. (1994). High-resolution core-level study of hexagonal WC(0001). *Physical Review B*, 49(3), 2035–2039. <http://doi.org/10.1103/PhysRevB.49.2035>
- Hong, S., Yeo, J., Kim, G., Kim, D., Lee, H., Kwon, J., et al. (2013). Nonvacuum, Maskless Fabrication of a Flexible Metal Grid Transparent Conductor by Low-Temperature Selective Laser Sintering of Nanoparticle Ink, 7(6), 5024–5031. <http://doi.org/10.1021/nn400432z>
- Hoover, W. G. (2012). Computational statistical mechanics (pp. 33–34). Elsevier.
- Hu, Y., Liu, Y., Li, Z., & Sun, Y. (2014). Highly Asymmetric, Interfaced Dimers Made of Au Nanoparticles and Bimetallic Nanoshells: Synthesis and Photo-Enhanced Catalysis. *Advanced Functional Materials*, 24(19), 2828–2836. <http://doi.org/10.1002/adfm.201303557>
- Humphrey, W., Dalke, A., & Schulten, K. (1996). VMD: Visual molecular dynamics. *Journal of Molecular Graphics*, 14(1), 33–38. [http://doi.org/10.1016/0263-7855\(96\)00018-5](http://doi.org/10.1016/0263-7855(96)00018-5)
- Hwang, H.-J., & Malhotra, R. (2018). Shape-Tuned Junction Resistivity and Self-Damping Dynamics in Intense Pulsed Light Sintering of Silver Nanostructure Films. *ACS Applied Materials & Interfaces*, 11(3), 3536–3546. <http://doi.org/10.1021/acsami.8b17644>

- Hwang, H.-J., Joo, S.-J., & Kim, H.-S. (2015). Copper Nanoparticle/Multiwalled Carbon Nanotube Composite Films with High Electrical Conductivity and Fatigue Resistance Fabricated via Flash Light Sintering. *ACS Applied Materials & Interfaces*, 7(45), 25413–25423. <http://doi.org/10.1021/acsami.5b08112>
- Iijima, S. (1991). Helical microtubules of graphitic carbon. *Nature*, 354(6348), 56–58. <http://doi.org/10.1038/354056a0>
- Jackson, S. T., & Nuzzo, R. G. (1995). Determining hybridization differences for amorphous carbon from the XPS C 1s envelope. *Applied Surface Science*, 90(2), 195–203. [http://doi.org/10.1016/0169-4332\(95\)00079-8](http://doi.org/10.1016/0169-4332(95)00079-8)
- Ji, S. Y., Ajmal, C. M., Kim, T., Chang, W. S., & Baik, S. (2017). Laser patterning of highly conductive flexible circuits, 28(16), 165301–8. <http://doi.org/10.1088/1361-6528/aa66a2>
- Jiang, J., Bin Bao, Li, M., Sun, J., Zhang, C., Li, Y., et al. (2016). Fabrication of Transparent Multilayer Circuits by Inkjet Printing. *Advanced Materials (Deerfield Beach, Fla.)*, 28(7), 1420–1426. <http://doi.org/10.1002/adma.201503682>
- Jiang, L., Gao, L., & Sun, J. (2003). Production of aqueous colloidal dispersions of carbon nanotubes. *Journal of Colloid and Interface Science*, 260(1), 89–94. [http://doi.org/10.1016/s0021-9797\(02\)00176-5](http://doi.org/10.1016/s0021-9797(02)00176-5)
- Jiang, S., Zhang, Y., Gan, Y., Chen, Z., & Peng, H. (2013). Molecular dynamics study of neck growth in laser sintering of hollow silver nanoparticles with different heating rates. *Journal of Physics D: Applied Physics*, 46(33), 335302–12. <http://doi.org/10.1088/0022-3727/46/33/335302>
- Kamshny, A. & Magdassi, S. (2014). Conductive Nanomaterials for Printed Electronics. *Small*, 10(17), 3515. <http://doi.org/10.1002/smll.201303000>
- Kang, H., Sowade, E., & Baumann, R. R. (2014). Direct Intense Pulsed Light Sintering of Inkjet-Printed Copper Oxide Layers within Six Milliseconds. *ACS Applied Materials & Interfaces*, 6(3), 1682–1687. <http://doi.org/10.1021/am404581b>

- Kang, Z., Wu, B., Wang, R., & Wu, W. (2018a). Laser-Based Fabrication of Carbon Nanotube–Silver Composites With Enhanced Fatigue Performance Onto a Flexible Substrate. *Journal of Manufacturing Science and Engineering*, *140*(9), 091005. <http://doi.org/10.1115/1.4039492>
- Kang, Z., & Wu, B. (2018b). Coalescence of gold nanoparticles around the end of a carbon nanotube: A molecular-dynamics study. *Journal of Manufacturing Processes*, *34*, 785–792. <http://doi.org/10.1016/j.jmapro.2018.03.051>
- Kaushik, V. K. (1991). XPS core level spectra and Auger parameters for some silver compounds. *Journal of Electron Spectroscopy and Related Phenomena*, *56*(3), 273–277. [http://doi.org/10.1016/0368-2048\(91\)85008-H](http://doi.org/10.1016/0368-2048(91)85008-H)
- Kim, T. H. (2014). Bonding. In *CIRP Encyclopedia of Production Engineering* (Vol. 4, pp. 102–105). Berlin, Heidelberg: Springer, Berlin, Heidelberg. http://doi.org/10.1007/978-3-642-20617-7_6618
- Ko, S. H., Pan, H., Grigoropoulos, C. P., Luscombe, C. K., Fréchet, J. M. J., & Poulidakos, D. (2007a). Air stable high resolution organic transistors by selective laser sintering of ink-jet printed metal nanoparticles. *Applied Physics Letters*, *90*(14), 141103. <http://doi.org/10.1063/1.2719162>
- Ko, S. H., Pan, H., Grigoropoulos, C. P., Luscombe, C. K., Fréchet, J. M. J., & Poulidakos, D. (2007b). All-inkjet-printed flexible electronics fabrication on a polymer substrate by low-temperature high-resolution selective laser sintering of metal nanoparticles. *Nanotechnology*, *18*(34). <http://doi.org/10.1088/0957-4484/18/34/345202>
- Ko, S. H., Pan, H., Lee, D., Grigoropoulos, C. P., & Park, H. K. (2010). Nanoparticle selective laser processing for a flexible display fabrication. *Japanese Journal of Applied Physics*, *49*(5 PART 2). <http://doi.org/10.1143/JJAP.49.05EC03>
- Kumpulainen, T., Pekkanen, J., Valkama, J., Laakso, J., Tuokko, R., & Mäntysalo, M. (2011). Low temperature nanoparticle sintering with continuous wave and pulse lasers, *43*(3), 570–576. <http://doi.org/10.1016/j.optlastec.2010.08.002>

- Laha, T., Agarwal, A., McKechnie, T., & Seal, S. (2004). Synthesis and characterization of plasma spray formed carbon nanotube reinforced aluminum composite. *Materials Science & Engineering A*, 381(1-2), 249–258. <http://doi.org/10.1016/j.msea.2004.04.014>
- Lange, A. P., Samanta, A., Majidi, H., Mahajan, S., Ging, J., Olson, T. Y., et al. (2016). Dislocation mediated alignment during metal nanoparticle coalescence. *Acta Materialia*, 120(C), 364–378. <http://doi.org/10.1016/j.actamat.2016.08.061>
- Li, H., Misra, A., Horita, Z., Koch, C. C., Mara, N. A., Dickerson, P. O., & Zhu, Y. (2009). Strong and ductile nanostructured Cu-carbon nanotube composite, 95(7), 071907–4. <http://doi.org/10.1063/1.3211921>
- Lim, H. S., Kim, S. J., Jang, H. W., & Lim, J. A. (2017). Intense pulsed light for split-second structural development of nanomaterials. *Journal of Materials Chemistry C*, 5(29), 7142–7160. <http://doi.org/10.1039/C7TC01848G>
- Liu, H. B., Jos Yacaman, M., Perez, R., & Ascencio, J. A. (2003). Studies of nanocluster coalescence at high temperature. *Applied Physics A*, 77(1), 63–67. <http://doi.org/10.1007/s00339-002-2028-x>
- Loctite (2014). Super glue ultra gel control® technical datasheet. Retrieved May 22, 2019. http://www.loctiteproducts.com/tds/SG_UG_CNTRL_tds.pdf
- Louette, P., Bodino, F., & Pireaux, J.-J. (2005). Polyimide XPS Reference Core Level and Energy Loss Spectra. *Surface Science Spectra*, 12(1), 121–126. <http://doi.org/10.1116/11.20051101>
- Macková, A., Švorčík, V., Sajdl, P., Strýhal, Z., Pavlík, J., Malinský, P., & Šlouf, M. (2007). RBS, XPS, and TEM study of metal and polymer interface modified by plasma treatment. *Vacuum*, 82(2), 307–310. <http://doi.org/10.1016/j.vacuum.2007.07.027>

- Maekawa, K., Yamasaki, K., Niizeki, T., Mita, M., Matsuba, Y., Terada, N., & Saito, H. (2009). Influence of wavelength on laser sintering characteristics of Ag nanoparticles (pp. 1579–1584). Presented at the Proceedings - Electronic Components and Technology Conference, IEEE. <http://doi.org/10.1109/ECTC.2009.5074224>
- Mather, R. R. (2009). Surface modification of textiles by plasma treatments. In *Surface Modification of Textiles* (pp. 296–317). Woodhead Publishing. <http://doi.org/10.1533/9781845696689.296>
- McEuen, P. L., Fuhrer, M. S., & Park, H. (2002). Single-walled carbon nanotube electronics. *IEEE Transactions on Nanotechnology*, *1*(1), 78–84. <http://doi.org/10.1109/TNANO.2002.1005429>
- Mehrer, H. (2007). Diffusion in solids: fundamentals, methods, materials, diffusion-controlled processes.
- Moon, Y. J., Kang, H., Kang, K., Moon, S.-J., & Hwang, J. Y. (2015). Effect of Thickness on Surface Morphology of Silver Nanoparticle Layer During Furnace Sintering. *Journal of Electronic Materials*, *44*(4), 1192–1199. <http://doi.org/10.1007/s11664-015-3639-2>
- Neek-Amal, M., Asgari, R., & Rahimi Tabar, M. R. (2009). The formation of atomic nanoclusters on graphene sheets. *Nanotechnology*, *20*(13), 135602. <http://doi.org/10.1088/0957-4484/20/13/135602>
- Niittynen, J., Sowade, E., Kang, H., Baumann, R. R., & Mäntysalo, M. (2015). Comparison of laser and intense pulsed light sintering (IPL) for inkjet-printed copper nanoparticle layers. *Scientific Reports*, *5*(1), 8832. <http://doi.org/10.1038/srep08832>
- NIST X-ray Photoelectron Spectroscopy Database, NIST Standard Reference Database Number 20, National Institute of Standards and Technology, Gaithersburg MD, 20899 (2000), <http://dx.doi.org/10.18434/T4T88K>

- Pan, H., Ko, S. H., & Grigoropoulos, C. P. (2007). The coalescence of supported gold nanoparticles induced by nanosecond laser irradiation. *Applied Physics a: Materials Science & Processing*, *90*(2), 247–253. <http://doi.org/10.1007/s00339-007-4320-2>
- Pan, H., Ko, S. H., & Grigoropoulos, C. P. (2008). The Solid-State Neck Growth Mechanisms in Low Energy Laser Sintering of Gold Nanoparticles: A Molecular Dynamics Simulation Study, *130*(9), 092404. <http://doi.org/10.1115/1.2943303>
- Paramsothy, M., Hassan, S. F., Srikanth, N., & Gupta, M. (2010). Simultaneous Enhancement of Tensile/Compressive Strength and Ductility of Magnesium Alloy AZ31 Using Carbon Nanotubes. *Journal of Nanoscience and Nanotechnology*, *10*(2), 956–964. <http://doi.org/10.1166/jnn.2010.1809>
- Perelaer, J., Smith, P. J., Mager, D., Soltman, D., Volkman, S. K., Subramanian, V., et al. (2010). Printed electronics: the challenges involved in printing devices, interconnects, and contacts based on inorganic materials. *J. Mater. Chem.*, *20*(39), 8446–8453. <http://doi.org/10.1039/c0jm00264j>
- Plimpton, S. (1995). Fast Parallel Algorithms for Short-Range Molecular Dynamics. *Journal of Computational Physics*, *117*(1), 1–19. <http://doi.org/10.1006/jcph.1995.1039>
- Rapaport, D. C. (2004). *The Art of Molecular Dynamics Simulation* by D. C. Rapaport (2nd ed.). Cambridge: Cambridge University Press. <http://doi.org/10.1017/CBO9780511816581>
- Reich, S., Mazur, S., Avakian, P., & Wilson, F. C. (1987). Sintering of silver interlayers in polyimide films. *Journal of Applied Physics*, *62*(1), 287–292. <http://doi.org/10.1063/1.339142>
- Sambles, J. R. (1971). An Electron Microscope Study of Evaporating Gold Particles: The Kelvin Equation for Liquid Gold and the Lowering of the Melting Point of Solid Gold Particles. *Proceedings of the Royal Society a: Mathematical, Physical and Engineering Sciences*, *324*(1558), 339–351. <http://doi.org/10.1098/rspa.1971.0143>

- Schebarchov, D., & Hendy, S. C. (2008). Capillary Absorption of Metal Nanodroplets by Single-Wall Carbon Nanotubes. *Nano Letters*, 8(8), 2253–2257. <http://doi.org/10.1021/nl080875s>
- Shen, W., Zhang, X., Huang, Q., Xu, Q., & Song, W. (2014). Preparation of solid silver nanoparticles for inkjet printed flexible electronics with high conductivity. *Nanoscale*, 6(3), 1622–1628. <http://doi.org/10.1039/C3NR05479A>
- Short, K., & Van Buren, D. (2014). Printable Spacecraft: Flexible Electronic Platforms for NASA Missions.[Final Report: Early Stage Innovation, NASA Innovative Advanced Concepts (NIAC) Phase 2].
- Sloan, J., Wright, D. M., Bailey, S., Brown, G., York, A. P. E., Coleman, K. S., et al. (1999). Capillarity and silver nanowire formation observed in single walled carbon nanotubes. *Chemical Communications*, (8), 699–700. <http://doi.org/10.1039/a901572h>
- Stuart, S. J., Tutein, A. B., & Harrison, J. A. (2000). A reactive potential for hydrocarbons with intermolecular interactions. *The Journal of Chemical Physics*, 112(14), 6472. <http://doi.org/10.1063/1.481208>
- Stukowski, A. (2009). Visualization and analysis of atomistic simulation data with OVITO—the Open Visualization Tool, 18(1), 015012. <http://doi.org/10.1088/0965-0393/18/1/015012>
- Stukowski, A. (2012). Structure identification methods for atomistic simulations of crystalline materials. *Modelling and Simulation in Materials Science and Engineering*, 20(4), 045021. <http://doi.org/10.1088/0965-0393/20/4/045021>
- Subramaniam, C., Yamada, T., Kobashi, K., Sekiguchi, A., Futaba, D. N., Yumura, M., & Hata, K. (2013). One hundred fold increase in current carrying capacity in a carbon nanotube–copper composite. *Nature Communications*, 4(1), 75. <http://doi.org/10.1038/ncomms3202>
- Tekin, E., Smith, P. J., & Schubert, U. S. (2008). Inkjet printing as a deposition and patterning tool for polymers and inorganic particles. *Soft Matter*, 4(4), 703–713. <http://doi.org/10.1039/b711984d>

- Theodorakos, I., Zacharatos, F., Geremia, R., Karnakis, D., & Zergioti, I. (2015). Selective laser sintering of Ag nanoparticles ink for applications in flexible electronics. *Applied Surface Science*, *336*, 157–162. <http://doi.org/10.1016/j.apsusc.2014.10.120>
- Tjeng, L. H., Meinders, M. B. J., Van Elp, J., Ghijsen, J., Sawatzky, G. A., & Johnson, R. L. (1990). Electronic structure of Ag₂O. *Physical Review B*, *41*(5), 3190–3199. <http://doi.org/10.1103/PhysRevB.41.3190>
- Treacy, M. M. J., Ebbesen, T. W., & Gibson, J. M. (1996). Exceptionally high Young's modulus observed for individual carbon nanotubes. *Nature*, *381*(6584), 678–680. <http://doi.org/10.1038/381678a0>
- Wang, J., Chen, S., Cui, K., Li, D., & Chen, D. (2016). Approach and Coalescence of Gold Nanoparticles Driven by Surface Thermodynamic Fluctuations and Atomic Interaction Forces. *ACS Nano*, *10*(2), 2893–2902. <http://doi.org/10.1021/acsnano.5b08236>
- Wong, W. S., & Salleo, A. (2009). Flexible electronics: materials and applications. New York: Springer Science & Business Media, LLC. <http://doi.org/10.1007/978-0-387-74363-9>
- Wu, B., (2017), Laser-based Fabrication of Carbon Nanotube–Metal Composites on Flexible Substrates, U.S. Patent Application No. US15/729078. Filed on October 10, 2017 (the previous related provisional patent application number: 62406556. Filed on October 11, 2016). <https://patents.google.com/patent/US20180102200A1/en>
- Xia, Z., Curtin, W. A., & Sheldon, B. W. (2004). Fracture Toughness of Highly Ordered Carbon Nanotube/Alumina Nanocomposites. *Journal of Engineering Materials and Technology*, *126*(3), 238–244. <http://doi.org/10.1115/1.1751179>
- Yu, M.-F., Files, B. S., Arepalli, S., & Ruoff, R. S. (2000). Tensile Loading of Ropes of Single Wall Carbon Nanotubes and their Mechanical Properties, *84*(24), 5552–5555. <http://doi.org/10.1103/PhysRevLett.84.5552>

- Zhao, D., Liu, T., Park, J. G., Zhang, M., Chen, J.-M., & Wang, B. (2012). Conductivity enhancement of aerosol-jet printed electronics by using silver nanoparticles ink with carbon nanotubes. *Microelectronic Engineering*, *96*, 71–75.
<http://doi.org/10.1016/j.mee.2012.03.004>
- Zhao, S. J., Wang, S. Q., & Yang, Z. Q. (2001). Coalescence of three silver nanoclusters: a molecular dynamics study. *Journal of Physics: ...*, *13*(35), 8061–8069.
<http://doi.org/10.1088/0953-8984/13/35/313>
- Zhao, S., Zheng, Z., Huang, Z., Dong, S., Luo, P., Zhang, Z., & Wang, Y. (2016). Cu matrix composites reinforced with aligned carbon nanotubes_ Mechanical, electrical and thermal properties. *Materials Science & Engineering A*, *675*(C), 82–91.
<http://doi.org/10.1016/j.msea.2016.08.044>
- Zhao, W., Rovere, T., Weerawarne, D., Osterhoudt, G., Kang, N., Joseph, P., et al. (2015). Nanoalloy Printed and Pulse-Laser Sintered Flexible Sensor Devices with Enhanced Stability and Materials Compatibility., *9*(6), 6168–6177.
<http://doi.org/10.1021/acsnano.5b02704>

VITA

Zheng Kang is from Henan Province of P. R. China. He received Bachelor of Engineering degree in 2008 from Department of Mechanical Engineering at Hangzhou Dianzi University (Hangzhou, P. R. China). Then he got the opportunity to advance his study in Mechanical Engineering at Shanghai Jiao Tong University (Shanghai, P. R. China), where he received Master of Science in Engineering degree in 2011. After working for two years at China Automotive Engineering Research Institute, Chongqing, China, he came to Illinois Institute of Technology (Chicago, IL, USA) in 2013 and joined Dr. Benxin Wu's group. He is currently a Ph. D. candidate in the School of Mechanical Engineering at Purdue University (West Lafayette, IN, USA). His research interest focuses on laser-based fabrication of nano materials, enhancement of material properties, laser-based micro-machining and material processing.

PUBLICATIONS

Journal papers published or accepted:

1. Zheng Kang, Benxin Wu, Ruoxing Wang, Wenzhuo Wu, Laser-based fabrication of carbon nanotube – silver composites with enhanced fatigue performance onto a flexible substrate, *Journal of Manufacturing Science and Engineering*, 2018, 140(9), 091005
2. Zheng Kang, Benxin Wu, Coalescence of gold nanoparticles around the end of a carbon nanotube: a molecular-dynamics study, *Journal of Manufacturing Processes*, 2018, 34(B), p. 785-792.
3. Hanyu Song, Zheng Kang, Ze Liu, Benxin Wu. Experimental Study of Double-Pulse Laser Micro Sintering: A Novel Laser Micro Sintering Process, *Manufacturing Letters*, 2019, 19, p. 10-14.
4. Yuewei Ai, Zheng Kang, Yung C. Shin, Benxin Wu, Analysis of weld geometry and liquid flow in laser transmission welding between Polyethylene Terephthalate (PET) and Ti6Al4V based on numerical simulation, *Optics & Laser Technology*, 2018, 103, p. 99-108
5. Ze Liu, Benxin Wu, Zheng Kang, Zhen Yang, Microhole drilling by high intensity focused ultrasound-assisted water-confined laser micromachining, *Journal of Manufacturing Science and Engineering*, Accepted

Journal papers under preparation:

1. Zheng Kang, Jitendra Kumar Tripathi, Muxuan Wang, Ahmed Hassanein, Benxin Wu. Laser-based fabrication of carbon nanotube–metal composite on polymer: experimental study and characterizations. Under preparation.
2. Hanyu Song, Zheng Kang and Benxin Wu, “Time-resolved in-situ temperature measurement and analysis for continuous-wave laser sintering of carbon nanotube – metal composites on a polymer substrate”, Journal of Materials Processing Technology, under preparation.
3. Hanyu Song, Zheng Kang and Benxin Wu, “Nanosecond laser sintering of carbon nanotube – metal composites on a polymer substrate: the thermal accumulation effect revealed by time-resolved temperature measurement”, Journal of Manufacturing Science and Engineering, under preparation.